ELECTROCHEMICAL BEHAVIOR AND MORPHOLOGICAL EVOLUTION IN CARBONACEOUS AND METAL ANODES FOR Li-ION AND Zn-ION BATTERIES

By

DARRELL REID GREGORY

Bachelor of Science in Chemical Engineering

Oklahoma State University

Stillwater, Oklahoma

2019

Submitted to the Faculty of the
Graduate College of the
Oklahoma State University
in partial fulfillment of
the requirements for
the Degree of
MASTER OF SCIENCE
May 2021

ELECTROCHEMICAL BEHAVIOR AND

MORPHOLOGICAL EVOLUTION IN

CARBONACEOUS AND METAL ANODES FOR

Li-ION AND Zn-ION BATTERIES

Thesis Approved:

Ömer Özgür Çapraz

Thesis Adviser

Jindal Shah

Marimuthu Andiappan

Ritesh Sachan

ACKNOWLEDGEMENTS

During my time here at OSU, I have had the opportunity to work with many exceptional people who have helped me immensely, and who I would like to thank here briefly.

First of all, I would like to thank my fellow graduate student lab members, Bertan Özdogru and Hannah Dykes. Whenever I first joined the lab group, Bertan gave me training on all of the common lab equipment and taught me the basics of working in an electrochemistry lab for which I am very grateful. He was also always open to answer any questions I had about the lab, electrochemistry, or graduate school in general. Without his help, I would have been very lost at the start of my time here and would have struggled immensely. I would also like to thank the two undergraduate students, Cameron Ketelsleger and Tanner Hagerman, I had the pleasure to work with here. They both always had a great attitude and an excellent work ethic and were remarkable colleagues.

I would also like to thank all of the collaborators I have had a chance to interact with in my graduate studies. I would like to thank Dr. Stephen Cronin and his graduate student, Sisi Yang, from USC for providing the annealed soot and giving important feedback on the soot study. I would also like to thank Dr. Mileva Radonjic and her graduate student Cody Massion for taking the time to assist me with Raman spectroscopy measurements. I am also very appreciative of the XRD and SEM workers at Research Park, Brent Johnson and Lisa Whitworth, for showing me how to use SEM and helping me with XRD measurements.

Many thanks to my graduate advisor, Dr. Ömer Özgür Çapraz, for his support throughout my studies. Dr. Çapraz was indispensable for finding me projects to work on, his guidance on my research and career advice, and for helping prepare me for my time after graduation for which I am very thankful.

I am thankful to the graduate college for supporting me with graduate teaching assistant positions.

I am grateful to my committee members, Dr. Jindal Shah, Dr. Mari Andiappan, and Dr. Ritesh Sachan for their time and their valuable feedback on my projects.

I am deeply indebted to my family members, my mom Noreen Gregory, my dad Jon Gregory, and my sister Audra Gregory for always supporting me and believing in me.

I am extremely appreciative of everyone I have mentioned and feel very lucky to have met them. I would not be where I am today without their help.

Name: DARRELL GREGORY

Date of Degree: MAY 2021

Title of Study: ELECTROCHEMICAL BEHAVIOR AND MORPHOLOGICAL EVOLUTION IN CARBONACEOUS AND METAL ANODES FOR Li-ION AND Zn-ION BATTERIES

Major Field: Chemical Engineering

Abstract: Li-ion batteries are ubiquitous in modern society with widespread applications in electric vehicles, personal electronics, and renewable energy storage. However, the practical energy density of the graphite anode commonly used in commercially available Li-ion batteries is approaching its theoretical limits. One potential solution to overcome this limitation is to replace graphite anodes with metallic anodes which have much higher theoretical charge storage capacities (3860, 1165, 860 mAh/g for Li, Na, Zn metal anodes respectively vs. 372 mAh/g for graphite). Unfortunately, problems arise during charging of metal anodes when metal ions are plated onto the electrode. These ions tend to deposit unevenly over the surface producing rough morphologies called dendrites which can grow through the separator and contact the counter electrode causing a short circuit, thermal runaway, and potential ignition of the flammable electrolyte and explosion.

My master's project investigated how electrode surface layers impact dendrite growth on Zn metal electrodes. Zn metal provides the opportunity to elucidate the effect of organic surface layers on metal deposition since Zn is stable in both organic and aqueous electrolytes. Symmetric cells were assembled using Li, Na, or Zn metal in an analogous organic electrolyte (1 M $M(ClO_4)_x$ in EC:DMC where M is Li, Na, or Zn) and compared to a Zn cell with aqueous electrolyte (1 M $Zn(ClO_4)_2$). Further investigations were done to determine the surface layer effects by forming an organic surface layer on Zn metal electrodes and cycling them in aqueous electrolyte and comparing this to the performance of Zn metal anodes with an inorganic layer cycled in organic electrolytes.

My master's studies included another project about utilization of industrial waste as potential Li-ion battery electrodes. The effectiveness of collected diesel engine exhaust soot as a potential anode material for Li-ion batteries was evaluated through a series of electrochemical characterization tests including rate performance testing, long-term cycling stability, and charge storage kinetics analysis. Material properties were determined using XRD, XPS, and Raman spectroscopy. The annealed soot electrodes displayed excellent rate capability and capacity retention along with a pseudocapacitive contribution to charge storage making them an inexpensive alternative to the graphite anode.

TABLE OF CONTENTS

Chapter Page

LIST OF TABLES

Table Page

LIST OF FIGURES

Figure Page

CHAPTER I

INTRODUCTION

1.1 HISTORY OF BATTERIES

Rechargeable batteries have become a ubiquitous part of modern society. The world of today is extremely reliant on a myriad of electronic technology which are, in many cases, powered through battery technology. These devices include laptops, pacemakers, digital cameras, power tools, handheld game consoles, electric vehicles, and, of course, cellular phones. Due to their importance as electrochemical energy storage devices, a considerable amount of research effort is currently being directed towards improving the capabilities of these rechargeable batteries. Before looking at the current state of battery technology and considering how it may advance in the future, we will first summarize the history of batteries.

The invention of the electric battery is universally accredited to the Italian chemist Alessandro Volta who performed key experiments around the turn of the 19th century. In the year 1799, Volta developed the first-known battery, the "Voltaic Pile", which consisted of disks of different metal (for example, zinc and silver) separated by a piece of cloth soaked in salt water. These stacks generated a small electric potential of between 1-2 V and produced a small electric current for use in experiments. Additionally, a group, or "battery", of these piles could be connected in series to provide a more powerful energy source. This early foray into battery development was further improved by John Daniell who, in 1836, invented what became known as the "Daniell cell". Volta's original battery design produced a film of hydrogen bubbles on the cathode surface as a result of electrolysis of the electrolyte. This phenomenon increased the internal resistance of the battery as the film developed. The Daniell cell consisted of a copper cylinder filled with a copper (II) sulfate solution containing another vessel with a zinc electrode immersed in sulfuric acid. This design utilized a second electrolyte which allowed for the deposition of copper to occur in place of the hydrogen gas evolution. This invention turned out to be popular in the 19th century as a source of electricity in applications such as telegraphs. However, both technologies lacked one critical

feature. Once discharged, the cells had no way to be recharged and lost their function as a source of electrical power. For batteries to become essential in the way they are in the modern world, they would need to be rechargeable.

The first rechargeable battery was invented in 1859 by the French physicist Gaston Plantè. Plantè's invention involved two sheets of pure lead separated by a linen cloth rolled into a spiral and placed inside a sulfuric acid solution. This apparatus was the first example of a lead-acid battery which still finds widespread use today as automobile starters. In a major improvement over previous battery designs, the lead-acid battery would accept a reverse current allowing for it to be recharged and subsequently used again. There was now a distinction between batteries with only one discharge use (primary batteries) and those which could be used repeatedly (secondary batteries). A commercially viable version of this battery was created in 1881 by Camille Faure who used a lead lattice grid with lead oxide pasted within that proved easier to mass produce. Interestingly, one of the early applications of these lead-acids batteries was in electric vehicle applications in 1894, an area which continues to be massively popular[1]. The lead-acid battery proved to be quite attractive and has retained a large portion of the battery market over the intervening years accounting for between 40-45% of all battery sales in 1999[2].

The next major milestone in rechargeable battery technology occurred in 1899 with the creation of a nickel-cadmium battery by Waldemaar Jungner. As the name implies, this battery featured nickel and cadmium electrodes in a potassium hydroxide solution. The Ni-Cd battery presented an increased energy density over its main competitor, the lead-acid battery, (40-60 W h kg^{-1} compared to lead-acid's 35-40 W h kg^{-1}) while also featuring greater chemical and physical durability. Like the lead-acid battery, these improvements secured the nickel-cadmium battery a place in the battery market for many years with an estimated market of $3 billion in 1995[3]. Jungner also produced several other alternative battery combinations including nickel-iron and silver-cadmium which proved to be less attractive than his Ni-Cd design due to lower energy densities. Unfortunately, cadmium is a toxic heavy metal and represents a potential environmental threat[4]. This reality necessitated the development of more advanced battery configurations.

This development began to take form when the nickel-hydrogen battery started development in 1970 at COMSAT laboratories[5]. The nickel-hydrogen battery acted in a similar manner to fuel cells by replacing the cadmium electrode in the nickel-cadmium battery with hydrogen gas. This technology had the dual of advantage of providing an increase in the energy density (55-75 W h kg^{-1}) over nickel-cadmium batteries while also not utilizing toxic cadmium

metal. Due to its higher energy density and long cycle lifetime, nickel-hydrogen batteries found a role as energy storage for satellites and space probes in the 1970s[6]. However, while these batteries may not have contained cadmium, the need for hydrogen gas presented a potential safety issue which kept them from ever becoming commercially viable.

While nickel-hydrogen battery development was beginning in 1970, another group of scientists at Philip Research Laboratories discovered that certain metallic alloys were capable of adsorbing large amounts of hydrogen at room temperature[7]. Throughout the 1970s and into the 1980s, more of these "metal hydrides" were discovered and potential applications were evaluated. This effort eventually culminated in 1987 when Willems and Bucshow built upon technology from the nickel-hydrogen battery and employed $La_{0.8}Nd_{0.2}Ni_{2.5}Co_{2.4}Si_{0.1}$, a metal hydride, as an electrode material in a nickel-hydride battery[8]. Their newly created nickel-hydride configuration exhibited remarkable cycling capability with a retention of 84% of its initial capacity over 4000-charge-discharge cycles at a charge/discharge rate of 1C (charge/discharge in 1 hour). Their discovery directly led to the commercialization of nickel-metal hydride (NiMH) batteries in 1989. Over the following years, NiMH batteries (specific energy density of 60-120 W h kg^{-1}) have been adopted by many consumer electronics and were the primary means of energy storage in electric vehicles before Li-ion batteries[9].

For many years, lead-acid and nickel-cadmium battery designs dominated the battery landscape, until the development of the lithium-ion battery in the 1980s. Lithium metal had long been considered a promising candidate as an electrode material due to its low molecular weight granting it an extremely high energy density (a pure Li metal anode has a theoretical specific capacity of 3862 mA h g^{-1})[10]. Early work describing pure Li metal as a potential anode material date back to the 1960s[11]. Increased interest into this research area over the ensuing decade was likely driven by the oil crisis of the 1970s which highlighted the need for fossil-fuel free energy sources[12]. In the mid-1970s, a British-American scientist by the name of Stanley Whittingham discovered the concept of intercalation electrodes for Li^+ ion storage[13]. His initial finding involved the material titanium disulphide (TiS_2), a layered material with gaps in its crystal structure that could house lithium ions during charging and discharging while retaining its overall crystal structure. He used TiS_2 as an innovative cathode material in a battery paired with metallic lithium. The resulting configuration had high-power capability due to an electrical potential difference of 2 V between the two electrodes. However, the metallic lithium used as the battery's anode was very reactive (for example, like all alkali metals, lithium reacts with moisture and oxygen in the air) and rendered the battery too unstable for commercial applications. Even with this caveat,

Whittingham's discovery would pave the way for more innovations that would eventually lead to the creation of the Li ion battery.

In 1980, John B Goodenough, a professor at the University of Texas at Austin, improved upon Whittingham's work when he proved that cobalt oxide was also able to intercalate lithium ions and was a viable cathode material[14]. Cobalt oxide functioned by a similar mechanism to TiS_2 with its ability to reversibly house lithium ions in voids in its crystal lattice. Dr. Goodenough had predicted that metal oxides would provide an even greater potential difference than metal sulphides due to the presence of oxygen species within the material. His prediction was validated with cobalt oxide which has a potential of 4 V vs metallic lithium. With this larger potential gap, lithium-ion battery technology had a promising cathode material capable of high-power outputs but was still lacking in a suitable anode material. This all changed in 1985 when Akiro Yoshino created the first commercially viable Li-ion battery using Goodenough's cobalt oxide cathode and an anode comprised of petroleum coke, a carbonaceous, layered material with the ability to intercalate Li - ions[15]. His anode exhibited a low potential versus lithium meaning that batteries with it as their anode in place of metallic lithium would still present high voltages and correspondingly high power outputs. Additionally, Yoshino's anode was much safer than pure lithium due to its greatly reduced reactivity and was highly rechargeabl. This petroleum coke was the precursor to the common graphite anode found within most modern Li ion batteries. In recognition of their achievements, the 2019 Nobel Prize in Chemistry was jointly awarded to Stanley Whittingham, John B. Goodenough, and Akira Yoshino for their work in developing the secondary Li-ion battery.

This newly developed Li ion battery was a major step forward over all previous battery designs, including the concurrently developed nickel-metal hydride battery. It has the advantage of having the highest volumetric and gravimetric energy densities of all commercially available batteries (100-250 W h kg^{-1} and 250-680 W h L^{-1}, respectively), a low self-discharge rate, and a lengthy cycle lifetime. With these attributes, Li-ion batteries have seen wide use in the modern world since their commercialization by Sony in 1991 with applications in electric vehicles and portable electronics. Of course, over the previous 3 decades, there has been considerable progress in identifying and developing additional electrodes for Li ion battery applications. Modern cathode materials include lithium manganese oxide (LMO), lithium iron phosphate (LFP), lithium nickel manganese cobalt oxide (NMC), and lithium nickel cobalt aluminum oxide (NCA)[16]. While on the anode side, there has been progress in identifying lithium titanate (LTO), hard carbon, and silicon as suitable electrode materials. A summary of the previously highlighted rechargeable batteries depicting their energy densities is provided below in Figure 1.1.

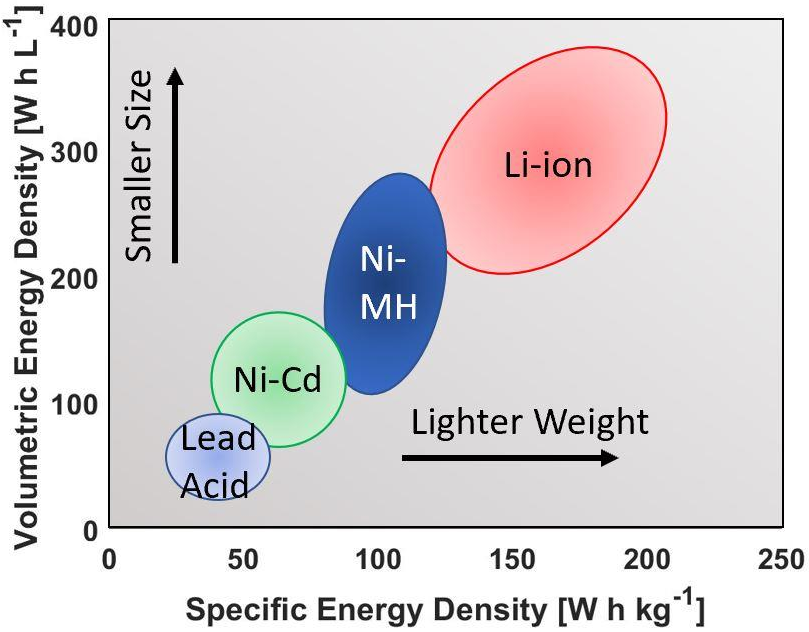

Figure 1.1: A comparison of energy densities for common commercially available batteries

However, there is still much room for improvement in the battery industry even over cutting-edge Li-ion battery designs. While lithium-ion batteries have the highest energy densities of all current commercially viable batteries, their energy densities are still far below what they could be if pure metals were used as an anode material. This innovation would allow for much lighter battery systems which may be required to bring technologies such as electric vehicles to widespread acceptance. Unfortunately, the use of a bulk metal as an electrode material is beset with a variety of issues which will be discussed in greater detail further on. Additionally, lithium is only the 25th most abundant element in the Earth's crust and is primarily mined in potentially politically unstable regions of South America which could indicate a scarcity of lithium metal in the future and will hamper lithium metal's attractiveness for grid storage applications where larger quantities are required[17,18]. For these reasons, it is imperative to look for innovations that go beyond lithium-ion batteries which can successfully meet the energy needs of the future.

1.2 BEYOND Li-ION BATTERIES

In this section, I will briefly describe the components, processes, and issues present in typical metal and metal-ion batteries. Three primary categories of rechargeable batteries will be considered: metal-ion, metal-sulfur, and metal-air batteries. To assist with these descriptions, simplified representations of these batteries are provided below in Figure 1.2. These groups of batteries all

share 4 primary components: an anode, a cathode, an electrolyte-permeable separator, and an electrolyte solution. The fundamental distinction between metal and metal-ion batteries concerns the nature of the anode material. Metal batteries (for example, metal-air and metal-sulfur batteries) utilize a bulk mass of a pure metal as their anode, while metal-ion battery anodes are comprised of host structures which can intercalate or adsorb metal ions. This key difference endows metal batteries with much higher energy densities and theoretical capacities than metal-ion batteries because no weight or space is added by an inert compound for accepting ions. To illustrate this point, a pure lithium metal anode has a theoretical capacity of 3862 $mA{\cdot}h{\cdot}g^{-1}$; however, the most common lithium-ion battery anode's (graphite) theoretical capacity is an order of magnitude lower (372 $mA{\cdot}h{\cdot}g^{-1}$)[10,16]. In the following section, I will describe the battery components and their electrochemical processes.

The electrolyte is composed of a salt containing the charge carrier ion dissolved in a solvent. The electrolyte allows for the charge carrier ion to travel from the anode to cathode during discharging or cathode to anode during charging. For metal ion batteries, the electrolyte solution can be either aqueous or organic; however, organic electrolytes are favored since the voltage window of aqueous electrolytes are limited by the oxygen evolution reaction on the cathode surface. For alkali metal batteries, an organic electrolyte must be used due to the reactivity of alkali metals with water. The highly negative electrochemical potentials of typical battery anodes are greater than the lowest unoccupied molecular orbital (LUMO) of organic electrolytes which leads to reaction between the electrode and electrolyte and results in the formation of a layer of organic and inorganic decomposition products on the anode surface[19,20]. This layer is called the solid-electrolyte interface (SEI) layer and will be discussed in more detail later in the section concerning capacity fade in battery materials. The chosen electrolyte will play an important role in the cycling performance of the battery not only because its own ionic conductivity, cation transference number, and viscosity will play a role in mass transport processes in the cell, but also because it will determine crucial properties of the SEI layer such as ionic conductivity, elasticity, and chemical stability[21]. Within the electrolyte, the separator plays the important role of keeping the anode and cathode from coming into physical or electrical contact with each other while still allowing the passage of ions between the electrodes. If the two electrodes did contact each other, a short circuit would result that would prevent the battery from functioning as an energy storage device, and could lead to thermal runaway, ignition of the flammable electrolyte, and possible explosion.

As mentioned earlier, metal-ion batteries are differentiated from other battery types by their anode material. Their electrode materials need to be capable of reversibly accepting, storing, and

releasing metal ions over many charge and discharge cycles. Conventional anode materials include carbonaceous materials like graphite and hard carbon as well as metal alloy based anodes such as Si, Ge and Sn[22]. Cathode materials are much more diverse and include groups of materials such as layered transition metal oxides, tunnel structured spinel oxides[23], polyanionic compounds[24], and Prussian blue analogues[25]. As an example, a typical lithium-ion battery configuration could include a graphite anode (where Li ions are stored between the graphene sheets), a layered metal oxide cathode (e.g. $LiCoO_2$, $LiMn_2O_4$, etc.), and a lithium salt in a carbonate based solvent as electrolyte (e.g. $LiPF_6$ in propylene carbonate).

The metal-ion battery functions by transferring electrons through an external circuit (where electrical power may be either extracted or supplied) connecting the two electrodes while metal ions simultaneously migrate from one electrode through the electrolyte to the opposite electrode. Electrochemical reactions occur on the surfaces of the two electrodes where one surface is oxidized (generates electrons) and the other is reduced (accepts electrons). During discharge, electrical energy may be extracted from the battery and used to power electronic devices as the electrons (and ions) flow from the anode to the cathode. During charge, the reverse is true. Energy must be supplied to generate the electrons and ions via electrochemical reactions. The operating potential of the cell and the magnitude of the implemented current are directly related to the electrical power generated (or supplied) through the simple expression

$$P = I * V \tag{1.1}$$

where P is the power, I is the current, and V is the cell voltage. The energy density of the battery can likewise be calculated with the expression

$$energy\ density = Q * V \tag{1.2}$$

where Q is the charge storage capacity of the battery and V is the cell potential. Furthermore, a battery's specific charge capacity can be calculated using Faraday's Law as follows

$$\frac{Q}{m} = n * \frac{F}{M} \tag{1.3}$$

where n is the number of electrons involved in the reaction, F is Faraday's constant (96485 C mol^{-1}), and M is the molecular weight of the electrode. As an illustration, consider the Li-ion battery anode material graphite. During the charge cycle, graphite lithiates to LiC_6 at full charge. For every mole of carbon in the anode, there is an equivalent of 1/6 mole of electrons traveling through the external circuit. Therefore, n = 1/6 and M is the atomic weight of carbon, 12.01 g/mol. After

appropriate unit conversion, Faraday's law indicates that graphite has a theoretical capacity of 372.2 mA h g^{-1}. High energy densities are enticing because they enable lightweight, compact battery designs. Smaller and lighter batteries would be advantageous in both portable electronic and in electric vehicle applications.

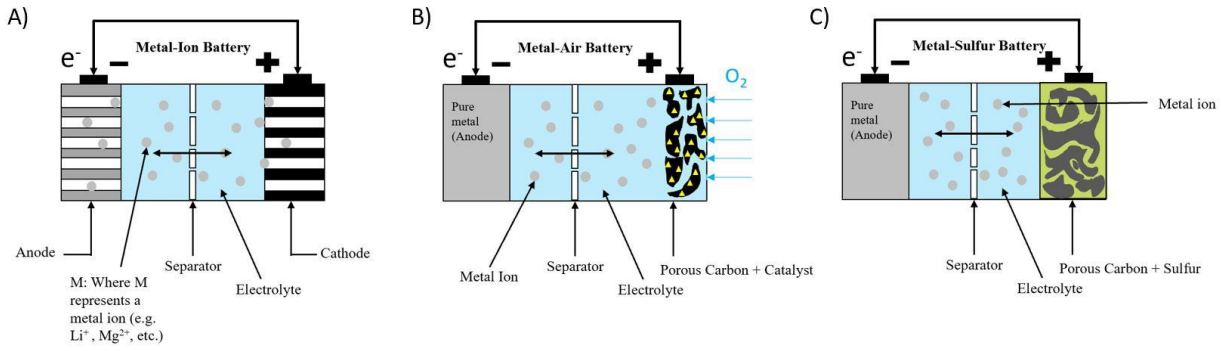

Figure 1.2: Depictions of representative A) metal-ion, B) metal-air, and C) metal-sulfur batteries

The other two types of batteries I will describe here, metal-air and metal-sulfur, fall under the broader classification of metal batteries. Representations of their typical configurations are provided in Figure 1.2. This category of battery is distinguished from metal ion batteries because they use a bulk supply of the mobile metal ion as their anode material. In contrast to intercalation anodes, where the electrode capacity is diminished by the inert host structure which takes up space and adds weight to the battery, metal batteries directly plate/strip metals onto a current collector. Due to the absence of a host structure, the potential energy and power densities of metal batteries far exceed those of metal-ion batteries. Lithium is widely regarded as the preeminent negative electrode material due to its theoretical capacity of 3862 mA·h ·g^{-1} and its very low reduction potential (-3.05 V vs SHE)[26]. However, other metals such as Na and Zn are also being widely researched. Sodium metal, while possessing a much lower theoretical storage capacity (1165 mA h g^{-1}) and higher redox potential (-2.71 V vs SHE) than Li, is considerably more abundant than Li and consequently far less expensive. Zinc metal offers the advantage of reduced reactivity compared to alkali metals. This quality makes it inherently safer and also enables the use of aqueous electrolytes which possess higher ionic conductivities than organic electrolytes.

The first metal battery I will describe is the metal-sulfur battery. An illustration of a metal-sulfur battery is provided above in Figure 1.2C. Metal-sulfur batteries feature a bulk mass of the pure metal as their anode and a sulfur containing species as the cathode. In current research, the cathodes of metal-sulfur batteries typically consist of sulfur compounded with either carbon, a

conductive polymer, or a metal/metal oxide[27]. Sulfur needs to be compounded with another material due its insulating nature and large volumetric changes when used on its own[28]. With a theoretical capacity of 1675 mA h g^{-1}, sulfur has the highest capacity of all solid cathodes when paired with lithium and is a relatively abundant (10th most abundant in the Earth's crust) and inexpensive (~$150 per ton in 2018) element[29]. Unfortunately, metal-sulfur batteries are plagued by issues relating to the formation of metal polysulfides on the cathode surface during discharge. These metal polysulfides do not remain on the cathode, but instead "shuttle" to the anode where they contaminate the metal anode[30]. This causes unsatisfactory lifetimes and low efficiency as the cathode active material is continuously consumed.

A representative metal-air battery is provided above in Figure 1.2B. Metal-air batteries feature the same anode as metal-sulfur batterie (a pure metal plating onto a current collector), but use a porous scaffold supporting a catalyst for the oxygen evolution reaction (OER) and oxygen reduction reaction (ORR) on the cathode side. The actual active material on the cathode side is oxygen which flows into the battery. Oxygen is reduced on the cathode side via electrocatalytic reactions to form metal oxides during discharge and undergoes oxygen evolution reaction during charge. Since the cathode active material is a gas that flows in and out of the device and not a solid which remains in and adds weight to the battery, metal-air batteries possess very high theoretical energy densities (3505 W h kg^{-1} for a lithium-air configuration) and have great potential to replace gasoline for electric vehicles[31]. Unfortunately, the cathodes in metal-air batteries tend to become passivated by the metal oxide discharge products which accumulate on the surface and block the incoming oxygen from interfacing with the electrolyte[32]. This process severely limits the reversibility of metal-air batteries and causes quick capacity fade and low cycle lifetimes. Further issues can arise when porous carbon scaffolds are used. During the charge process, the carbon scaffold and electrolyte can decompose to form metal carbonates which further passivate the electrode, increase cell polarization, and cause additional capacity fading[33].

In addition to the problems specific to metal-air and metal sulfur batteries, all metal batteries share issues concerning uneven metal deposition onto the anode surface to produce dendritic morphologies. This feature will be discussed in greater detail in the following section.

1.3 CURRENT CAPACITY RETENTION AND SAFETY ISSUES WITH METAL AND METAL-ION BATTERIES

As indicated in the preceding section, the processes occurring in metal and metal-ion batteries are distinct. Consequently, a different set of problems are present in metal and metal-ion batteries. I will begin this section by discussing the dendritic issues facing metal battery technology and end with a description of the common causes of capacity fade in metal and metal-ion batteries.

In addition to the specific problems highlighted above for metal-air and metal-sulfur batteries, all metal batteries share one destructive similarity, dendritic deposition on the anode surface. During charging, metal ions will deposit non-uniformly on the anode surface. The areas which experience the greatest amount of deposition will form preferential nucleation sites for further deposition due to the lower kinetic barrier to grow new deposits over initiate new ones. This process will cause the deposited metal to form irregular structures called dendrites on the anode which will grow towards the cathode. This phenomenon has been observed to occur in a wide variety of metals during electrodeposition including Li[34], Na[35],K[36], Zn[37], Mg[38], and many others[39]. These dendrites present a variety of potential safety concerns and capacity fade issues. As they grow, dendrites will inevitably expand through the anode's SEI layer and contact with the electrolyte solution. This contact will result in further electrolyte and metal consumption as the electrolyte will decompose to form an SEI layer over the newly exposed metal surface. With continued growth, the dendrites will pierce the separator and eventually encounter the cathode causing a short-circuit. Short-circuits introduce the potential for thermal runaway which can ignite highly flammable organic electrolytes and potentially result in an explosion.

Another problem arises during the discharge process. Metal on the anode undergoes electrodissolution as it oxidizes to form cations that migrate to the cathode. If this metal stripping occurs at the base of a dendrite, it can result in the dendrite breaking off from the anode and floating into the electrolyte. This "dead" particle is no longer in contact with the anode and will no longer be able to participate in charge storage. The combination of continuously reacting electrolyte and formation of "dead" metal leads to low Coulombic efficiencies in metal anode batteries and limits their reversibility and cycle life[40]. The mechanism for dendrite formation and growth is still an area of intensive research with several models having been proposed to describe the phenomenon. These models include the phase-field model[41], the SEI model[42], the charge-based model[43], the deposition/dissolution model[44], and the film growth model[45].

The capacity of battery electrodes degrades with cycle number due to mechanical and chemical deformations in the electrode. Metal and metal-ion batteries share three capacity fade mechanisms which will be discussed. These are capacity losses due to SEI formation, volumetric expansion, and dissolution of cathode materials. I will begin by looking at the SEI layer and its relation to capacity fade.

The existence of an SEI layer was first proposed by Peled in 1979 based on observations of unusual electrolysis behavior of certain electrolytes[20]. It describes a mechanism in non-aqueous batteries where a solid layer forms on the electrode surfaces due to decomposition reactions between the electrodes and the electrolyte. The operating voltage window of the electrolyte is determined by its highest occupied molecular orbital (HOMO) and lowest unoccupied molecular orbital (LUMO). If the electrochemical potential of the anode is above the LUMO, then the electrolyte will be reduced on its surface. Likewise, if the electrochemical potential of the cathode is below the HOMO, then the electrolyte will oxidize on its surface to form a cathode electrolyte interface (CEI)[46]. The redox potentials of the anode materials found in metal-ion batteries and the metals in metal batteries lie outside of this potential range. This causes decomposition reactions to occur on the anode surface which leads to formation of an SEI layer over the entire anode surface. A beneficial SEI layer is electronically insulating which prevents further reaction between the electrode and electrolyte while also being conductive to metal-ion transfer to allow continual charging and discharging. SEI formation occurs primarily during the initial cycles but continues to gradually grow over additional cycles. This process uses up a portion both the electrolyte and metal-ion species which leads to a noticeable loss of capacity during the first cycle (~10% for graphite anode in lithium ion batteries) and additional lesser capacity losses in subsequent cycles[47]. This process is exacerbated in metal batteries which tend to form less stable SEI layers than graphite anodes and the dendrites in metal batteries will grow through the SEI and contact the electrolyte where they will react further with the electrolyte to form more SEI.

Electrodes also undergo continuous strain generation upon ion intercalation and associated stress formation upon ion intercalation. During ion insertion and extraction, electrodes will undergo volumetric expansions and contractions. As more metal ions are stored within the electrode material, the electrode will experience a positive strain and associated stress as it expands to accommodate the new material. As the ions are extracted, the reverse is true; the electrode will undergo a negative strain as it shrinks back to a smaller size. The magnitude of strain depends heavily on the electrode material, ranging from ~400% for silicon anodes in lithium-ion batteries to effectively 0% for “no-strain” electrodes (e.g. LTO)[48,49]. These mechanical changes have the

potential to introduce additional capacity loss in the material owing to either cracks in the SEI or electrode particle fracturing. If the SEI layer is not elastic enough to accommodate the cyclic expansions and contractions of the electrode, it will begin to crack or fracture[50]. When this happens, additional electrode surface will be exposed to the electrolyte where new SEI will form and capacity will be lost. If the stresses caused by the ion diffusion within the particle are great enough, they can cause actual fracturing of the electrode particle. Similar to the phenomenon with dendrites, this results in a portion of the electrode losing contact with the bulk electrode. At this point, the fractured particle will consume electrolyte and charge carrier ions as SEI forms on its new surface, and it will no longer contribute to charge storage. In the case of metal batteries, the cracks in the SEI serve as hot spots for metal deposition since there is less resistance to charge transfer at locations with a thinner SEI layer. This makes these regions particularly susceptible to dendritic growth. An SEM image of a fractured lithium manganese oxide particle is provided below in Figure 1.3 as an example.

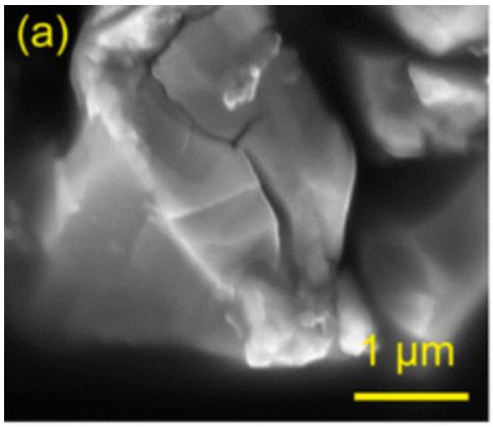

Figure 1.3: SEM image of fractured LMO particle after first charge cycled in 1 M $LiPF_6$ in (1:1:1) EC:DMC:DEC electrolyte at C/2[51]

Dissolution of active material from the cathode is another common means of capacity fade in batteries. During long term cycling, components of the cathode can dissociate from the cathode surface due to their solubility in the electrolyte and lose contact with the bulk electrode. The loss of cathode material reduces the charge storage capacity of the cathode and leads to capacity fade. This process is especially prevalent in lithium manganese oxide cathodes where manganese tends to reduce to Mn^{2+} and dissociate[52]. The polysulfide "shuttle" effect mentioned in the previous section is another example of cathode dissolution.

1.4 COMMON ANALYTICAL TECHNIQUES AND METHODS

A variety of analytical techniques and methods have been employed in order the better understand the characteristics of the SEI layer, dendrites, and electrochemical performance. This section will provide a brief overview of some of the most prevalent methods for monitoring and characterizing battery materials. Specifically, this section will examine scanning and transmission electron microscopy (SEM and TEM respectively), X-ray diffraction (XRD), electrochemical impedance spectroscopy (EIS), cyclic voltammetry (CV), galvanostatic cycling, galvanostatic intermittent titration technique (GITT), and potentiostatic intermittent titration technique (PITT) as they relate to electrochemical research.

Scanning electron microscopy is used to reveal the morphology of the material of interest. In battery application, it is often used to characterize particle morphology and any physical changes occurring during cycling. Common features of interest include dendrite formation and growth, electrode particle size and morphology, volume expansion, particle cracking/particle fracturing, and SEI buildup. SEM functions by scanning a beam of electrons over the sample surface. Interactions between the electron beam and atoms in the sample produce signals which can be used to construct images. A few characteristic examples from literature of SEM images on dendrite formation are shown in Figure 1.4.

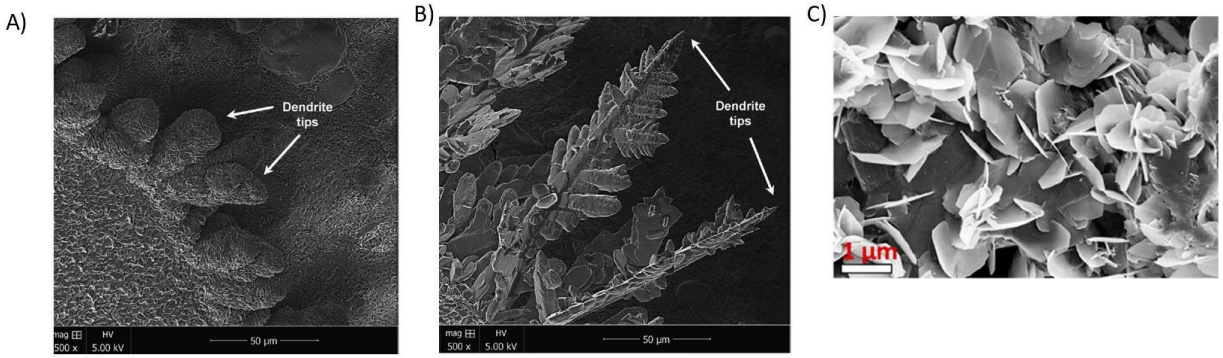

Figure 1.4: SEM images of different Zn dendrite morphologies from A) Zn electrode cycled in 0.1 M ZnO + 4M KOH electrolyte[53], B) Zn electrode cycled in 0.1 M Zn + 4 M KOH electrolyte solution also containing 10 ppm polethylenamine[53]s, C) Zn electrode cycled in 3 M $ZnSO_4$[54]

Transmission electron microscopy fills a similar role as SEM; it allows for visual images of nanoscale features occurring on the electrodes. Like SEM, TEM functions by sending a focused beam of electrons at the sample, but unlike SEM, TEM images are produced from interactions between atoms in the sample and the electron beam as the electron beam is transmitted through the

sample. With this mechanism, TEM can resolve images to an even higher level than SEM reaching even to the point of capturing single columns of atoms. However, this increased resolution comes at the cost of more precise sample preparation as the samples need to be thin enough for the electron beam to penetrate through. For battery applications, TEM is used in much the same way as SEM where it can be used to observe small changes occurring on or in the electrodes. For example, TEM has been used to measure volume expansion in electrode particles[55], lithium dendrite formation[56], and the presence of SEI layers[57]. Representative TEM images from literature showing a Si particle expanding and fracturing and Li dendrite growth on a Pt wire are shown below in Figure 1.5.

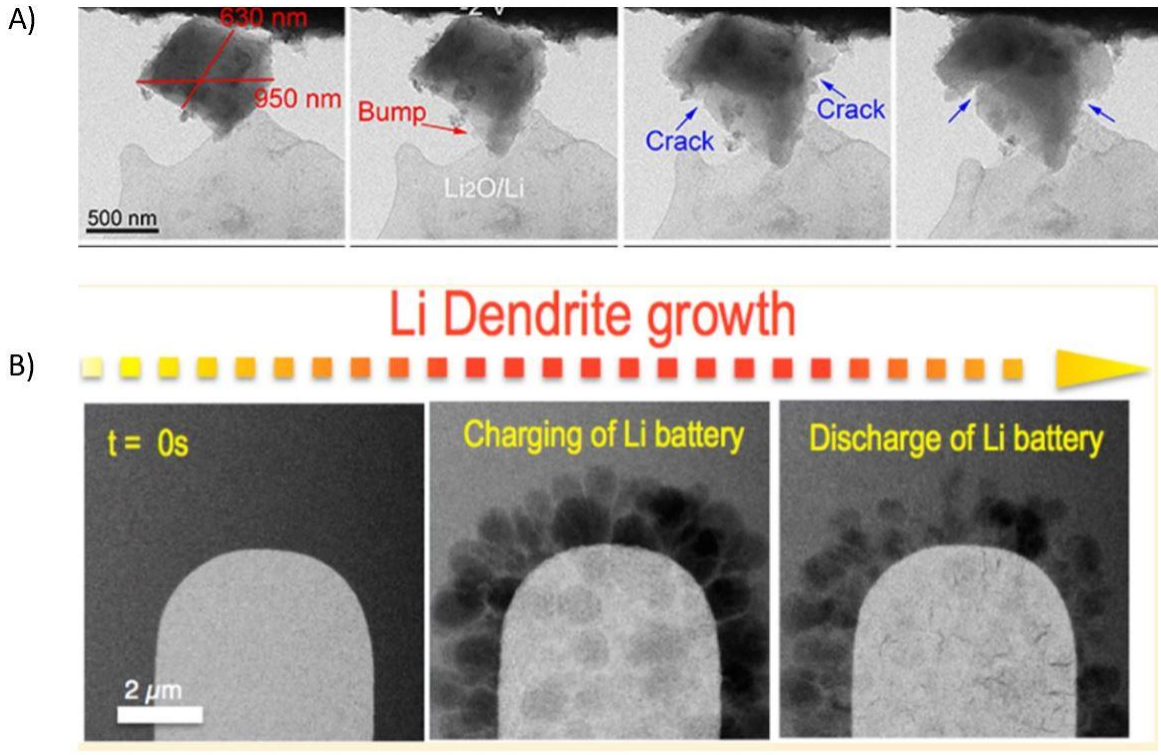

Figure 1.5: A) TEM images showing volumetric expansion and particle cracking of Si particles upon lithiation[55]. B) TEM image showing Li dendrites forming on Pt electrode during lithiation (charging) and presence of "dead lithium" during delithiation (discharging)[56]

X-ray diffraction is a powerful tool for obtaining structural information and crystallographic parameters for samples. In the battery, XRD is commonly used for studying phase transformations in intercalation electrodes and for measuring changes in lattice parameters during (de)lithiation). To give a few examples, XRD has been used to measure phase changes in Si electrodes during lithiation and delithiation wherein an amorphous LiSi phase forms alongside the crystalline $Li_{15}Si_4$

phase causing uneven volume variations and leading to mechanical degradation[58]. XRD has also been used to determine the anode and cathode temperatures in commercial Li-ion cells by measuring the changes in lattice parameters of the Cu and Al current collectors, respectively[59]. Temperature measurements like these are important for safety considerations due to the possibility of the thermal runaway during overcharging. As a final example, XRD was used to study the reaction mechanisms of lithiation in a variety of tin oxide materials[60]. This study showed than Li would initially irreversibly react with the oxygen species to form Li_2O leading an irreversible capacity loss in the initial cycles and subsequent electrode failure.

Electrochemical impedance spectroscopy is a technique which gives information about the various impedances in an electrochemical cell. There are a wide variety of processes occurring in the cell which influence the overall resistance such as molecular diffusion, SEI layer thickness and composition, double-layer charging, etc. Fortunately, the time scales for these processes vary significantly which allows EIS to differentiate between the resistance of these processes. By providing sinus currents (or voltages) at a range of frequencies and measuring the voltage (or current) response, EIS takes advantage of these various time constants and can be used to form a Nyquist plot which plots the imaginary portion of the impedance vs. the real impedance as shown in Figure 1.6. The data obtained from EIS can be fit to an equivalent circuit and provide quantitative insight into processes within the cell. a few examples of utilization of EIS from literature include monitoring the surface resistance of an electrode as the SEI layer thickens[61], calculating Li^+ chemical diffusion coefficients in lithium iron phosphate electrodes[62], and measuring the change in interfacial resistance on lithium anode as a result of an ex-situ formed LiF layer[63].

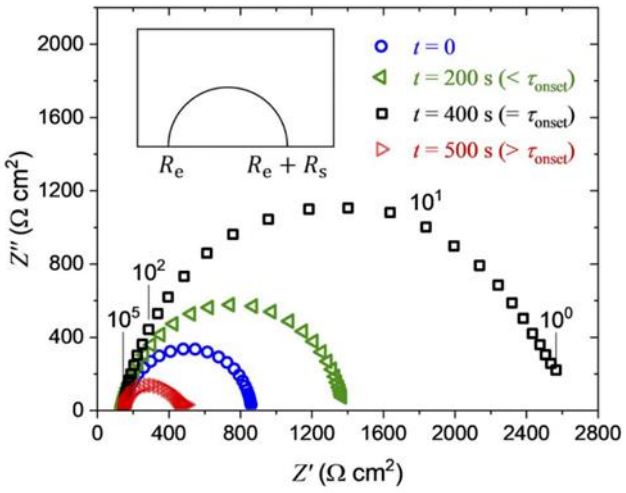

Figure 1.6: Representative Nyquist plot obtained from galvanostatic electrochemical impedance spectroscopy (GEIS) on a Li||Li symmetric cell with Li reference electrode[61]

Cyclic voltammetry is a common cycling technique for characterizing an electrode and/or an electrolyte. In this technique, the potential of the cell is linearly ramped at a constant rate to a cutoff voltage and then reversed to the other cutoff voltage. Over this test, the associated current response is measured and recorded to make quantitative observations of the system. The voltage range selected depends on the equilibrium potential of the reaction or phase transformation of interest and extends below and above this potential. A large jump or peak in current response is observed at the voltage where this reaction occurs, and the shape of the current peak can be used to deduce information about the kinetics of the system. For example, a more broadened peak is an indication of slow kinetics or decreased exchange current density while a sharper peak is indicative of faster kinetics and a more reversible electrochemical reaction[64]. In practice, CV is often used to test novel electrodes (e.g. hollow silica spheres embedded in porous carbon[65]) or to make comparisons between a bare electrode and a modified electrode, such comparing pre-sodiated hard carbon to bare hard carbon in sodium-ion batteries[66]. An illustration of the voltage ramping and induced current response is provided in Figure 1.7 for reference.

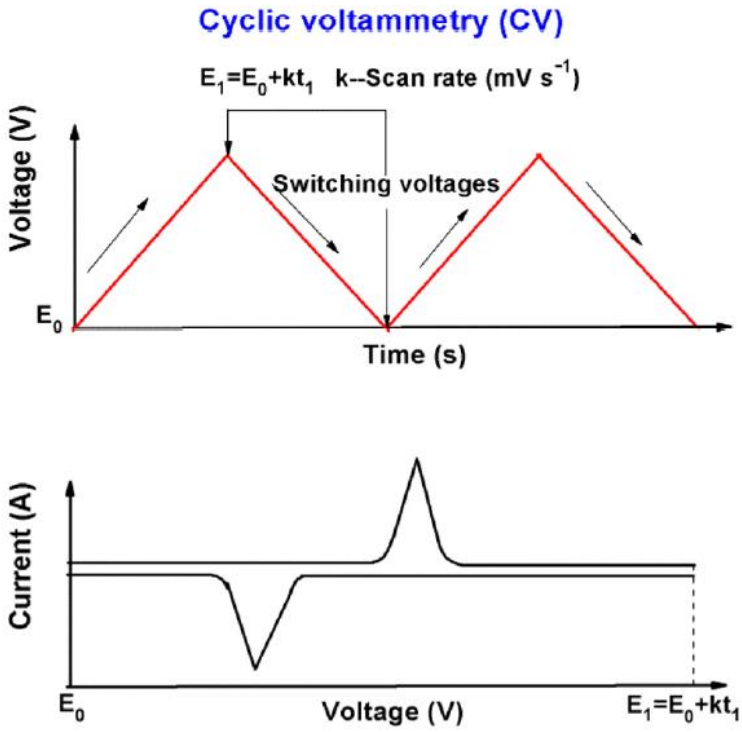

Figure 1.7: Depiction of the linear voltage ramp and a representative current response for CV[67]

Galvanostatic cycling is an extremely common technique for controlling the reaction rate and monitoring the electrochemical potential. This method involves applying a constant current to charge (or discharge) the cell to a cut-off voltage and then reversing the direction of the current to discharge (or charge) the cell to the other cutoff voltage and measuring the voltage response. The applied current is typically indicated as the C-rate which is the time required to perform one charge or discharge step. For example, a current that charges the battery in 4 hours would be designated as C/4 and a current which charges the battery in 30 minutes would be 2 C. Since the applied current is constant over time, charge capacity can be easily calculated as

$$Q = i * t \tag{1.4}$$

where Q is charge capacity, i is the applied current, and t is the duration the current is applied. Many charge-discharge cycles may be run on a cell, and the capacities of each cycle can be recorded and compared to provide information on capacity retention. Rate capability of electrodes can also be determined by applying different C-rates to the electrode allowing for measurements of variations in capacity due to rate of charge. Additionally, galvanostatic cycling can be used to measure Coulombic efficiencies, the ratio of charge extracted to charge inserted for a given cycle, to detect irreversible capacity losses. Galvanostatic cycling is also used in electroplating/stripping

studies for examining the deposition/dissolution behavior of a metal onto either a metal anode or a current collector[36].

The galvanostatic intermittent titration technique is specific form of galvanostatic experiment. In this method, a constant current pulse is applied for a short duration of time (e.g. 1 hour) and is followed by a long rest period (e.g. 10 hour) where the current is removed and the cell is allowed to relax back to an equilibrium state[68]. This process is then repeated until the cutoff voltage is reached. The potential difference between the working electrode and reference electrode is recorded over these periods and used to characterize properties of the electrode material. This technique is primarily used to measure the thermodynamic equilibrium potentials at various states of charge (SOCs) for a specific electrode material. This equilibrium potential is taken to be the open circuit voltage (OCV) at the end of each rest period. Additionally, this technique may also be used to calculate chemical diffusion coefficients at various SOCs. The model and theory behind this analysis will be discussed in further detail in a later section. As an example of these applications, GITT has been used to obtain equilibrium potentials and chemical diffusion coefficients for Li^+ and Na^+ in the common electrode materials $LiFePO_4$ and $NaFePO_4$, respectively[24]. Furthermore, GITT can be used to measure other kinetic and thermodynamic properties including partial conductivity, thermodynamic enhancement factor, and free energy of formation[68]. Figure 1.8 below displays a typical current and voltage response in an electrochemical cell undergoing GITT measurements.

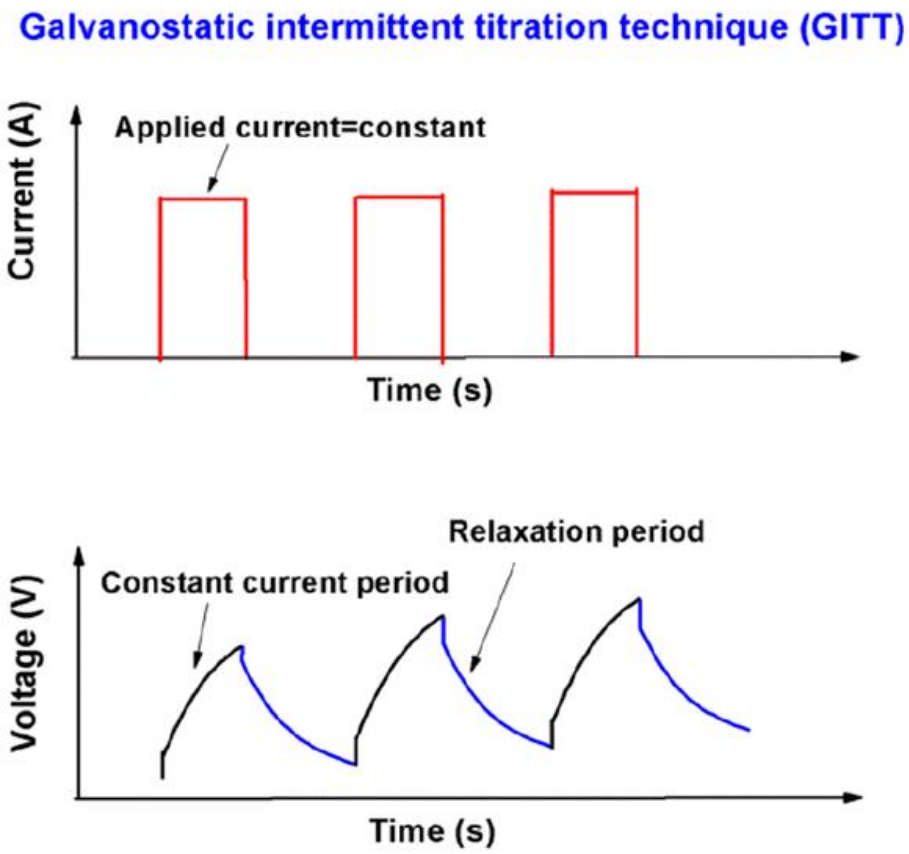

Figure 1.8: Representation of characteristic applied current and voltage response for GITT[67]

Potentiostatic intermittent titration technique (PITT) is also commonly used in electrochemical research to determine the transport and thermodynamic properties of electrode materials. In contrast to the previously described GITT, this technique involves a series of applied voltage steps where the potential of the working electrode with respect to a reference electrode is adjusted and held to a new value and current behavior is recorded over time[69]. Once the current required to sustain this potential has reduced to below a small, selected value, another voltage jump is applied, and this process is repeated until the cutoff voltage is reached. Similar to GITT, PITT can be used to determine chemical diffusion coefficients of a solute into a host structure. Also, PITT can be used to create quasi-equilibrium voltage-capacity plots. Figure 1.9 below shows provides a representation of the voltage steps and current response in a typically conducted PITT experiment. As an example of its application, PITT has been used to measure chemical diffusion coefficients and prepare voltage capacity plots for Li^+ in amorphous Si and graphitic carbon electrodes[70,71].

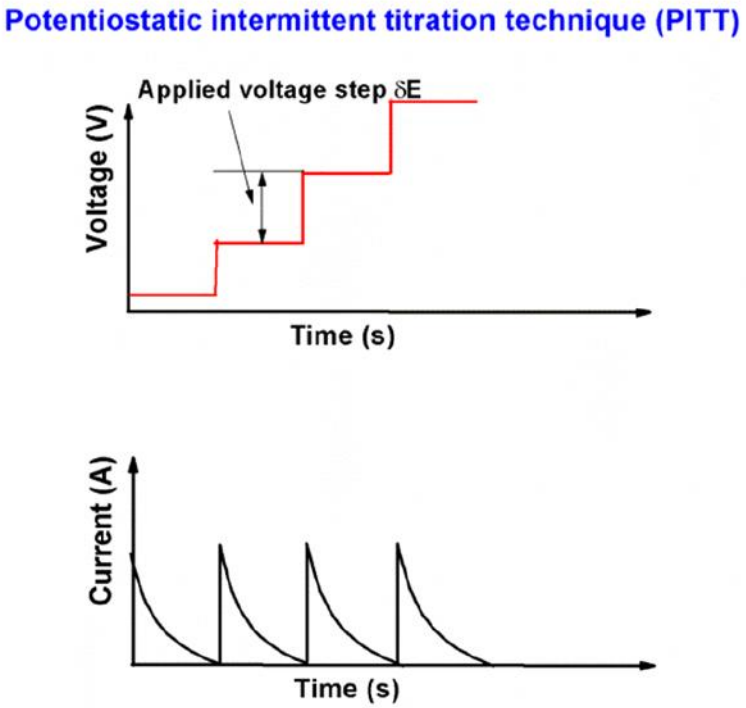

Figure 1.9: Representation of characteristic voltage steps and current response for PITT[67]

CHAPTER II

HYPOTHESIS

My master's studies were divided between two main projects, investigating the role of the solid-electrolyte interface (SEI) layer on deposition/dissolution behavior on Zn metal anodes and evaluating the electrochemical performance of diesel engine exhaust soot particles for use an anode material in Li-ion batteries.

It is well known that metallic anodes form a thick SEI layer in the presence of organic electrolyte[72–74]. The SEI layer formed in organic solvents is composed of two layers, a compact layer of inorganic compounds formed from the reduction of salt anions close to the metals surface and an outer, porous organic layer formed from decomposition of the organic solvent[75,76]. The composition and morphology of this layer has a strong influence on the subsequent plating/stripping behavior of the underlying metals when used as anodes in rechargeable secondary batteries[21,77]. Zinc metal provides an interesting opportunity to further investigate the influence of the porous organic layer on electrochemical behavior during galvanostatic cycling. Unlike alkali metals, Zn is stable in water which allows for the use of aqueous electrolytes. In aqueous electrolyte, Zn metal will not form an outer organic layer, therefor, the SEI layer will be composed of only a thin layer of inorganic salt reduction products on the surface[78]. For my project on deposition/dissolution behavior of Zn metal anodes, I began by galvanostatically cycling 4 symmetric cells systems: Li||Li, Na||Na, Zn||Zn in analogous perchlorate organic electrolytes ($M(ClO_4)_x$ in ethylene carbonate:dimethyl carbonate where M is Li, Na, or Zn) and a Zn||Zn cell with an analogous aqueous electrolyte (1 M aqueous $Zn(ClO_4)_x$). Symmetric cell behavior for Li||Li cells is well understood which facilitated interpreting the results from the Zn||Zn cells and allowed for comparisons between the 4 systems[79–81]. Then, to further investigate the role of the organic SEI layer on Zn metal anode performance, I cycled a Zn symmetric cell in organic electrolyte for 20 cycles to form an organic SEI layer and then removed the electrodes and placed them in an aqueous electrolyte cell for continued cycling. Lastly, I performed the reverse of this process by cycling Zn

electrodes in aqueous electrolyte for 20 cycles to form a thin inorganic SEI layer before switching to an organic electrolyte and resuming cycling. This project further elucidated the effects of an organic SEI layer on Zn metal anode cycling stability.

My second project involved repurposing soot from the combustion of diesel fuel as a potential anode material for Li-ion batteries. This study was motivated by the prevalence of filters and electrostatic precipitators for reducing the nanoscale particulate matter emissions form diesel engines[82–84]. These devices produce carbonaceous soot which needs to cleaned out after extended use. The collected carbonaceous soot is a toxic waste material with no commercial applications making it a prime target for repurposing in clean energy storage devices like Li-ion batteries. Depending upon their particle size and morphology, carbonaceous particles have been shown to store charge through either the typical intercalation process exhibited by graphite electrodes or through pseudocapacitive behavior[85–87]. Pseudocapacitance involves the adsorption of ions onto the electrode surface with an accompanying faradaic charge transfer[88]. Unlike intercalation, this process is not diffusion limited and enables pseudocapacitive electrodes to function at much higher charge/discharge rates than conventional intercalation electrodes. To test whether the annealed soot particles demonstrated this behavior, a cyclic voltammetry experiment involving a wide range of scan rates was conducted and used to quantify the contributions to charge storage from capacitive and diffusion limited mechanisms. Additional electrochemical testing of the material involved a long-term galvanostatic cycling experiment at a high charge/discharge rate of 4C (charge/discharge in 15 minutes) to evaluate the soot particles' capacity retention and a rate capability experiment at a range of very high charge/discharge rates to evaluate the soot electrode's rate performance. These electrochemical experiments were supplemented by an array of characterization techniques including XRD, XPS, and Raman spectroscopy. This project showed the potential of a toxic waste material, diesel combustion soot, as a novel electrode material for Li-ion batteries.

CHAPTER III

INVESTIGATING THE IMPACT OF THE SOLID-ELECTORLYTE INTERFACE LAYER IN THE FORMATION OF DENDRITES: CASE STUDY ON ZINC METAL ELECTRODES

(Manuscript will be submitted to J. Electrochemical Society)

D. Gregory[1], C. Britten[2], K. Walters[2] and Ö. Ö. Çapraz[1]

[1]The School of Chemical Engineering, Oklahoma State University, Stillwater, OK 74074

[2]The School of Chemical, Biological and Materials Engineering, University of Oklahoma, Norman, OK

3.1 ABSTRACT

The formation of dendrites is the bottleneck to harvest the high theoretical capacities of metal electrodes such as Li, Na, Mg and Zn in batteries. The critical current density, interfacial instabilities, and the characteristic of solid-electrolyte interface (SEI) layer play a major role on the formation mechanisms of dendrites. Unlike Li and Na metals, zinc can be electroplated in organic and aqueous electrolytes. In this study, we investigated the impact of SEI layer on the electroplating of zinc metals in organic and aqueous electrolytes by using electrochemical techniques coupled with electron microscopy. First, we characterized the voltage profile and morphological evolution of Zn metal electroplating in organic and aqueous electrolytes with $Zn(ClO_4)_2$ salt dissolved in either organic or aqueous solvents. The electrochemical response of Zn plating was compared with the ones for Li and Na metal plating by using analogous perchlorate $LiClO_4$ or $NaClO_4$ salt dissolved in the same organic solvent. Under the same charge conditions, cycle life of the metal electrodes was longer in the order of Li > Zn > Na. Cycle life of the Zinc metal electrodes cycled in aqueous electrolytes last almost two-times longer than the ones in organic electrolyte. The impact of the SEI layer is further investigated by electroplating Zn first in aqueous for 20 cycles, and then switching it to organic electrolytes and vice versa. The presence of the SEI layer due to decomposition of organic electrolyte species caused larger overpotentials during cycling and reduced cycle life from 220 to 160 cycles. On the other hand, when the Zn is first electroplated in aqueous electrolytes, cycle life of the Zn symmetric cells in organic electrolyte is almost three-fold longer than the ones cycled entirely only in organic electrolytes. Overall, our study demonstrated the impact of surface chemistry and morphology on the formation of Zn dendrites. The methodology established here can be used to study impact of electrolyte salt and additives on the formation of dendrites on metal electrodes.

3.2 INTRODUCTION

The Li-ion battery has been a tremendous success since its commercialization by Sony in 1991 with applications in portable electronics, renewable energy storage, and electric vehicles[16]. However, the practical charge storage capacity of the intercalation electrodes commonly used in commercial lithium-ion batteries is approaching its theoretical limit[89,90]. This imposes a restriction on the energy density of lithium-ions batteries and impedes progress towards developing batteries with higher energy density. One potential solution is to replace the graphite anode with a metal electrode. Instead of intercalating ions into a host structure, charge storage on metal anodes occurs through deposition/dissolution of metal ions on the electrode surface. With the elimination of an inert host structure, metal anodes feature much higher theoretical energy densities than traditional anodes. For example, the theoretical capacity of a Li metal anode (3860 mA h g^{-1}) is almost 10 times higher than graphite (372 mA h g^{-1}). Beyond Li batteries, sodium (1165 mA h g^{-1}) and zinc (820 mA h g^{-1}) anodes also feature high specific capacities as well. Additionally, the metal anode provides a source of metal ions to alternative battery geometries such as metal-air and metal-sulfur batteries which have very high theoretical capacities in comparison with metal-ion batteries.

Unfortunately, utilization of metal anodes in rechargeable metal batteries is limited due to severe performance loss and safety issues associated with the formation of dendrites. Uneven electrodeposition of the metal ions over the surface of metal anode leads to formation of dendrites[34,35,91]. These dendrites present a potential safety hazard in flammable organic electrolytes because, over repeated charge/discharge cycles, they can grow through the electrolyte and cause an internal short-circuit by contacting with the cathode[92]. The solid-electrolyte interphase (SEI) plays a crucial role on the electrodeposition of metal ions. These SEI layers forms due to the highly negative electrochemical potentials of metallic anodes which are higher than the lowest unoccupied molecular orbital (LUMO) of the electrolyte[19,20]. Even the small surface roughness on the SEI layers can cause distortion transportation of ions, leading to nonuniform metal ion electroplating[93]. The formation of new SEI layers continues unless the electrode is passivated by a desirable SEI layer that prevents electron transfer between the anode and the electrolyte. However, if the SEI is not elastic enough, it can break down during lateral expansion of metal volume during electrodeposition, causing the exposure of fresh metal surface to the electrolyte and therefore formation of new SEI layers. Also, during the stripping of metal ions from the dendrites, the process may lead to generation of "dead metal" by physically or electrically disconnected from the bulk electrode by dissolution of metal from the base of the dendrite[94–96]. The combination of

continuously forming SEI layers and production of "dead" metal lead to low Coulombic efficiencies in metal anode batteries and limits their reversibility and cycle life[40].

A variety of solutions to the dendrite problem have been proposed including artificial SEI layers[21,78,97–99], liquid electrolyte optimization and additives[53,100–103], solid-state electrolytes[104–107], 3D current collectors[108–110], pulsed current charging/discharging protocols[61], and rapid oxidation and reduction[111]. However, better understanding of the mechanism behind the dendrite formation is required to develop effective strategies to overcome dendrite problem in the metal anodes. Recently, Dasgupta and his group utilized in operando microscopy to correlate between voltage trace shape and morphology changes of the electrode during galvanostatic plating/stripping using symmetric Li cells[79,80,112]. This explanation was later extended to account for further voltage trace evolution over extended cycling and is a valuable resource for interpreting symmetric cell data[81]. More recently, Mandl et al utilized the similar approach to correlate morphology and voltage profiles for sodium anodes[96]. In all of these cases, the nature of the SEI layer formed on the anode surface played an important role in the performance and resulting overpotentials for the cells tested.

In this study, our objective is to understand the impact of the solid-electrolyte interface on the electroplating / stripping performance of Zn metal anodes. To achieve it, we first investigate the voltage profiles for three different metals (Li, Na, Zn) in symmetric cell configuration using same salt anions and organic electrolytes. Li and Na symmetric cells are used to compare with the Zn symmetric cell voltage profiles since correlations between voltage trace features and morphology changes in Li and Na symmetric cells are well understood. Lithium and sodium are both highly chemically reactive metals and cannot be used with aqueous electrolytes. On the other hand, Zn metal can be used in both aqueous and organic electrolytes. This is a very beneficial feature, as Zn metal will not form an SEI layer containing organic species in aqueous electrolytes which allows for determining the influence of organic species in SEI layers on voltage trace evolution and long-term cycling performance. To utilize this feature, Zn electrodes were first cycled in an organic perchlorate electrolyte (1 M $Zn(ClO_4)_2$ in 1:1 EC:DMC) and then transferred to aqueous electrolyte (1 M aqueous $Zn(ClO_4)_2$) for comparison to Zn electrodes cycled solely in aqueous electrolyte. Similar experiment is also performance by cycling it first in aqueous, and then switching it to organic electrolytes. SEM images were taken to characterize the morphology of the electrodes.

3.3 Experimental Methods

Sample Preparation: Lithium (99.9% metal basis), sodium (99.9%, metal basis) and zinc metals (99.9% trace metals basis) were purchased from Alfa Aesar and Sigma Aldrich, respectively. The

lithium and zinc metals were used as received. Na metals were prepared using the methodology described in our previous publication[113]. The sodium cubes were purchased in a mineral oil solution. They were cleaned with hexane in a glovebox in order to remove mineral oil. The cleaned sodium cubes were stored in a 1:1 (V:V) solution of ethylene carbonate (EC, anhydrous, 99%, Sigma Aldrich) : dimethyl carbonate (DMC, anhydrous, >99%, Sigma Aldrich) inside the glove box. During symmetric cell assembly, the sodium cubes were removed from the storage solution, dried using a paper towel, and the exterior surface of the cubes comprised of an oxidized layer was cut off using a stainless- steel scalpel. The newly cut piece was then placed in a plastic bag and rolled out into a thin film using a rolling pin.

Electrochemical Characterization: The electrochemical performance of Li, Na and Zn metals were investigated by using symmetric cells. Symmetric cells assembled by using CR2032 coin cells for organic electrolytes and lab-made Swagelok for aqueous electrolytes. All symmetric cells utilizing organic electrolytes were assembled in an Ar filled glovebox ((H_2O and O_2 concentrations < 1 ppm). Celgard polyethylene separator was used for Li symmetric cells. Borosilicate glass fiber separator (Whatman GF/D was used for Na and Zn symmetric cells. Organic electrolyte were prepared by dissolving 1M $LiClO_4$, $NaClO_4$ or $Zn(ClO_4)_2$ in EC:DMC solvent for Li, Na and Zn symmetric cells, respectively. Aqueous electrolytes were prepared by dissolving $Zn(ClO_4)_2$ in ultrapure water. The electrochemical stripping and plating of metals were conducted by applying galvanostatic cycles at |1| mA cm^{-2} for1 hour. Electrochemical impedance spectroscopy (EIS) was conducted on the pristine and cycled cells using a Biologic potentiostat equipped with EC-EC-lab® acquisition software with an amplitude of 50 μA cm^{-2} and a frequency range of 100 kHz to 100 mHz.

Structural and Morphological Characterization: SEM images were acquired from a FEI Quanta 600 field emission gun ESEM with Bruker EDS and HKL EBSD. Coin cells were disassembled using an MTI disassembly die set inside a glovebox under Ar atmosphere. Samples were transferred between the glovebox and the SEM chamber using a sealed SEM transfer container to minimize ambient air exposure. At the SEM, samples were transferred as quickly as possible between SEM transfer module and SEM vacuum chamber to minimize samples contact with oxygen or moisture in the air.

3.4 Results and Discussion

3.4.1 Galvanostatic Cycling Profiles of Li, Na and Zn Metals

Electrochemical performance of the Li, Na and Zn metals were characterized using symmetric cells during electrochemical charge / discharge galvanostatic cycles. Cycle is defined as one stripping / plating process of metal ions on the electrode. Between each plating/stripping half-cycle, the cell was in open circuit condition (no current applied) for 3 minutes. In order to minimize the role of anionic electrolyte species on the plating/stripping behavior, an analogous perchlorate salt ($LiClO_4$, $NaClO_4$, or $Zn(ClO_4)_2$) - containing electrolytes were used in all experiments. Li and Na symmetric cells were only tested in ethylene carbonate: dimethyl carbonate (EC: DMC) organic solvent. However, plating / stripping behavior of Zn anode was characterized in EC: DMC organic solvent and aqueous electrolyte. EC: DMC mixture is chosen as a model organic carbonate solvent because of its rich literature on Li and Na plating in this solvent[35,114]. Figure 3.1 demonstrates the voltage profile of Li vs Li, Na vs Na and Zn vs Zn symmetrical cells during plating / stripping at ± 1 mA/cm^2 current density. The potential hysteresis in the Li vs Li symmetrical cell initially reduced gradually to 0.114 V around 50 cycles. After that, the potential hysteresis continuously increased up to 0.2905 V at around 200 cycles before short-circuiting. In the case of Na plating, the potential hysteresis dramatically increased before reaching the cut-off voltage of 1 V on the 36th cycle. The potential hysteresis in the Zn vs Zn symmetrical cell in the organic electrolyte started around 0.3 V in the first and reduced to about 0.17 V after 10 cycles. The hysteresis was almost constant until around 65th cycle and the cell short-circuited around 90th cycle. On the other hand, in the aqueous electrolyte, the potential hysteresis reduced from 0.1 V to 0.07 V within first 10 cycles. The hysteresis was almost constant around 0.05 V until the cell was short-circuited around 225th cycle. Overall, when symmetric Li, Na and Zn cells were cycled under same current density and using analogous perchlorate salt, cycle life of the metal electrodes were longer in the order of Li > Zn > Na. Cycle life of the Zinc metal electrodes cycled in aqueous electrolytes was almost two-time longer than the ones in organic electrolyte.

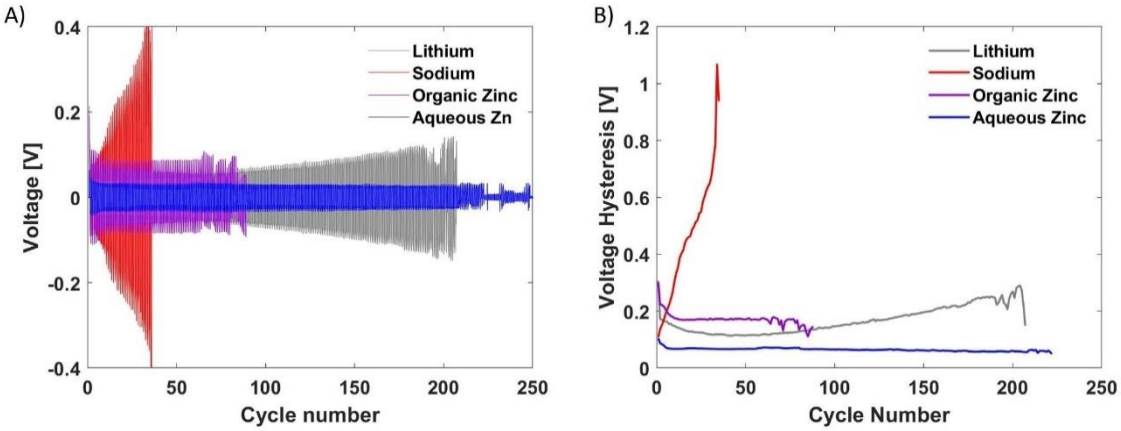

Figure 3.1: A) Galvanostatic cycling at 1 mA cm^{-2} voltage profile comparisons for Li metal, Na metal, Zn metal in organic electrolyte, and Zn metal in aqueous electrolyte. B) Voltage hysteresis comparison for the same symmetric cells.

3.4.2 Voltage Profile Observations

Voltage profiles during plating / stripping of metal electrodes provides information about the morphological changes on the metal electrode. Previous research efforts have linked evolution of the voltage profiles in Li and Na symmetric cells during galvanostatic cycling to morphological changes on the electrode surface[79,96]. The voltage profiles in Zn symmetrical cells, cycled in both aqueous and organic electrolytes, were compared with the voltage profiles in Li and Na symmetrical cells.

First charge: Initially, the symmetric cells consist of pristine metal electrodes. Although both electrodes are identical before cycling, in order to avoid confusion, the electrode is called as counter electrode where metal ions were generated at its surface during the first charge. The other electrode is called as working electrode where generated metal ions are plated on its surface. Li plating on the working electrode began with maximum cell voltage of 0.214 V and it gradually decayed to 0.082 V at the end of first charge cycle. The shape of the voltage evolution during the first lithium plating on the pristine Li metal electrode is very similar with the previous Li symmetric cells studies in the literature[115,116]. Dasgupta and his group provided a detailed correlation between the transient morphological changes on the Li metal electrodes and the voltage profile for each plating/stripping cycle using in-situ optical microscopy[79]. According to their studies, the initial maximum is correlated with overcoming the energy barrier associated with nucleating Li onto the cathode surface. A decay in the overpotential is then observed as the cathodic process switches from nucleating new Li deposits to plating Li on the existing deposits, a more kinetically favored process

requiring lower overpotentials. At the end of the first charge cycle, the counter electrode is pitted due to removal of Li from the initially pristine surface and working electrode has irregular Li deposits on its surface. The voltage profile during the first charge cycle in symmetric Zn cell cycled in organic electrolyte shows very similar behavior with the Li symmetric cell. Initial voltage of the cell was 0.184 V and it reduced to 0.109V. The initial voltage in the symmetrical Zn cell in aqueous electrolyte was lower compared to the zinc cell cycled in organic electrolyte. The voltage of Zn cell in aqueous electrolyte slowly decreased from 0.064 to 0.035V. In the case of Na, the voltage initially dropped from 0.048 to 0.043V within initial 10 minutes of the charge cycle, and then it slowly increased to 0.050V by the end of the charge cycle. The shape of the voltage evolution in the first discharge is similar in behavior with the subsequent charge and discharge cycles.

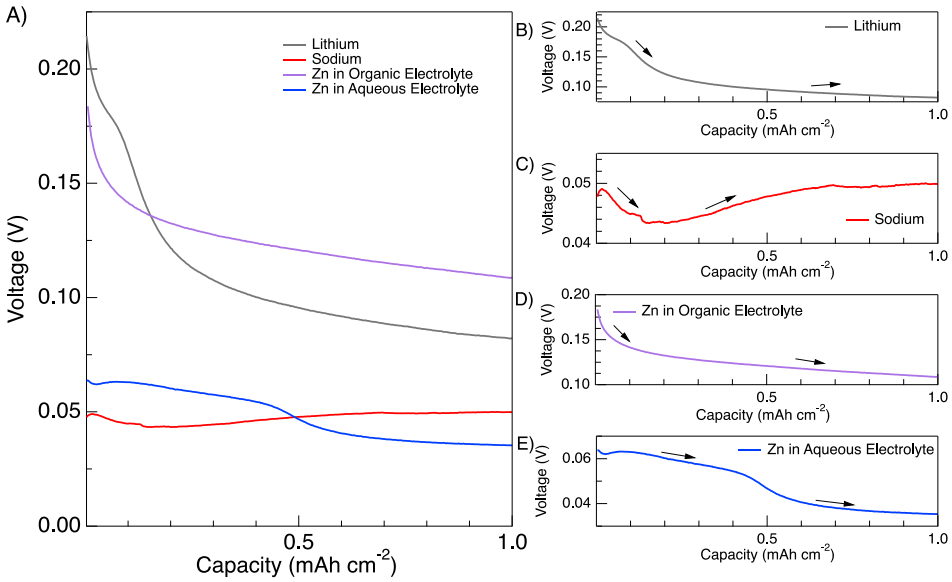

Figure 3.2: 1st galvanostatic half-cycle voltage profiles at 1 mA cm^{-2}. A) Comparison between Li, Na, Zn in organic electrolyte, and Zn in aqueous electrolyte symmetric cell. Voltage profiles for B) Li, C) Na, D) organic Zn, and E), aqueous Zn

***Fifth Charge*:** During the fifth charge cycle, the metal ions are generated on the previously plated counter electrode and they are plated on the working electrode. As the sign of the applied constant current was switched from negative (fourth discharge cycle) to positive (fifth charge cycle), the voltage of the symmetric cells jumped to 0.071 V, 0.083 V, 0.076 V and 0.035 V for Li, Na, Zn in organic electrolyte and Zn in aqueous electrolyte cells, respectively.

After the initial increase, the voltage of the Li symmetric cell decreased to local minima, 0.038 V within 28 minutes of applied current. From this minimum, the voltage increases again to a maximum value of 0.078 V where it plateaus after 58.5 minutes of applied current. Similar to the

first charge cycle, the initial maximum overpotential is required to overcome the nucleation potential on the surface of the counter electrode. Then, the potential gradually decreases as the plating mechanism switches from nucleation to growth of Li deposits[79]. Unlike the first charge, Li metals are stripped off from the dendritic depositions on the working electrode during the fifth charge cycle leading to volumetric shrinkage of the dendrites on counter electrode. Eventually, Li ions can no longer be generated from the dendritic deposits. Optical microscopy studies showed some of the dendrites on the counter electrode are either disconnected from the surface of the electrode or they become electrochemically inactive (observed as black color change in the optical studies)[79,112]. As a result, Li begins to be stripped off from the bulk surface of the working electrode. This point is correlated with the localized minima in the voltage profile. From this point, the location of the stripped Li will begin to transfer from the bulk surface to the newly created pits on the surface. These pits have different SEI compositions and thicknesses from the bulk surface making them more favorable for stripping. Therefore, the transition from bulk stripping to pit stripping is represented through the increase in overpotential.

In the case of Na plating / stripping in Na symmetric cell, the initial voltage peak of 0.0828 V is followed by a sharp drop in the voltage to a value of 0.043 V within the first 10 minutes. A notable difference in the two alkali metals is that the cell voltage reaches the first voltage plateau much quicker in the Na symmetric cell than the Li. After the plateau, voltage increased to its second peak value of 0.094 V after 25 minutes before plateauing at 0.090 V. A similar observation was recorded by Mandl et al in their symmetric cells alongside in-situ optical microscopy video footage[96]. The differences in voltage evolution between Na and Li symmetric cells associated to a larger amount of "inactive" Na being formed than "inactive" Li under similar conditions thereby providing less active metal to strip from the electrochemically active dendrites. After the 2nd voltage peak, voltage gradually decreased in the Na symmetrical cell and it was associated with Na ions being extracted from the pitted areas.

The Zn symmetrical cell cycled in organic electrolyte also displayed an analogous overall shape in its voltage trace. However, the first voltage peak is much less pronounced (an initial maximum value of 0.076 V followed by a minimum of 0.072 V after 6 minutes. There is a more gradual increase in overpotential to a final maximum value of 0.105 V. Also, the maximum overpotential was not yet reached in Zn cell although it was charged similar amount with Li and Na cells (1 mAh cm^{-2}).

In the case of symmetric Zn cell cycled in aqueous electrolyte, the first voltage peak was much broader than the voltage peaks in Li, Na and Zn cells cycled in organic electrolyte eventually reaching a value of 0.036 V after 6.5 minutes before decreasing. After the initial voltage peak, the evolution of voltage resembles metal electrodes cycled in organic electrolytes. Afterwards, the voltage dropped to its minimum value ,0.031 V, and slowly increased up to 0.036 V at the end of the half-cycle. However, it is important to note that potential change from initial peak to plateau is only 0.005 V, similar to the organic zinc cell with a drop of 0.004 V, whereas potential drop from the initial peak to plateau in Li and Na symmetrical cells in organic electrolyte is 0.033V and 0.040 V, respectively.

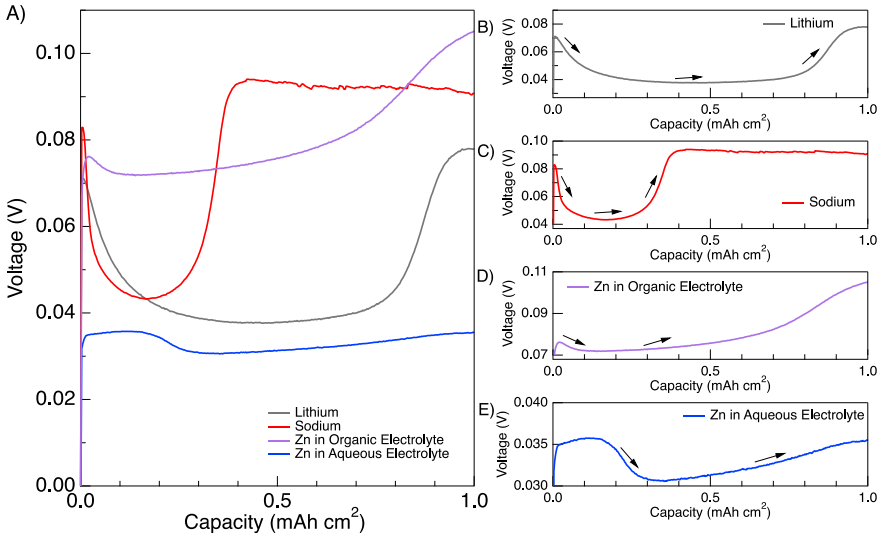

Figure 3.3: Fifth charge cycle voltage profiles at 1 mA cm^{-2}. A) Comparison between Li, Na, Zn in organic electrolyte, and Zn in aqueous electrolyte symmetric cell. Voltage profiles for B) Li, C) Na, D) organic Zn, and E), aqueous Zn

Later Cycles: Figure 3.4 shows the voltage profiles in Li, Na and Zn symmetrical cells during 1st, 2nd, 5th, 10th, 20th, 75th, 100th and 150th cycles from Figure 3.1. A distinct evolution in the voltage trace for each cell can observed over longer cycling. In the Li symmetric cell, the voltage dipping between the two potential peaks becomes shallower over extended cycling. The minimum half-cycle voltage increased from 0.038 V in cycle 5 up to 0.052 V in cycle 100. An accompanying decrease in the first voltage peak from 0.071 V to 0.064 V and the second voltage peak from 0.078 V to 0.072 V is also observed between the 5th and 100th cycle. A decrease in cell polarization during initial cycling is commonly reported in the literature and is attributed to the formation of higher surface area lithium deposits and lowered interfacial impedances[81]. Additionally, the initial peak broadened over extended cycling. Whereas the peak was reached within the first 10 seconds in the fifth cycle, it took 3 minutes before the local maximum was reached in cycle 100. Over further cycling, this voltage minimum disappears and the overall shape switches from peaking behavior to the arcing shape and increased overpotentials discussed by Chen et al[81]. This evolution was attributed to accumulation of dead Li within the cell which imposes Li-ion mass transport limitations. The switch from reaction kinetics limitations to mass transport-controlled behavior produced the more pronounced arcing behavior.

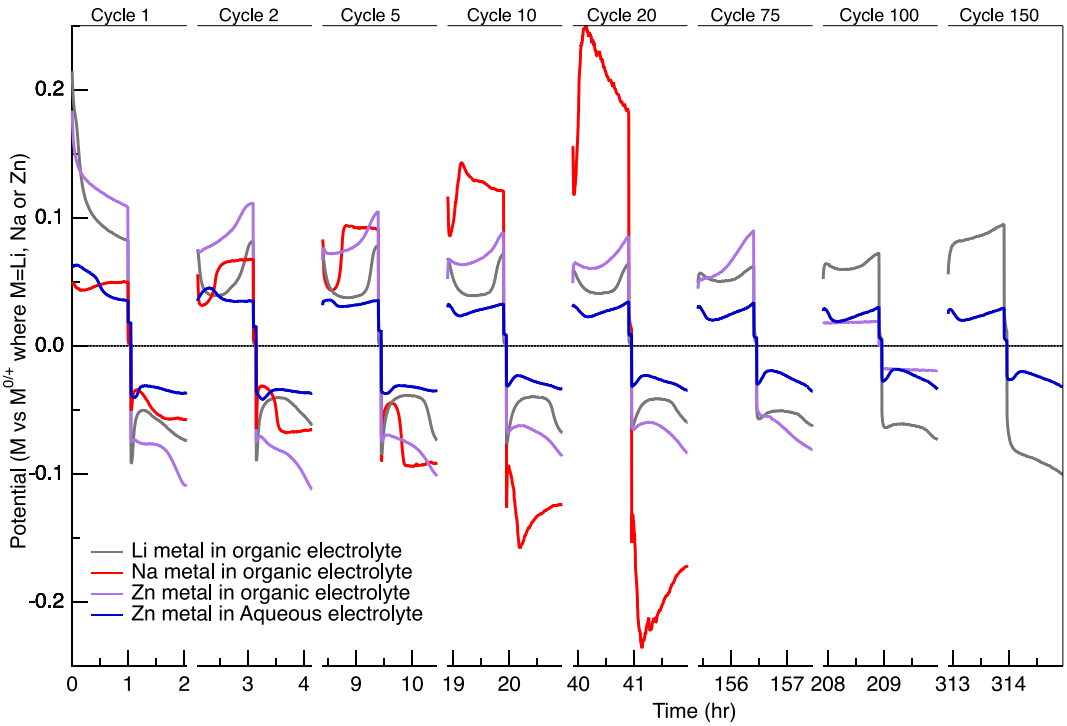

Figure 3.4: Galvanostatic cycling profiles from specific cycles for Li, Na, organic Zn, and aqueous Zn symmetric cells at 1 mA cm^{-2} showing the evolution of the voltage traces over extended cycling

The voltage profile of the Na symmetric cell rapidly changed over cycling. The 2nd voltage peak occurred progressively earlier with extended cycling and the voltage dip between the two peaks shrunk. The 2nd peak occurred at the 25-minute mark in the fifth cycle, but only after 13.5 minutes in cycle 20. Furthermore, the magnitude of the 2nd voltage peak increased dramatically over cycling. In cycle 5, the maximum potential was 0.094 V; however, this value increased to 0.251 V in cycle 20. The organic zinc cell's voltage profile remains relatively constant over prolonged cycling. The most prominent difference lies in the magnitude of the first voltage peak. The initial voltage peak has a value of 0.076 V in the fifth cycle which decreases to 0.054 V in cycle 75. In the case of the aqueous zinc cell, the initially broad first peak progressively narrows after many cycles. With the narrowing of this peak, the voltage profile of the aqueous zinc cell begins to resemble the lithium cell more closely, with a narrow initial peak followed by a dip in voltage, a second maximum, and lastly a voltage plateau.

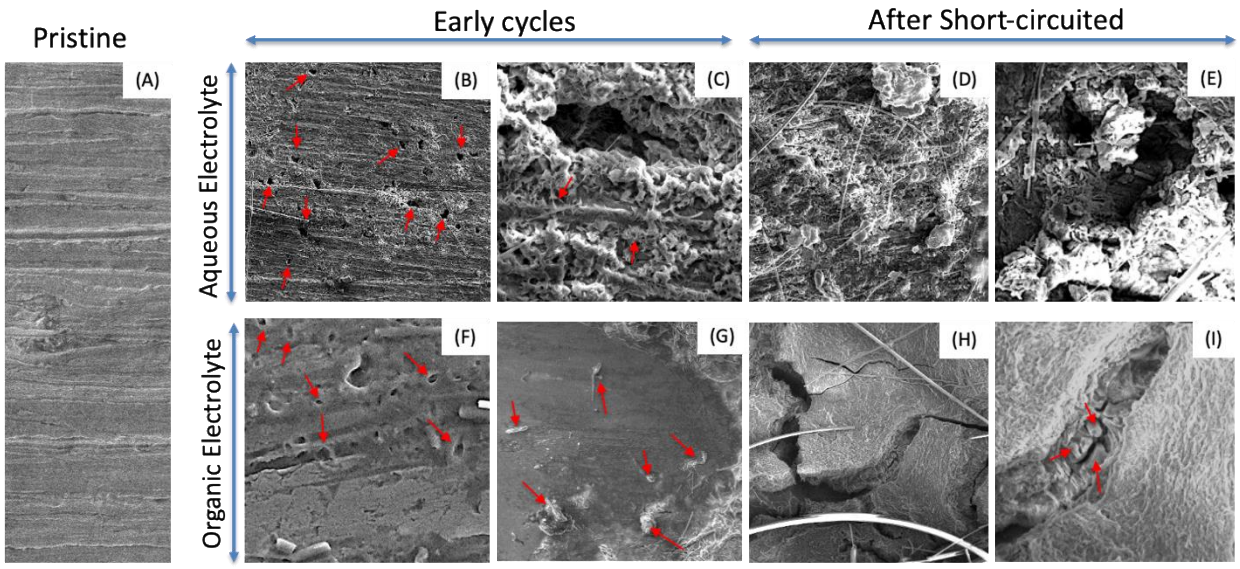

Figure 3.5: SEM images of (A) pristine Zn electrode, (B, C) Zn electrodes after 20 cycles in aqueous electrolyte, (D, E) Zn electrodes after short circuit in aqueous electrolyte, (F) Zn electrode cycled in organic electrolytes for 2 cycles, (G) Zn electrode cycled in organic electrolytes for 20 cycles, (H, I) Zn electrode after short circuited in organic electrolyte. Arrows demonstrated the representative morphologies such as pits (B and F) and dendrites (C, G, and I) in selected images.

***Morphological Evolution of Zn electrode*:** Morphology evolutions on Zinc metal anode was investigated by using scanning electron microscopy after cycling Zinc in either aqueous or organic electrolytes. Figure 3.5A shows the morphology of the pristine Zinc metal electrode. The needle-shaped dendrites were observed on the surface of the Zinc electrode when cycled in the aqueous electrolytes. On the other hand, mossy-type dendrite shapes were detected when cycled in organic electrolytes. In both electrolytes, the generation of pits was observed on the surface of the electrode

due to stripping of Zn from the metal surface. We also compared the final morphology of the Zinc electrodes after symmetric cells were short-circuited in organic or aqueous electrolytes. In the case of aqueous electrolytes, the dendritic deposits and pits further progress, and a large amount of dendritic deposits were captured on the electrode surface (Fig. 5 D and E). However, surface of the Zinc electrode was clearly covered by thick layer of solid-electrolyte interface when the electrode was cycled in the organic electrolytes (Fig 5H and I). Due to the volumetric expansion and contraction of the electrode during Zn plating/strippping, the SEI layer has fractured and large cracks are observed. Looking into these cracks reveals Zn dendrites growing up into the SEI layer. The presence of this pronounced SEI layer is the one of the most obvious difference between the electrodes cycled in the two electrolytes. This is to be expected as organic species in the electrolytes decomposes at lower potential and forms solid-electrolyte interface (SEI) later on the anode surface.

Open Circuit Potentials: Between each plating/stripping half-cycle, a 3-minute open circuit rest period is employed to allow the concentration of ions across the cell to approach equilibrium. This allows each half-cycle to start out with near equilibrium conditions for the surface reaction at each electrode. Metal ions are generated at one electrode and consumed at the other in the deposition/dissolution electron transfer reactions. The generation and consumption of metal ions at each electrode moves the concentration of ions away from equilibrium and introduces a concentration gradient across the cell. The severity of the concentration gradient depends on the effective diffusion coefficient of metal ions in the cell with greater mass-transport limitations inducing larger concentration gradients. As the interfacial concentration of metal ions at the surface of both electrodes changes, a larger overpotential is needed to drive the plating/stripping processes according to the equation[117]

$$U - U_{SHE}^{0} = U^{0} + \frac{RT}{nF} \ln \left(\frac{c_{ox}}{c_{red}}\right) \tag{3.1}$$

where U is the cell potential, U_{SHE}^{0} is the potential of the standard hydrogen electrode, U^0 is the standard potential of the cell, R is the gas constant, T is the temperature, n is the number of electrons involved in the electron transfer reaction, F is Faraday's constant, C_{ox} is the concentration of the oxidized species, and C_{red} is the concentration of the reduced species. When the half-cycle is completed and the symmetric cell becomes under the open-circuit condition, the concentration of ions across the cell is once again allowed to equilibrate, and the cell potential decreases as a result. The potential between the beginning and end of the open-circuit period is, therefore, directly related to the mass transport of ions from the surface of the electrode. A larger potential drop is indicative

of accumulation of greater ions on the electrode surface, causing larger concentration gradient in the cell.

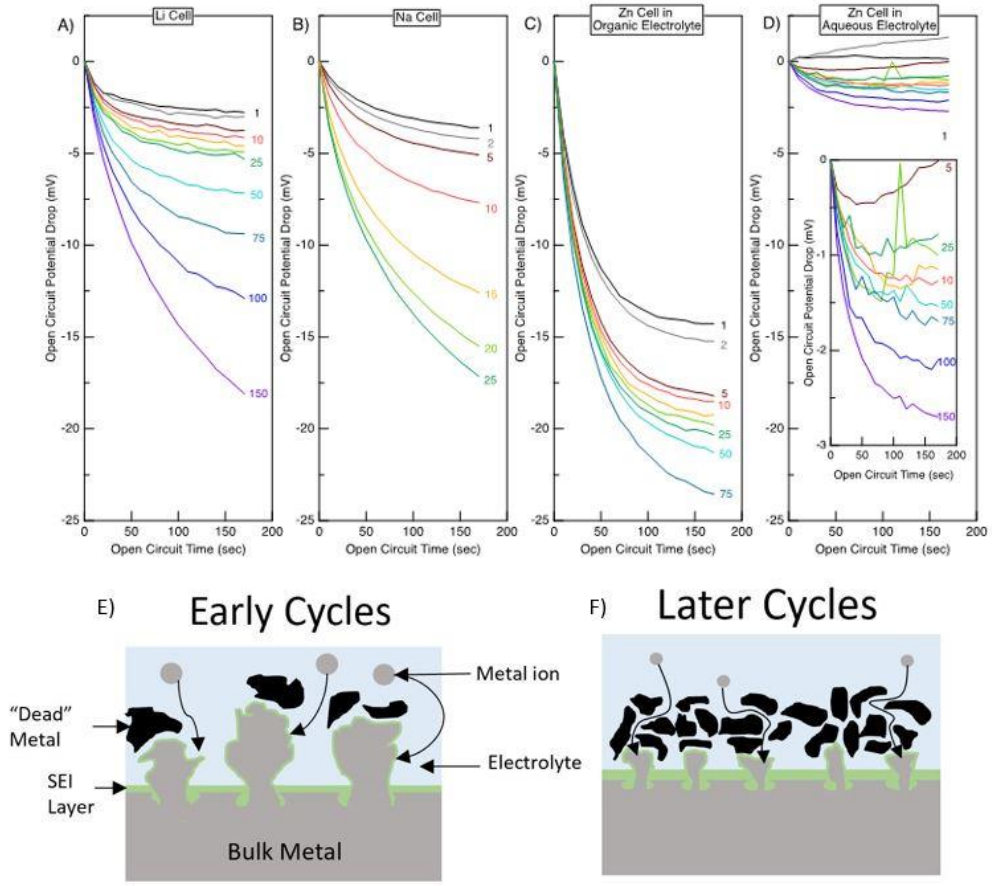

Figure 3.6: Open-circuit potential drops for selected cycles for A) Li, B) Na, C) Organic Zn, and D) aqueous Zn symmetric cells. Representation of metal ion diffusion pathways during E) early cycling and F) later cycling

Figure 3.6 shows the potential relaxations during open circuit conditions after selected cycles for the Li, Na, organic Zn, and aqueous Zn symmetric cells. In each case, there is an increase in the potential drop during the open circuit period with increased cycle number. The increased potential drops can be attributed to mass transport limitations. These limitations arise due to the buildup of "dead" metal on the surface of electrode as well as the formation of solid-electrolyte interface (SEI) layers. The accumulation of the dead metal and the formation of SEI layers material create a tortuous path for ions to reach the out the electrolyte (Figure 3.6 E,F). Therefore, increasing the diffusion length lowers the effective diffusion coefficient in the electrolyte according to the equation

$$D_{eff} = D\frac{\epsilon}{\tau} \tag{3.2}$$

where D_{eff} is the effective diffusion coefficient, D is the intrinsic diffusion coefficient, ε is the volume fraction of conductive phase of the electrolyte, and τ is the tortuosity factor[81]. For each metal, the open circuit potential drop follows an exponential decay over the rest period. The shape of this decay arises from the movement of ions within the cell towards equilibrium conditions according to Fick's first law

$$J = -D_{eff}\frac{dc}{dx} \tag{3.3}$$

where J is the mass flux of the metal ions, D_{eff} is the effective diffusion coefficient, c is the concentration of the metal ion, and x is the position in the direction perpendicular to the electrode surface. In cycle 1, the Li, Na, organic Zn, and aqueous Zn cells have a difference in potential of -2.76, -3.60, -14.3, and 0.15 mV, respectively, between the beginning and end of the open circuit relaxation period. The magnitude of these potential relaxations during open circuit progressively increased for each symmetric cell until cell failure for the all the organic cases. For the aqueous Zn cell, the drop in potential reaches a maximum of -2.70 V near cycle 150 before diminishing slightly over the remaining cycles. By the end of cycling, the total potential drops reached values of -28.3, -25.1, -24.5, and -2.33 mV for Li, Na, organic Zn, and aqueous zinc, respectively. The large potentials drops are only observed when the metal electrodes were cycled in the organic electrolyte.

This observation further verifies the correlation between accumulation of surface deposits on the metal electrode with transport limitations near electrode surface.

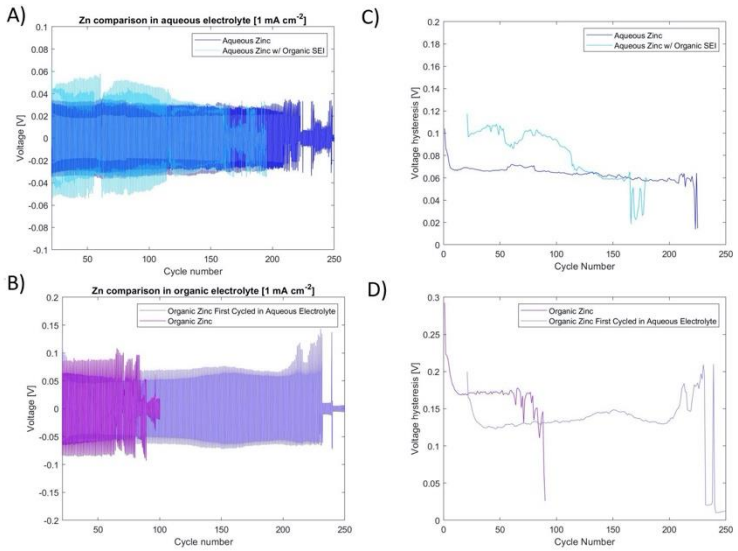

Figure 3.7: Galvanostatic cycling at 1 mA cm^{-2} voltage profile comparisons for A) aqueous Zn and aqueous Zn with organic SEI and B) organic zinc and organic zinc w/ inorganic SEI layer. Voltage hysteresis comparison for C) aqueous Zn and aqueous Zn with organic SEI and D) organic zinc and organic zinc w/ inorganic SEI layer.

3.4.3 Impact of Solid – Electrolyte Interface on Plating of Zn

The composition, thickness, and elasticity of the SEI layer on lithium and sodium electrode surfaces has a strong effect on the overpotentials during deposition/dissolution, long-term cycling stability, and plating/stripping Coulombic efficiencies[21,115,118]. Unlike Li and Na metal, Zn is compatible with organic and aqueous electrolytes which provides an opportunity to highlight the effects of organic SEI layers on deposition/dissolution behavior. In order to elucidate the SEI effect on metal plating, the symmetric cells were pre-cycled in organic or aqueous electrolytes for 20 cycles. Then, in some cases, the electrolyte solution was replaced from organic to aqueous electrolytes or vice versa. In the other cases, the cells were cycled in the same electrolyte as they were cycled in the first 20 cycles. To avoid confusion, we described the cells as follows; in the case, Zn metal electrodes were cycled for 20 cycles in organic electrolyte to form a thick SEI layer. Then, the electrodes were removed, placed into an aqueous Zn cell, and galvanostatically plated/stripped at constant 1 mA/cm^2. These cells are called as "aqueous Zinc w/organic SEI". If symmetrical cells are only cycled in aqueous electrolyte from the beginning, they are called as "aqueous Zinc". If zinc electrodes were first cycled for 20 cycles in 1 M aqueous $Zn(ClO_4)_2$ before being removed and replaced into a cell with 1 M $Zn(ClO_4)_2$ in EC:DMC electrolyte, the cell is called as "organic Zinc w/inorganic SEI". The symmetrical cell, which is only cycled in organic electrolyte, is called as "organic Zinc Cell".

The electrochemical performance of the aqueous Zinc w/organic SEI and aqueous Zinc were compared in Figure 3.7A. The presence of the organic SEI layer contributed to higher overpotentials during the first 100 cycles in the aqueous Zinc w/organic SEI cell. Also, there is a maximum polarization in aqueous Zinc w/organic SEI cell at cycle 45 is about 0.054 V, whereas maximum polarization in aqueous Zinc cell is 0.033 V at the same cycle. The overpotentials gradually decrease until the polarization in aqueous Zinc w/organic SEI cell becomes similar with aqueous Zinc cell at around cycle 120. However, aqueous Zinc w/organic SEI cell has a shortened cycle life and short circuits at around 160 cycles. For comparison, aqueous Zinc cell made it to about 220 cycles before shorting.

Solid electrolyte interface has a complex morphology and chemistry. It undergoes serious changes by increasing charging / discharging time. Also, it proposed to have two distinct layers, where more inorganic compounds form near electrode interface and the SEI is composed of more organic species on the electrolyte interface[21]. In the case of aqueous electrolyte, the formation of SEI layer on the surface of the electrode is much thinner and it only composes of inorganic species due to decomposition of salt[119]. To differentiate the impact of thin layer of inorganic SEI versus thick organic SEI, we also perform another set of experiments where symmetrical Zinc cell is initially cycled in aqueous electrolyte for 20 cycles, and then switched to organic electrolyte. The electrochemical performance of organic Zinc w/inorganic SEI cell is compared with organic Zinc Cell in Figure 3.7 C and D. An initial pre-cycling in aqueous electrolyte produced an improvement in the performance of the organic Zinc w/inorganic SEI cell. The maximum overpotential in organic Zinc w/inorganic SEI cell (0.067 V) was lower than the one for organic Zinc Cell (0.088 V) at cycle 45. Organic Zinc w/inorganic SEI cell short-circuited around cycle 230. However, cycle life of organic Zinc Cell as much less and it short-circuited around cycle 85. To understand the better performance of Zn cell when it pre-cycled in aqueous electrolytes, we compare the potential profiles during Li plating and stripping.

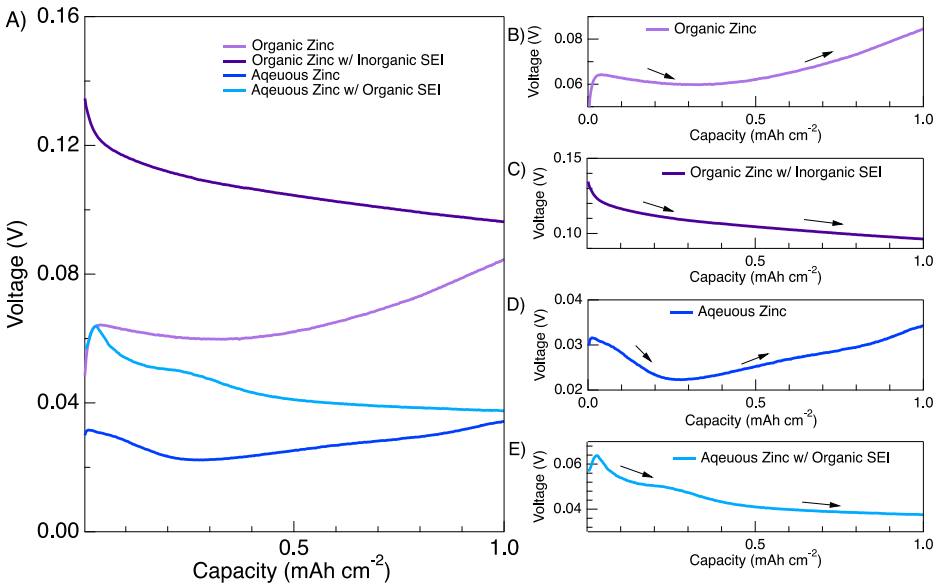

Figure 3.8: 21st charge cycle for a aqueous Zinc, organic Zinc, aqueous Zinc w/organic SEI, and organic Zinc w/inorganic SEI. Note that it is the first charge cycle for aqueous Zinc w/organic SEI, and organic Zinc w/inorganic SEI after changing the electrolyte.

First charge after changing the electrolyte: The voltage profiles during 21st cycle in aqueous Zinc w/organic SEI and organic Zinc w/inorganic SEI are shown in Figure 3.8. These symmetric cells were previously cycled 20 times in organic or aqueous electrolytes. 21st cycle is the first cycle after changing the electrolytes (from organic to aqueous or vice versa). Evolution of voltage profile is significant different between organic Zn cell and organic Zinc w/inorganic SEI cell. The behavior of voltage profile in organic Zinc w/inorganic SEI resembles with the behavior of organic Zn cell during the first charge cycle (Figure 3.2). Similar behavior is also observed in aqueous Zinc w/organic SEI cell where the potential did not reach its minimum value during charging yet.

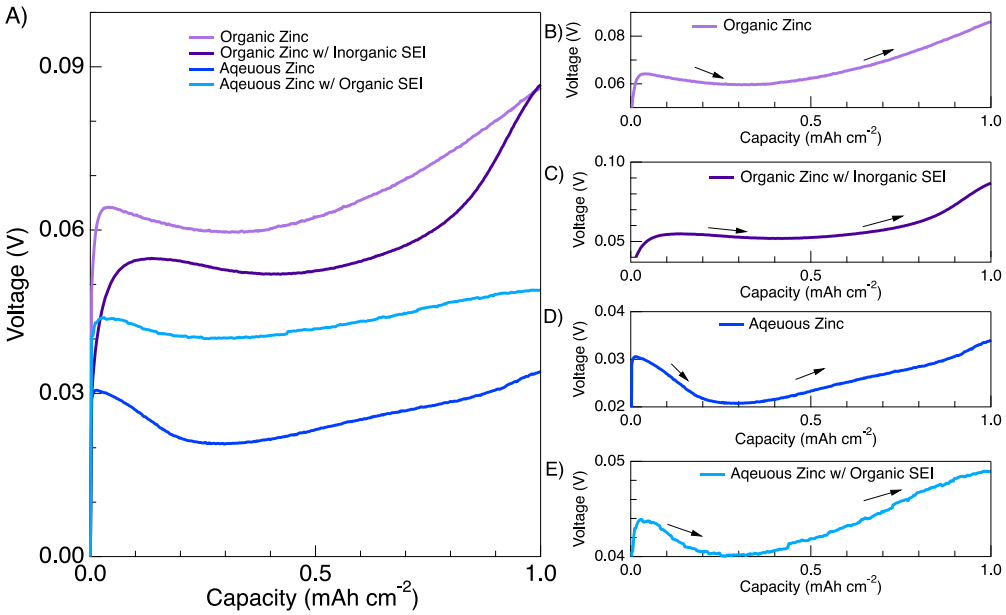

Figure 3.9: 25st charge cycle for an aqueous Zinc, organic zinc, aqueous Zinc w/organic SEI, and organic Zinc w/inorganic SEI. Note that it is the fifth charge cycle for aqueous Zinc w/organic SEI, and organic Zinc w/inorganic SEI after changing the electrolyte.

***Fifth Charge after changing the electrolyte*:** Figure 3.9 provides a comparison of the different Zn cells during the first half of the 25th cycle, which is the fifth cycle for Zn cells where the electrolytes were changed from organic to aqueous or vice versa. Organic Zinc w/inorganic SEI cell presents a broadened initial peak shape and reduced overpotentials throughout the half-cycle in comparison with organic Zinc cell. The broadened peak is accompanied by a shallower dip in voltage between the two peaks and a more severe increase in voltage towards the second peak. Neither cell reaches a final plateau stage at the end of the half-cycle but are still increasing in overpotential when the half-cycle ends. Aqueous Zinc w/organic SEI electrodes displays a narrower peak at the beginning of the half-cycle than the aqueous Zinc cell. Other than this minor distinction, both cells produce comparable voltage trace shapes with an initial peak followed by a shallow dip in voltage before a final voltage increase. An aqueous zinc w/organic SEI cell displays higher overpotentials throughout the entire half-cycle in comparison with aqueous zinc cell.

Later Cycles: Figure 3.10 shows the voltage profiles in the different Zn symmetrical cells during 1st, 2nd, 5th, 10th, 20th, 75th, 100th and 150th cycles from Figure 3.7. As compared to the organic Zn cell, the organic Zn w/ inorganic SEI cell retains its voltage profile over more extended cycling. In the case of the organic Zn cell, the voltage dip between the two maximums has largely disappeared by cycle 75; however, the organic Zn w/ inorganic SEI cell's voltage profile retains a small voltage dip even up to cycle 150. Furthermore, the dramatic voltage increases at the end of the later half-cycles of the organic zinc cell are not present in the organic Zn w/ inorganic SEI case which instead begins to level out over long-term cycling.

For the two aqueous Zn systems, extended cycling results in their voltage profiles becoming more alike. As described previously, the voltage trace of the aqueous Zn cell does not change substantially over long-term cycling. However, the voltage profile of the aqueous Zn with organic SEI does change noticeably over cycling and results in the growing similarity between the two. The presence of the organic SEI layer contributes to increased overpotentials during the initial cycling. These overpotentials reduce gradually until the voltage profile of the aqueous zinc with organic SEI and aqueous zinc cell begin to overlap by cycle 150. The aqueous zinc with organic SEI cell still displays slightly large overpotentials during the voltage dip portion of the half-cycles, but the two voltage profiles demonstrate similar profiles.

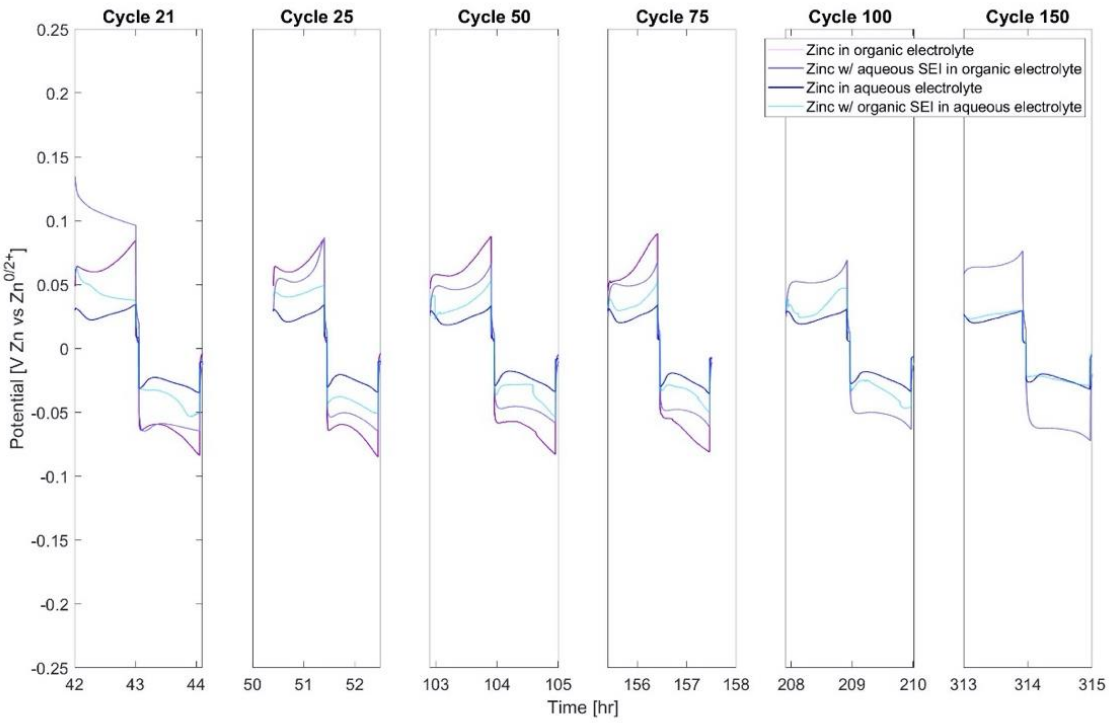

Figure 3.10: Galvanostatic cycling profiles from specific cycles for aqueous Zn, organic Zn, aqueous Zn w/organic SEI, and organic Zn w/inorganic SEI symmetric cells at 1 mA cm^{-2} showing the evolution of the voltage traces over extended cycling

Open Circuit Potentials*:* Figure 3.11 shows the open circuit voltage drops for the organic Zn w/ inorganic SEI and aqueous Zn w/ organic SEI symmetric cells after specific cycles. The initial potential drops for the aqueous Zn w/ organic SEI and organic Zn w/ inorganic SEI are 0.11 and 17.1 mV, respectively. Unlike the behavior in Figure 3.6, the magnitude of open circuit potential relaxations in Figure 3.11 do not steadily increase with cycle number. Instead, they reach a maximum in the initial cycles, before experiencing a decrease followed by an additional rise towards the end of cycling. In the aqueous Zn w/ organic SEI cell, this initial potential drop gradually rises to 4.1 mV by cycle 75, followed by a decrease to 1.58 mV by cycle 125, and finally an increase for the remainder of cycling up to 2.25 mV by cycle 180. The potential drop behavior during open circuit on the aqueous Zn w/ organic SEI cell suggest the deformation of organic SEI layer between cycle number 75 and 125. The increase in the potential drop between 125 and 180 is very similar to increase in potential drop in aqueous zinc cell within similar cycles. For the organic

Zn w/ inorganic SEI, the potential drop of 17.6 mV in the 21st cycle is the highest until around cycle 75 and is followed by a decrease in potential drop to 15.0 mV in cycle 30 and then an increase for the rest of cycling up to 53.3 mV at cycle 231.

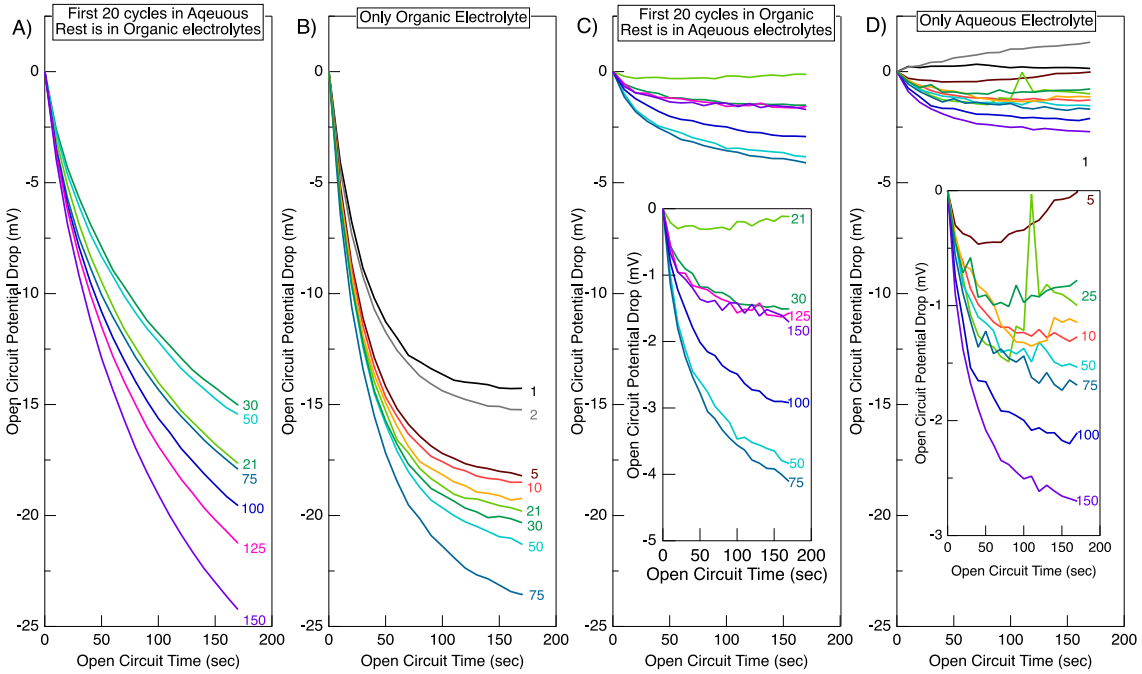

Figure 3.11: Open-circuit potential drops for selected cycles for A) organic Zn w/ inorganic SEI, B) organic Zn, C) aqueous Zn w/ inorganic SEI, and D) aqueous Zn symmetric cells

3.5 CONCLUSIONS

In this study, we compared the cycling performance of Li, Na, and Zn symmetric cells using the same anionic salt (ClO_4^-) in the electrolyte solution. Zn metal enabled us to investigate the influence of organic SEI layers on electrochemical performance by allowing us to use both carbonate and aqueous electrolytes. These symmetric cells were evaluated by cycling at 1 mA/cm^2 up to an areal capacity of 1 mA h cm^{-2} with open circuit periods of 3 minutes in between each half-cycle. This revealed that the cycling lifetime of the different systems followed the order aqueous Zn>Li>organic Zn>Na. Additionally, a different failure mechanism was noted in the Na cell compared to the other systems. Whereas the aqueous Zn, organic Zn, and Li symmetric cells failed by short-circuit over prolonged cycling, the Na symmetric cell failed due to a rapid rise in cell overpotential. This is likely due to drying up of the electrolyte owing to Na's high reactivity with the electrolyte and the significant buildup of "dead" Na in the cell imposing mass transport limitations. Observations of the voltage traces revealed that organic Zn cells cycled in organic electrolyte exhibit similar voltage features as Li cells which can be correlated with deposition/dissolution processes occurring on the surface. Extended cycling revealed a switch from

"peaking" to arcing voltage shapes for Li, Na, and Zn metals cycled in organic electrolyte. This observation agrees well with previous reports for Li and can be attributed to the buildup of a tortuous "dead" metal and SEI layer above the electrode surface which impedes metal ion diffusion and causes the cell's potential to switch from kinetically controlled to mass transport limited. The aqueous Zn cells showed much less pronounced changes in their voltage profile which is likely due to the absence of a porous organic SEI layer which would contribute to imposing mass transport limitations. Plots of the cell potential relaxations during the open circuit period after each half-cycle show an increase in potential drop for each of the 4 systems studied. The increase in potential relaxation can also be attributed to the buildup of a "dead" metal and SEI layer on the surface which increases the concentration gradient in the cell whenever a current is applied and slows relaxation of this potential gradient during the open circuit period. Notably, while the organic cells reached large potential relaxations of ~ 20 mV before failure, the aqueous Zn cell only reached a value of ~2.5 mV which supports the notion that the aqueous Zn cell is less mass transport limited.

Further investigation of the role of an organic SEI layer on electrochemical performance in Zn cells was conducted by creating either an inorganic or organic SEI layer on the surface of Zn electrodes by cycling for 20 cycles in aqueous or organic electrolyte, respectively. The electrolyte in the cell was then switched and electrochemical performance was evaluated. This procedure revealed that the addition of an organic SEI layer to aqueous Zn cells increases cell polarization and reduced cycle life from ~225 cycles to ~160 cycles. Cell polarization in these cells gradually decreased and became more like the voltage traces of aqueous Zn cells after extended cycling possibly indicating the breakdown of the organic SEI layer over time. A similar trend was noted in the potential relaxation drops during OC period for the aqueous Zn cells with organic SEI which had an increase in potential drop up to cycle 75 reaching a value of ~4 mV, but then experienced a decrease in potential drop for the remainder of cycling down to ~ 2 mV which agrees well with the potential drop in the aqueous Zn cell. The addition of an inorganic SEI layer to Zn electrodes cycled in organic electrolyte greatly increased cell lifetime from about 90 cycles to about 230 cycles and also reduced cell overpotentials.

These results demonstrate that similar correlations between voltage profiles and surface processes for Li and Na cells can be extended to describe Zn cells cycling in organic or aqueous electrolyte. This study also highlights the effects of the organic SEI layer formed during cycling in organic electrolyte on cell performance and shows that the organic SEI layer increases cell potentials and reduces cycle life in Zn cells.

ACKNOWLEDGEMENTS

Parts of this work were carried out in the Microscopy Laboratory, Oklahoma State University, which received funds for purchasing the equipment from the NSF MRI program.

CHAPTER IV

UTILIZING NANOSCALE PARTICULATE MATTER FROM THE COMBUSTION OF DIESEL FUELS AS A CARBONACEOUS ANODE ELECTRODE FOR Li-ION BATTERIES

(Manuscript is submitted to ACS Environmental Science and Technology)

Darrell Gregory[1], Sisi Yang[2], Cody Massion[1], Mileva Radonjic[1], Stephen Cronin[2],

Ömer Özgür Çapraz[1]

[1]The School of Chemical Engineering, Oklahoma State University, Stillwater, OK 74074

[2]Department of Electrical Engineering, University of Southern California, Los Angeles, CA 90089

4.1 ABSTRACT

According to the Environmental Protection Agency's National Emissions Inventory Report, hundreds of thousands of tons of particulate matter ($PM_{2.5}$) are released by diesel combustion per year[120,121]. The toxic $PM_{2.5}$ air pollution causes serious public health problems and is responsible for millions of worldwide deaths each year[122]. In this study, we investigate the electrochemical energy storage capability of annealed soot PM originating from diesel exhaust. Soot composite electrodes were utilized as anode electrodes and cycled against Li counter electrodes. X-ray diffraction and Raman spectroscopy showed the graphitized carbon structure of the annealed soot particles. The cycle life and rate-capability of the electrodes were investigated via galvanostatic cycling tests. The electrodes exhibited excellent rate performance with discharge capacities of 235, 195, 150, 120, and 80 mAh/g when cycled at rates of 1C, 2C, 5C, 10C, and 20C, respectively. The electrode demonstrated an initial discharge capacity of 154 mAh/g at 4C rate with a capacity retention of almost 77% after 500 cycles. Raman analysis confirms the retention of structural ordering in the soot carbon after 500 cycles. Kinetics analysis, obtained through cyclic voltammetry at different scan rates, indicates pseudocapacitive charging behavior in the soot composite electrode. Our study provides a viable pathway towards a sustainable energy-environment by converting an abundant toxic pollutant into a valuable electrode material for Li-ion batteries.

4.2 INTRODUCTION

The steady increase in the consumption of fossil fuels in modern society has caused several serious environmental and human health issues. The burning of fossil fuels not only produces carbon dioxide emissions, which are contributing to global warming and poisoning the world's oceans, but also releases toxic air-borne pollutants into the atmosphere[123,124]. For example, combustion of fossil fuels in diesel engines generates nanoscale particulate matter (PM) with an aerodynamic diameter lower than 2.5 μm (i. e. $PM_{2.5}$). According to Global Burden of Disease report, almost 3.2 million worldwide deaths per year are attributed to health diseases associated with $PM_{2.5}$ air pollution, making it the 6th highest risk factor for premature mortality[122]. The long-reaching adverse effects of this PM includes complications in infant development during prenatal period[125], mental illnesses[126], respiratory health[127] and cardiovascular health[128–130]. In particular, combustion-derived carbonaceous particles have been suggested in recent years to be up to 5 times more toxic than inorganic particulate compositions[131–133]. According to the Environmental Protection Agency's (EPA) 2017 National Emissions Inventory Report, approximately 123,000 tons of $PM_{2.5}$ were released by diesel combustion in the year 2017[120,121]. The combustion of diesel fuels in California alone produces more than 25,000 tons of toxic nanoscale particulate matter (PM) as a waste product every year[134]. This has captured the attention of global organizations such as the World Health Organization (WHO), which gives an average annual guideline of 10 $\mu g/m^3$ of $PM_{2.5}$ in their air quality guidelines[135]. Furthermore, this attention has prompted decision makers such as the Environmental Protection Agency (EPA)[136], Federal-Provincial Advisory Committee[137], and the European Union[138] to impose standards on the emissions of nanoscale particulate matter. For example, the Euro 6 update limited the emission of particulate matter to 0.01 g/kWh for heavy duty engines and 0.005 g/km for light-duty vehicles operating in Europe, and further, more stringent air quality standards are expected in the future. Effective implementation of these policies is key to control and mitigate $PM_{2.5}$ air pollution[139].

These requirements have necessitated the need for an improvement in the technology restricting diesel engine particulate emissions. Diesel particulate filters (DPFs) and electrostatic precipitators (ESPs) are common methods of reducing combustion engine emissions[82,83,140]. However, these DPFs become clogged over extended use and must be cleaned out. If not maintained properly, these filters can exert a large back pressure on the engine ultimately reducing engine efficiency. The carbonaceous waste soot collected from these filters is of limited use and mostly ends up as industrial toxic waste. Potential commercial application of the waste material is needed to transform it into useful chemicals for sustainability. Previously, we demonstrated the

application of diesel engine exhaust soot as a conductive additive for two different Li-ion battery cathode materials, lithium manganese oxide (LMO) and lithium iron phosphate (LFP)[141]. In the study presented here, we examine the electrochemical storage capability of carbonaceous particulate matter as an anode material for Li-ion batteries.

Li-ion batteries are pervasive in modern society with applications in cell phones, laptops, and power tools. The discovery of graphite anodes in the early 1990s lead to the commercialization of rechargeable lithium-ion batteries in 1991 because graphite allows reversible Li-ion insertion (i.e. intercalation) and removal from its structure. In recent years, a number of publications have come forth with various carbonaceous electrodes as alternatives to the graphite electrode from a variety of sources including prawn shells[142], corn stalk cores[143], rice husks[144], garlic peels[145], sweet potatoes[146], wheat flour[147], and soot from marine gas oil[86] among others.

In this study, we investigate the electrochemical performance of soot particles derived from the combustion of diesel fuel. The morphological and chemical structure of the soot particles were characterized using SEM, XPS and XRD analysis. The composite anode electrodes were fabricated by mixing the soot particles with conductive carbon and binder. The electrochemical behavior of the soot composite electrodes was characterized via cyclic voltammetry and impedance spectroscopy. The cycle life and rate-capability of the electrode was investigated via galvanostatic cycling tests. The electrode demonstrated 150 mAh/g capacity at 4C rate and capacity retention was almost 77% after 500 cycles. Excellent rate-capability of the soot electrode suggested pseudocapacitive charge behavior of the electrode, which was further investigated by conducting cyclic voltammetry over a wide range of scan rates and Raman spectroscopy studies.

4.3 MATERIALS AND METHODS

Recycled Particulate Matter: The details of the preparation of the soot particles were explained in detail in our previous publication[141]. Briefly, soot particles were collected from diesel engine exhaust using electrostatic precipitation. The collected particles were then annealed at 250 ^{o}C in air for 4 hours.

Electrode Fabrication: Annealed diesel soot particles were used as the active material in composite electrodes for electrochemical characterizations. The composite electrodes were fabricated by mixing the annealed soot particles with carboxymethyl cellulose sodium salt binder (CMC, Aldrich) and Super P® conductive carbon additive (Alfa Aesar) in an 8:1:1 mass ratio, respectively. First, the CMC binder was dissolved in ultrapure water and mixed for 10 min in a Thinky centrifugal mixer at 2000 rpm mixing speed. Next, the annealed soot particles and Super P®

conductive carbon were added to the binder mixture. The resulting slurry was mixed in a Thinky centrifugal mixer at 2000 rpm for 30 minutes. The slurry was then casted onto Cu foil (9 μm thick, >99.99%, MTI) using a doctor blade and allowed to dry under ambient room conditions.

Electrochemical Cycling: CR2032 coin cells were assembled using the composite electrode as a working electrode, Li foil (99.9% metal basis, Alfa Aesar) as a counter electrode, and Celgard polyethylene film as a separator. Electrolyte was prepared by dissolving 1 M $LiClO_4$ in 1:1 (v:v) ethylene carbonate (EC, anhydrous, 99%, Sigma Aldrich):dimethyl carbonate (DMC, anhydrous, >99%, Sigma Aldrich). Coin cell assembly and electrolyte preparation were both performed in a glovebox under an inert argon atmosphere with moisture and oxygen levels kept below 1.5 ppm. Galvanostatic cycling and cyclic voltammetry tests were conducted between 2.0 to 0.01 V vs $Li^{+/0}$ on an Arbin potentiostat/galvanostat (MSTAT21044). Lithiation refers to insertion of Li^+ ions into the composite electrode during the discharge cycle, and delithiation refers to the extraction of Li^+ ions from the composite electrode during the charge cycle.

During galvanostatic cycling, a constant current, I, is applied until the cell potential reaches the set minimum (0.01 V) or maximum (2.0 V) value. The C-rates in galvanostatic cycling were calculated using Faraday's law: $C - rate = \frac{Qm_{sp}}{I}$, where the theoretical capacity of graphite, Q is 372 mAh/g and m_{sp} denotes a mass of annealed soot particles in the composite electrode[148]. In all galvanostatic tests, coin cell batteries were first cycled 3 times to allow formation of solid-electrolyte interface (SEI) layers. The capacity retention and rate capability of the soot composite electrode was then investigated by conducting galvanostatic cycle experiments at various rates. The experiments were performed at least twice and the average values based on repeated experiments are presented in the paper.

During cyclic voltammetry, the cell potential was increased and decreased at a constant rate (μV/s) between 0.01 and 2.0 V vs $Li^{+/0}$. Cyclic voltammetry experiments were performed at different rates (between 25 and 2500 μV/s) to investigate the charging mechanism of Li ions into annealed soot particles. Electrochemical impedance spectroscopy (EIS) was conducted on the pristine and cycled cells using a Biologic potentiostat equipped with EC-EC-lab® acquisition software.

Structural and Morphological Characterization: X-ray diffraction (XRD) patterns were captured using a Bruker D8 Advance XRD with Lynxeye Detector. A Witec alpha300 Raman microscope was used to identify carbon related bands using a 532nm laser and a 50x objective lens with a power of 2.5-3.5 mW and integration time of 2.5s. X-ray photoelectron spectroscopy (XPS) measurements were taken with a Kratos Axis Ultra DLD spectrometer.

4.4 RESULTS AND DISCUSSION

4.4.1 Material Characterization: The structure and chemical composition of the diesel soot particles were characterized by using powder X-ray diffraction (XRD), Raman spectroscopy, and X-ray photoelectron spectroscopy (XPS) measurements. The crystal structure of the annealed soot particles was investigated using XRD, as shown in Figure 4.1A. It is a well-known phenomenon that the high number of structural defects in the layered structure of graphite produce strong distortions of the diffraction peaks[149,150]. This distortion cannot be avoided as it is an intrinsic feature of graphitized carbon. Despite this distortion, two diffraction peaks were observed near 24.7° and 43.8°, corresponding to the (002) diffraction peak for parallel graphene sheets and the (100) peak from the covalently bonded structure of carbon atoms within each graphene sheet, respectively[151]. These results suggest the presence of graphitized carbon in the structure of annealed soot particles. High-resolution XPS C1s spectra are shown in Figure 4.1B. The C1s spectrum is found to be a combination of three peaks at 285, 286 and 289 eV, which correspond to sp^2 C–C, C–OH, and O=C–O bonds, respectively[86,145,152,153]. The areal percentage of these peaks were calculated, and the percentage of sp^2 C–C, C–OH and O=C–O peaks were found to be 43.0, 27.8 and 29.2%, respectively.

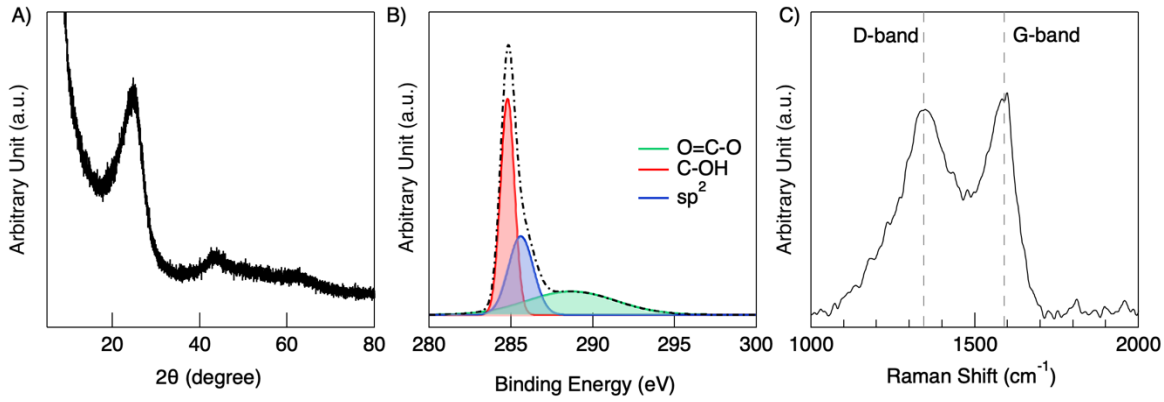

Figure 4.1: Characterization of Material Chemistry: A) XRD analysis of annealed soot powders, B) XPS spectrum of annealed soot powder, C) Raman spectrum of pristine soot composite electrode

The Raman spectra of the pristine soot composite electrode is shown in Figure 4.1C. The presence of two peaks, a D-band at ~1350 cm^{-1} and a G-band at ~1580cm^{-1}, is a distinctive feature of graphitized carbon. The first peak, at ~1340 cm^{-1} is caused by the A_{1g} vibration associated with defects in the aromatic rings and can be attributed to amorphization of the carbon structure[154]. The second peak at ~1580^{-1} is caused by the E_{2g} vibration of the sp^2 hybridized carbon atoms. The ratio of the intensity of these two peaks (I_D/I_G) is commonly used to evaluate the degree of disorder present in graphitized carbon[155,156]. For the pristine soot composite electrodes, the I_D/I_G ratio was

measured to be 0.94. The average particle size of the soot particles were measured to be around 20-30 nm[141].

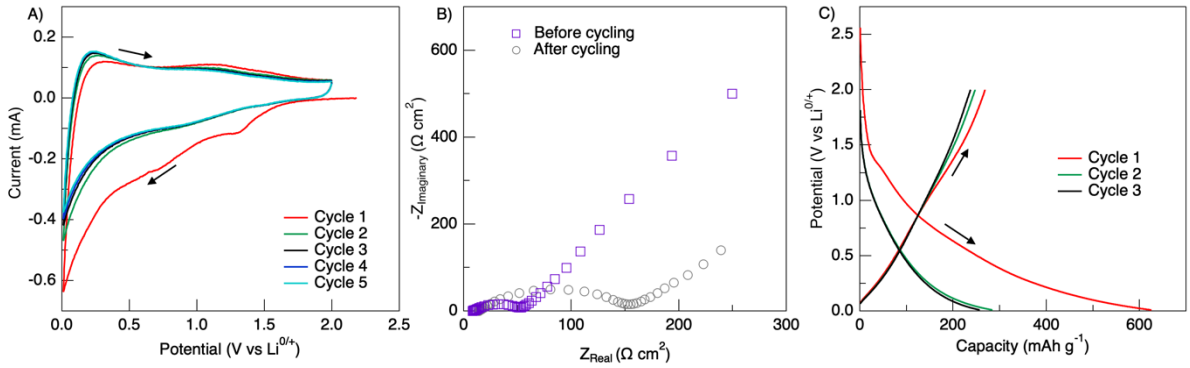

Figure 4.2: Electrochemical behavior of soot composite anode. A) Cyclic voltammetry at 200 µV/s for 5 cycles, B) Electrochemical impedance spectra of the composite electrode before and after 5 cycles cyclic voltammetry at 200 µV/s, C) Potential – capacity profiles during the first 3 galvanostatic cycles at C/2 rate.

4.4.2. Electrochemical Behavior of Soot Composite Electrode: The electrochemical properties of the soot composite electrodes were evaluated using a variety of electrochemical experiments, as shown in Figure 4.2. First, cyclic voltammetry (CV) was performed to investigate reversible and irreversible electrochemical reactions during the initial cycles[157]. During CV, the potential changes linearly with time at a constant rate between the two cutoff voltages. Figure 4.2A shows the current evolution during the first five cycles of CV between 0.01 – 2.0 V vs $Li/Li^{0/+}$ at a scan rate of 200 $\mu V\ s^{-1}$. During the first cathodic scan (i.e. potential sweep from higher potential to lower potential), a broader current peak was detected at 1.26 and 0.76 V. These peaks disappeared in the subsequent cycle, indicating that they are due to the formation of the solid-electrolyte interface (SEI) on the electrode from electrolyte decomposition[158]. Irreversible reduction current peaks were detected for various carbonaceous electrodes during the first cycle due to the electrolyte decomposition[85,159]. For carbonaceous electrodes, the cathodic peak between 0.01-0.2V is associated with reversible Li ion intercalation, and the anodic peak at around 0.25 V results from Li ion extraction from the host structure[146]. A similar electrochemical behavior is observed for the soot composite anode in Fig. 2A. A reversible and sharp cathodic peak was observed around 0.01 V in the first five cycles, associated with the lithiation of the soot composite electrode. During the anodic scan (i.e. increasing from lower potential to higher potential), a broad and reversible current peak was detected around 0.25 V in the first five cycles, indicating delithiation of the electrode. Interestingly, the current

profile of the electrode beyond the first cathodic cycle demonstrates a quasi-rectangular shape without pronounced redox peaks, indicating that the electrode material may possess a considerable pseudocapacitive contribution to charge storage[88]. We will discuss the capacitive behavior of the electrode by performing cyclic voltammetry at different scan rates in a later section of this manuscript.

Electrochemical impedance spectroscopy (EIS) is a common method for quantifying the relationship between current and voltage in an electrochemical cell through an equivalent circuit that represents physical processes occurring in the cell. EIS was applied to the composite electrode before and after cyclic voltammetry measurements, as shown in Figure 4.2B. The purpose of the EIS measurement is to investigate changes in the cell resistance. The surface resistance is associated with the electron transfer reaction occurring on the electrode's surface and it has a direct relationship with the radius of the real impedance portion of the semicircle. The radius of the semi-circle increased from 50.9 Ω/cm^2 before cycling to 150.7 Ω/cm^2 after five cycles. This increase indicates a higher resistance to the electron transfer reaction occurring on the electrode and can be a attributed to an increased resistance to Li^+ diffusion through the surface film caused by the formation and growth of the SEI layer[160].

The charge/discharge capacity of the electrode was analyzed by performing galvanostatic measurements at C/2 rate for the first 3 cycles, as shown in Figure 4.2C. C-rates are calculated based on the theoretical capacity of graphite (372 mAh/g). The composite electrodes display a large first cycle lithiation capacity of 625.3 mA h g^{-1}, which quickly reduced to 285 and 257 mA h g^{-1} during 2nd and 3rd lithiation cycles, respectively. During the first discharge cycle, the slope of the potential vs capacity curve changes dramatically at around 1.25 V. This observation further supports the contribution of SEI growth on the large discharge capacity in the first cycle. The large discharge capacity drop between the first and second cycle is attributed to the formation of an SEI layer on the electrode surface[87]. It also agrees well with the increase in the resistance in Figure 4.2B. The delithiation capacities during the first three cycles were 268, 247, and 237 $mAhg^{-1}$, respectively. Beyond the first discharge cycle, the potential–capacity curves show an almost linear relationship. This is in contrast to traditional graphite anodes which display a series of plateaus during galvanostatic cycling, caused associated by the phase transformations between different stages of graphite during (de)lithiation[149]. A quasi-linear relationship between potential and

capacity in the soot composite electrode suggests capacitive behavior of the electrode, which will be discussed later.

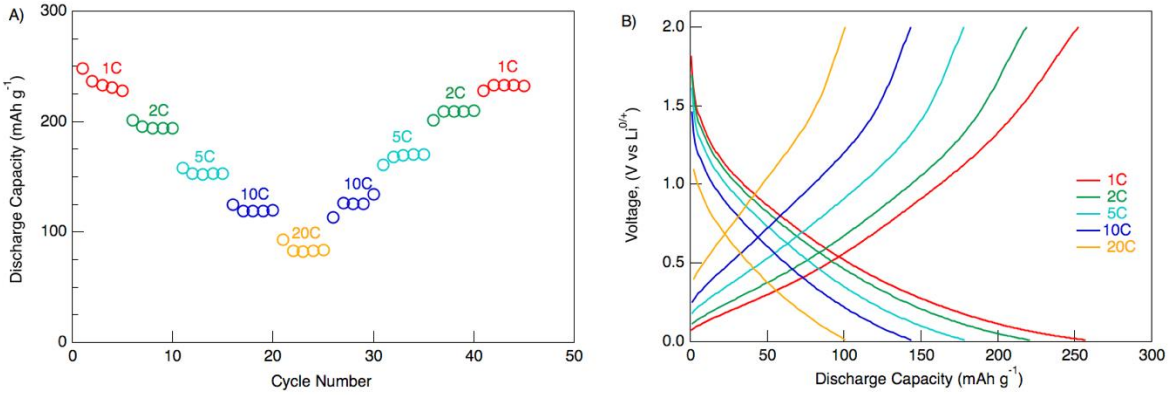

Figure 4.3: A) Rate performance of the electrode cycled at different C-rates, B) Potential – Capacity curves for charge and discharge cycles at different C-rates.

4.4.3 Rate Capability: The rate-capability of the soot composite electrodes was tested by performing galvanostatic cycling at different rates. Figure 4.3A shows the charge/discharge capacities and Coulombic efficiencies at 1 C, 2 C, 5 C, 10 C, and 20 C rates. The electrode was cycled for five consecutive cycles at each scan rate. The electrodes display excellent rate performance with charge capacities of 233, 194, 150, 118, and 82 mA h g^{-1} during the first cycle at C-rates of 1C, 2C, 5C, 10C, and 20C, respectively. Additionally, when the C-rate was restored to its initial value of 1C, a capacity of 229 mAh/g was retained which demonstrates the high reversibility of the charge storage. The potential–capacity plots for different scan rates are shown in the Figure 4.3B. The potential curves retains their shape with respect to capacity at various rates, and the potential profiles lack any distinct voltage plateaus, further indicating the capacitive charge storage mechanisms in addition to Li ion intercalation[149,161].

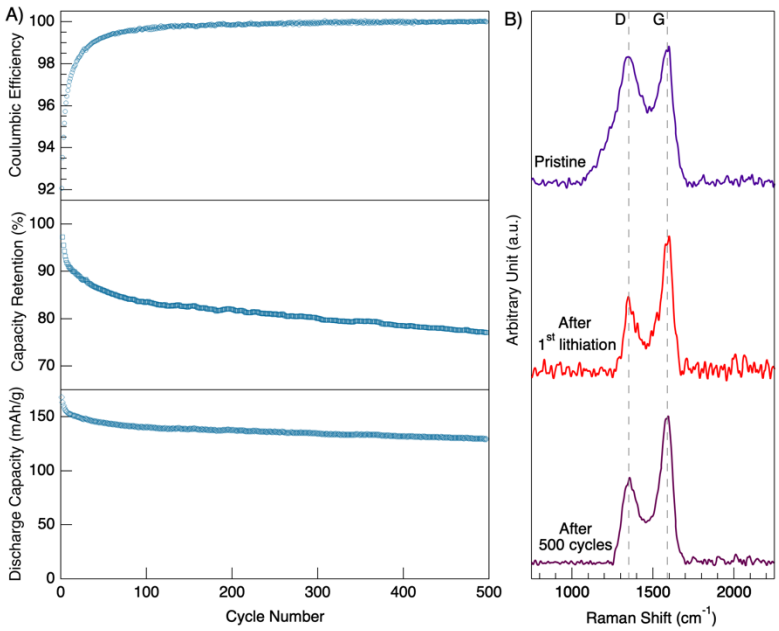

Figure 4.4: A) Columbic efficiency, capacity retention, and discharge capacity of the soot composite electrode cycled 4C for 500 cycles. B) Raman spectra of the electrode taken before cycling, after 1st lithiation and after 500 cycles.

4.4.4. Cycle Life of the Soot Composite Electrode: The cycle life of the soot composite electrodes was tested by performing long-term galvanostatic cycling. Figure 4.4A shows the average charge/discharge capacities, capacity retention, and Coulombic efficiency for soot electrodes cycled at 4C rate for 500 cycles. Before the cycle life testing, the electrode were charged/discharged three times for SEI formation and stabilization. The initial charge and discharge capacities of the electrode were 168 and 154 mAh/g, respectively, but decreased steadily throughout the initial 10-15 cycles. The charge and discharge capacities became reversible at 148 and 152 mAh/g after 15 cycles, respectively. The capacity retention was calculated by taking the ratio of the capacity at the current cycle over the first cycle: $\text{Capacity retention} = \frac{Q_n}{Q_1} \times 100\%$. The discharge capacity retention was about 90% by cycle 10 and decreased to 80% when the electrode was cycled 300 times, indicating highly reversible Li-ion storage ability of the soot composite anode. The coulombic efficiency was calculated as the ratio between charge extracted (delithiation, Q_{charge}) to charge inserted (lithiation, $Q_{discharge}$) for each cycle: $\text{CE} = \frac{Q_{charge}}{Q_{discharge}} \times 100\%$. The Coulombic efficiency rose steadily over cycling from its initial value and reaches 99.99% by cycle 500. Complimentary Raman analysis was conducted to better understand the high-capacity retention in the soot composite electrode. Figure 4.4B shows the Raman spectra of the pristine electrode, electrode after 1st lithiation and electrode after 500 cycles. The ratio of I_D/I_G decreased after the first

lithiation, demonstrating an increase in ordering of the soot carbon with Li intercalation. The I_D/I_G ratio does not change significantly between after 1st lithiation and after 500 cycles, indicating that structural ordering is retained in the soot carbon[162].

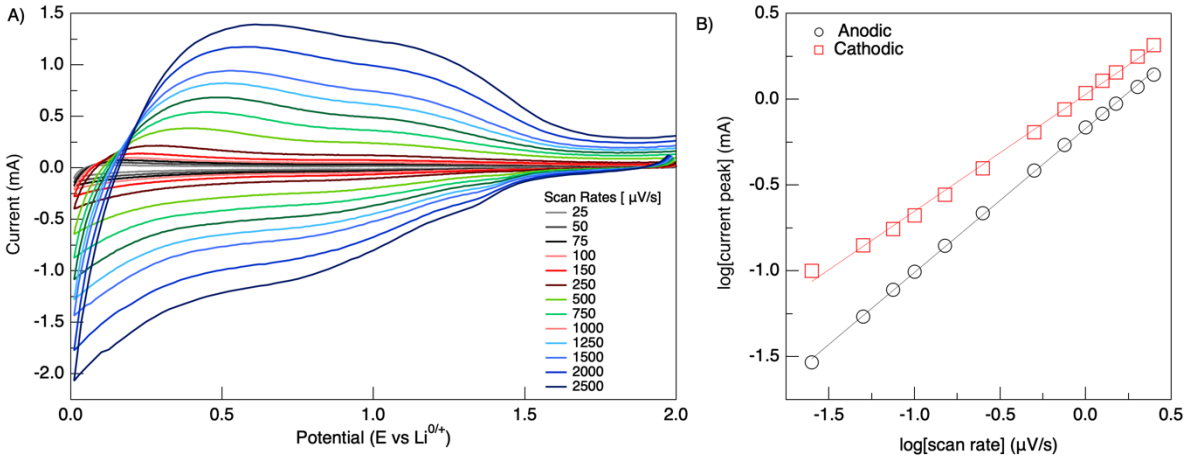

Figure 4.5: Li^+ charge storage mechanisms in soot composite electrode. A) CV curves of the electrode at various scan rates from 25 – 2500 µV/s. B) Relationship between current peak and scan rate.

3.4.5 Charging Kinetics of Li^+ in Soot Composite Anode: Cyclic voltammetry experiments were conducted at various scan rates to investigate the kinetics of lithium-ion storage in the soot composite electrode. Previous research efforts have utilized cyclic voltammetry to interrogate whether the charge storage mechanism in a material is based on intercalation or capacitive behavior[163–165]. By conducting CV at different scan rates, the difference in reaction kinetics between intercalation (which is diffusion-limited) and capacitive mechanisms can be exploited to ascertain their contributions to charge storage. The current response of the soot composite electrode cycled at a range of scan rates from 25 – 2500 µV/s is shown in Figure 4.4A. We can quantify the diffusion-controlled and surface capacitive-controlled contributions through the application of the following power law relationship between current and scan rate:

$$i = av^b \tag{4.1}$$

where *i* is peak current, *v* is the scan rate, and *a* and *b* are fitting parameters[86,152]. If the *b*-value is equal to 0.5, it indicates diffusion-controlled process charge storage behavior. On the other hand, if the *b*-value is equal to 1.0, then it suggests surface-capacitive controlled charge behavior in the electrode. Plots of log(|i|) vs log(|v|) were generated from the CV data, and the slopes of lines fitted

to the data were taken as the *b*-values for the peak currents in the cathodic and anodic sweeps (Figure 4.4B).

Based on these power-law fits, the *b*-values for the anodic and cathodic peaks were 0.84 and 0.68, respectively. These values suggest a combination of diffusion-controlled and surface-capacitive controlled mechanisms for the lithium-ion storage in the soot composite electrode. Further separation of the diffusion-controlled and pseudocapacitive mechanisms of charge storage was accomplished using the method of Dunn et al[166]. At each potential in the CV curve, there is a current contribution from both the intercalation and surface-controlled electron transfer reactions. The insertion process is diffusion limited and will vary with the square root of the scan rate according to the equation

$$i = nFAC^{*}D^{\frac{1}{2}}\left(\frac{\alpha nF}{RT}\right)^{\frac{1}{2}}\pi^{\frac{1}{2}}\chi(bt)\nu^{1/2} \tag{4.2}$$

where n is the number of electrons involved in the electron transfer reaction, F is the Faraday constant, A is the surface area of the electrode, C^{*} is the surface concentration of the electrode material, D is the chemical diffusion coefficient, α is the charge transfer coefficient, R is the ideal gas constant, T is the temperature, and $\chi(bt)$ is a function representing the normalized current for a totally irreversible system. In contrast, the surface-controlled mechanism will be directly proportional to the scan rate according to the following equation:

$$i = C_D A\nu \tag{4.3}$$

where C_D is the capacitance. At a fixed potential, the contribution of the diffusion-limited and capacitive processes on the current can be defined as:

$$i(V) = k_1\nu + k_2\upsilon^{0.5} \tag{4.4}$$

where k_1 and k_2 represent the capacitive and interaction contributions, respectively[88]. Therefore, if values of k_1 and k_2 are found over the range of potentials in the CV, then the individual contribution of each process can be identified. To assist with this, Eqn. 4.4 was re-arranged into the form:

$$\frac{i(V)}{\upsilon^{0.5}} = k_1\nu^{0.5} + k_2 \tag{4.5}$$

which allows for calculating k_1 and k_2 values from linear fits of $i(V)/\nu^{0.5}$ vs $\nu^{0.5}$ plots, where k_1 is the slope and k_2 is the y-intercept in Figure A1 at various potentials. The k_1 and k_2 values produced from the graphs in Figure 4.5A are provided in Table A1 alongside the R^2 value of the line fit to

the data points. These values are used to calculate the current produced from the capacitive processes according to the following equation:

$$i_{cap}(V) = k_1 \nu \tag{4.6}$$

The contribution of capacitive behavior to the current are plotted on top of the experimentally recorded current profiles when the electrode is cycled at 25 and 2500 μV/s in Figures 4.6A and 4.6B. Contributions of the capacitive charge storage are also presented for the other scan rates in Figure A2 in the Appendix. Figure 4.6C illustrates the overall contribution of capacitive and diffusion-controlled processes on the discharge capacity of the electrode at various scan rates. The relative contribution is calculated by numerically approximating the area under the curve of the overall current response and the capacitive current response using the trapezoidal rule at each scan rate and dividing the area of the capacitive current response by the overall current response, as follows: $\text{relative contribution} = \frac{A_{capacitive}}{A_{overall}} * 100\%$. At the slowest scan rate of 25 μV/s, the capacitive contribution is about 45.8% of the total charge storage, indicating that insertion is the primary contributor to the charge storage at this rate. However, with increasing the scan rate, the capacitive contribution significantly increases to account for 87.1% of the total charge storage when cycled at 2500 μV/s. The intercalation of Li ions into the electrode structure is a diffusion-controlled process unlike the pseudocapacitive mechanism which involves the adsorption of ions onto the electrode surface alongside an accompanying faradaic charge transfer. As a result, the surface-capacitive charge storage mechanism has much faster kinetics than the diffusion-controlled intercalation of Li ions into the annealed soot particles[88,161]. For this reason, the capacitive charge storage mechanism provides a larger contribution to charge storage at faster scan rates.

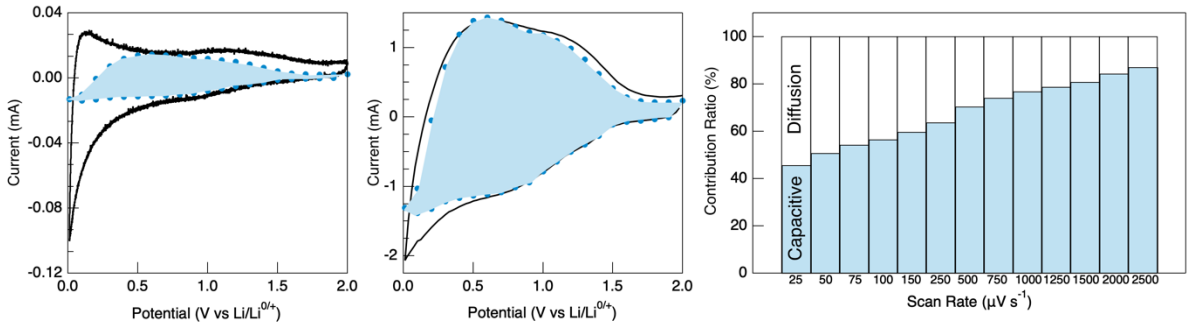

Figure 4.6: A, B) Current response (black straight line) and Capacitive charge storage contributions (colored with blue) at 25 and 2500 μV/s, respectively. C) Contribution ratio of diffusion-limited and capacitive factors on the charge storage at scan rates between 25.- 2500 μV/s.

4.5 CONCLUSION

In summary, we report the ability of annealed diesel soot particulate matter to store Li^+ ions as an anode electrode in Li-ion batteries. The structure and chemical composition of the annealed soot particles were characterized by X-ray diffraction, Raman spectroscopy, and X-ray photoelectron spectroscopy. The electrochemical behavior of the soot composite electrode was investigated by performing cyclic voltammetry, impedance spectroscopy, and galvanostatic cycling. The soot composite electrode demonstrated highly reversible discharge capacities when cycled at fast rates up to 20C. The electrode also demonstrated a remarkable capacity retention (77% after 500 cycles) with an initial discharge capacity of 154 mAh/g when cycled at 4C rate. Raman analysis on the cycled electrode shed light into structural retention of the soot electrode after 500 cycles. Cyclic voltammetry analysis at different scan rates demonstrated the pseudo-capacitive behavior of the soot electrode, which provided remarkable rate ability for fast charging.

The remarkable electrochemical performance of soot composite electrodes suggests new directions to ensure the provision of energy and protecting the environment at the same time. Although there has been a promising progress on electric vehicles, many other transportation vehicles such as Naval ships, large trucks, trains, and airplanes still heavily depend on fossil fuels with different variety of chemical impurities. Utilization of waste products from the combustion of fuels from these transportation vehicles into valuable products for electrochemical storage devices can reduce the release of toxic materials into earth's atmosphere and can promote the development of new electrode materials for energy storage devices.

ACKNOWLEDGEMENTS

Parts of this work were carried out in the Microscopy Laboratory, Oklahoma State University, which received funds for purchasing the equipment from the NSF MRI program.

CHAPTER V

CONCLUSIONS

5.1 SUMMARY

In summary, I completed two distinct projects over the course of my master's studies, investigating the role of an SEI layer on Zn deposition/dissolution alongside comparisons to Li and Na symmetric cells using an analogous electrolyte and evaluating the electrochemical performance of annealed soot from diesel engine exhaust as a potential anode material for Li-ion batteries.

In my project on deposition/dissolution behavior, I initially compared 4 systems: Li, Na, Zn symmetric cells using perchlorate salts in organic solvents as electrolyte and a Zn symmetric cell with an aqueous perchlorate electrolyte. I discovered that, in the presence of the same ionic species and organic solvent, Li has the highest galvanostatic cycling stability (~200 cycles before short circuit), followed by Zn (~90 cycles), and Na has the lowest (~35 cycles). Also, the failure mechanism was different between the Na cell and the other two, with the Na cell failing due to a rapid rise in overpotential and the Li and Zn cells failing due to short circuit. This difference could be due to the increased reactivity of Na metal with the organic electrolyte and production of larger amounts of "dead" Na during cycling imposing greater mass transport limitations at earlier cycles and drying up the electrolyte which would result in increasing overpotentials[96,118]. In contrast, the Li and Zn cells failed due to growth of metal dendrites off their surfaces creating a short circuit. Qualitative similarities were present in the voltage traces of Li and organic Zn cells which allowed for extension of correlations between voltage trace features and cell processes produced from earlier studies on Li metal to organic Zn symmetric cells. The aqueous Zn cell performed the best of the 4 systems with a cycle lifetime of ~220 cycles before short-circuiting. The behavior of the cell potentials during the open-circuit period between each half-cycle was also studied. The magnitude and shape of the potential decay during this period depends upon mass transport within the cell. The organic symmetric cells all experienced larger potential drops during the open-circuit period than the aqueous cell suggesting more severe concentration gradients during cycling which

can be attributed to the presence of an organic SEI layer on their surface and reduced ionic conductivity of the organic solvent impeding ion transport. Furthermore, the magnitude of the potential drop increased with increasing cycle number suggesting that the buildup and accumulation of a layer of "dead" metal on the electrode surface was further impeding ion diffusion. Further investigations were done to determine the role of the organic SEI layer on electrochemical performance by cycling Zn electrodes in organic electrolyte and then transferring them to aqueous electrolyte. These aqueous Zn with organic SEI cells showed reduced performance compared to the aqueous Zn cells with a reduced cycle life of ~160 cycles compared to ~220 cycles and increased overpotentials during cycling. Notably, the overpotentials for the aqueous Zn with organic SEI gradually decreased over cycling to resemble more closely those of the aqueous Zn cell possibly suggesting the degradation of the organic SEI layer due to repeated expansion/contraction of the anode surface. A reverse experiment was also conducted where an inorganic SEI layer was formed on the surface of Zn electrodes by cycling in aqueous electrolyte and then transferring the electrodes to organic electrolyte. The organic Zn with inorganic SEI cells vastly outperformed the organic Zn cells with an almost three-fold increase in cycle life before short circuit (~230 cycles up from ~90 cycles) and reduced overpotentials during cycling. A possible explanation for this is that the inorganic SEI layer formed on the surface suppresses electron transport between the electrolyte and the underlying metal anode preventing growth of an organic SEI layer and improving cycling performance. In conclusion, it was discovered that an organic SEI layer is detrimental to Zn anode plating/stripping stability and that the presence of an inorganic SEI layer protects the Zn metal surface and greatly increases cell lifetime in organic electrolytes.

For my second project, I tested the potential for recycling waste soot from diesel engine exhaust as Li-ion battery anode material. This was accomplished by performing both cyclic voltammetry and galvanostatic cycling experiments. I tested the capacity retention of the material by performing a long-term galvanostatic experiment with a high C-rate of 4C (15-minute charge/discharge) for 500 cycles. The initial discharge capacity of the composite soot electrodes after SEI formation and stabilization was 154 mAh/g which decreased to 129.6 mAh/g by cycle 500 for a capacity retention of 84%. Raman spectroscopy conducted on the composite electrodes before cycling, after first lithiation, and after 500 cycles revealed an increase in structural ordering in the soot electrodes upon first lithiation which was retained after 500 cycles. The rate capability of the composite soot electrodes was evaluated by running 5 cycles at sequential C-rates of 1 C, 2 C, 5C, 10 C, and 20 C resulting inaverage discharge capacities of 228.7, 199.7, 160.4, 123.2, and

82.6 mAh/g, respectively. These are very high C-rates (20 C is charge/discharge in 3 minutes) that extend to the limits of the kinetics capabilities of intercalation electrodes[167]. Cyclic voltammetry experiment at 200 μV/s for 5 cycles and galvanostatic cycling experiment at C/2 for 3 cycles were performed to study the behavior and reversibility of the electrochemical reactions. Interestingly, the cyclic voltammogram exhibited a quasi-rectangular shape with less pronounced redox peaks and the galvanostatic charge-discharge plots had linear profiles instead of the series of plateaus seen in graphite electrodes[149]. These two features, along with the excellent rate performance and capacity retention at high rates, suggest that the carbonaceous particles are storing charge via a pseudocapacitive mechanism in addition to intercalation of Li ions into the structure[161]. This capacitive behavior was further investigated by performing an additional CV experiment with scan rates ranging from 25 – 2500 μV/s. Ion intercalation is a diffusion limited process unlike pseudocapacitive charge storage, so varying the scan rate allows for differentiation of these two processes from their different kinetics[166]. This kinetics analysis confirmed a combination of diffusion and capacitive mechanisms for charge storage with an increase in the capacitive contribution to charge storage from 45.8% at 25 μV/s to 87.1% at 2500 μV/s. In summary, through a combination of galvanostatic cycling and cyclic voltammetry experiments, the electrochemical performance of diesel combustion soot was evaluated for Li-ion batteries. It was discovered that the composite soot electrodes displayed pseudocapacitive charge storage behavior in addition to intercalation behavior providing them with superior rate capability and showed that they have potential for use in applications requiring very quick charge/discharge times.

5.2 FUTURE WORK

There is potential to further explore the subjects of both projects. For the metal anode study, it would be useful to fabricate a custom electrochemical cell which allows for in-situ optical microscopy imaging of the electrode surface during plating/stripping like the setups used in literature for correlating voltage trace features to cell processes[79,103,112]. This would confirm assumptions about the Zn metal plating/stripping behavior and, to my knowledge, be the first time that correlations like those derived for Li and Na symmetric cells could be confirmed for Zn cells. Additionally, there are a diverse variety of artificial SEI layers that have been proposed for metal anodes. Further inquiries could involve studying the influence of these artificial layers on Zn metal anode electrochemical behavior. The testing and cell conditions for these SEI layers often vary considerably between different groups, so performing them with the same cell setup and standardized electrochemical testing procedures would aid in comparison between different artificial SEI layers.

In my second project, I demonstrated the application of annealed soot electrodes for Li-ion batteries. This study could be extended to look at the potential for soot composite electrodes in Na-ion and K-ion batteries. The larger atonic radii of Na and K cause greater distortions in the crystal lattice of electrodes during insertion which contributes to increased chemo-mechanical degradation in these materials[168]. The pseudocapacitive charge storage mechanism exhibited by the annealed soot electrodes would result in minimal changes in electrode structure which would be beneficial when utilizing larger cations. Additionally, the graphite anode used in commercial Li-ion batteries does not appreciably intercalate Na ions making identification of a Na-ion battery anode a critical issue[169].

REFERENCES

1. Andrew, M. G. & Weinlein, C. E. The Lead-Acid Battery—Demonstrating the Systems Design Approach to a Practical Electric Vehicle Power Source. *IEEE Trans. Veh. Technol.* **32**, 21–25 (1983).

2. Linden, D. & Reddy, T. *Handbook of batteries*. (McGraw-Hill, 2002).

3. Putois, F. Market for nickel-cadmium batteries. *J. Power Sources* **57**, 67–70 (1995).

4. Mayén-Mondragón, R., Ibanez, J. G., Vasquez, R. C., Baeza, A. & Oropeza, M. T. Electrochemical recovery of cadmium from simulated waste nickel-cadmium battery solutions. *Water. Air. Soil Pollut.* **194**, 45–55 (2008).

5. Coates, D. K. & Fox, C. L. Current status of nickel-hydrogen battery technology development. *J. Propuls. Power* **12**, 879–885 (1996).

6. Dunlop, J., Dunnet, A. & Cooper, D. Performance of INTELSAT V Ni-H_2 Batteries in Orbit (1983-1991). in *Proceedings of the 27th Intersociety Energy Conversion Engineering Conference* 1.117-1.125 (1992).

7. van Vucht, J. H. N., Kuijpers, F. A. & Bruning, H. C. A. M. Reversible room-temperature absorption of large quantities of hydrogen by intermetallic compounds. *Philips Res. Reports* **25**, 133–140 (1970).

8. Willems, J. J. G. & Buschow, K. H. J. From permanent magnets to rechargeable hydride electrodes. *J. Less-Common Met.* **129**, 13–30 (1987).

9. Ruetschi, P., Meli, F. & Desilvestro, J. Nickel-metal hydride batteries. The preferred batteries of the future? *J. Power Sources* **57**, 85–91 (1995).

10. Yoo, H. D. *et al.* Mg rechargeable batteries: An on-going challenge. *Energy Environ. Sci.* **6**, 2265–2279 (2013).

11. Selim, R., Hill, K. R. & Rao, M. L. B. Research and Development of a High Capacity, Nonaqueous Secondary Battery *First Quarterly Report*. (1965).

12. Pimentel, D. *et al.* Food production and the energy crisis. *Science* **182**, 443–449 (1973).

13. Whittingham, M. S. Electrical Energy Storage and Intercalation Chemistry. *Science* **192**, 1126–1127 (1976).

14. Mizushima, K., Jones, P. C., Wiseman, P. J. & Goodenough, J. B. Li_xCoO_2 ($0 < x \sim< 1$): A new cathode material for batteries of high energy density. *Solid State Ionics* **3**–**4**, 171–174 (1981).

15. Yoshino, A., Sanechika, K. & Nakajima, T. Secondary battery. (1986).

16. Li, M., Lu, J., Chen, Z. & Amine, K. 30 Years of Lithium-Ion Batteries. *Adv. Mater.* **30**, 1800561 (2018).

17. Taylor, S. & McLennan, S. The continental crust, its composition and evolution: an examination of the geochemical record preserved in sedimentary rocks. (Blackwell Scientific, 1985).

18. Olivetti, E. A., Ceder, G., Gaustad, G. G. & Fu, X. Lithium-Ion Battery Supply Chain Considerations: Analysis of Potential Bottlenecks in Critical Metals. *Joule* **1**, 229–243 (2017).

19. Xu, K. Electrolytes and interphases in Li-ion batteries and beyond. *Chem. Rev.* **114**, 11503–11618 (2014).

20. Peled, E. The Electrochemical Behavior of Alkali and Alkaline Earth Metals in Nonaqueous Battery Systems—The Solid Electrolyte Interphase Model. *J. Electrochem. Soc.* **126**, 2047 (1979).

21. He, M., Guo, R., Hobold, G. M., Gao, H. & Gallant, B. M. The intrinsic behavior of lithium fluoride in solid electrolyte interphases on lithium. *Proc. Natl. Acad. Sci. U. S. A.* **117**, 73–79 (2020).

22. Zhang, W. J. A review of the electrochemical performance of alloy anodes for lithium-ion batteries. *J. Power Sources* **196**, 13–24 (2011).

23. Jiang, X. *et al.* Tunnel-structured $Na_{0.54}Mn_{0.50}Ti_{0.51}O_2$ and $Na_{0.54}Mn_{0.50}Ti_{0.51}O_2$/C nanorods as advanced cathode materials for sodium-ion batteries. *Chem. Commun.* **51**, 8480–8483 (2015).

24. Zhu, Y., Xu, Y., Liu, Y., Luo, C. & Wang, C. Comparison of electrochemical performances of olivine $NaFePO_4$ in sodium-ion batteries and olivine $LiFePO_4$ in lithium-ion batteries. *Nanoscale* **5**, 780–787 (2013).

25. Yan, X. *et al.* Improved cycling performance of prussian blue cathode for sodium ion batteries by controlling operation voltage range. *Electrochim. Acta* **225**, 235–242 (2017).

26. Lin, D., Liu, Y. & Cui, Y. Reviving the lithium metal anode for high-energy batteries. *Nat. Nanotechnol.* **12**, 194–206 (2017).

27. Luo, Y. *et al.* Strategies for inhibiting anode dendrite growth in lithium-sulfur batteries. *J. Mater. Chem. A* **8**, 4629–4646 (2020).

28. Chung, S. H., Chang, C. H. & Manthiram, A. Progress on the Critical Parameters for Lithium–Sulfur Batteries to be Practically Viable. *Adv. Funct. Mater.* **28**, 1–20 (2018).

29. Ji, X. & Nazar, L. F. Advances in Li-S batteries. *J. Mater. Chem.* **20**, 9821–9826 (2010).

30. Manthiram, A., Fu, Y., Chung, S. H., Zu, C. & Su, Y. S. Rechargeable lithium-sulfur batteries. *Chem. Rev.* **114**, 11751–11787 (2014).

31. Guan, X. *et al.* Controlling Nucleation in Lithium Metal Anodes. *Small* **14**, 1–21 (2018).

32. Wang, K. X., Zhu, Q. C. & Chen, J. S. Strategies toward High-Performance Cathode Materials for Lithium–Oxygen Batteries. *Small* **14**, (2018).

33. Gallant, B. M. *et al.* Chemical and morphological changes of Li-O_2 battery electrodes upon cycling. *J. Phys. Chem. C* **116**, 20800–20805 (2012).

34. Xu, W. *et al.* Lithium metal anodes for rechargeable batteries. *Energy Environ. Sci.* **7**, 513–537 (2014).

35. Seh, Z. W., Sun, J., Sun, Y. & Cui, Y. A highly reversible room-temperature sodium metal anode. *ACS Cent. Sci.* **1**, 449–455 (2015).

36. Xiao, N., Mcculloch, W. D. & Wu, Y. Reversible Dendrite-Free Potassium Plating and Stripping Electrochemistry for Potassium Secondary Batteries. *J. Am. Chem. Soc.* **139** 9475-9478 (2017)

37. Yang, Q. *et al.* Dendrites in Zn-Based Batteries. *Adv. Mater.* **32**, 1–32 (2020).

38. Davidson, R. *et al.* Formation of Magnesium Dendrites during Electrodeposition. *ACS Energy Lett.* **4**, 375–376 (2019).

39. Jäckle, M., Helmbrecht, K., Smits, M., Stottmeister, D. & Groß, A. Self-diffusion barriers: Possible descriptors for dendrite growth in batteries? *Energy Environ. Sci.* **11**, 3400–3407 (2018).

40. Fang, C. *et al.* Quantifying inactive lithium in lithium metal batteries. *Nature* **572**, 511–515 (2019).

41. Okajima, Y., Shibuta, Y. & Suzuki, T. A phase-field model for electrode reactions with Butler-Volmer kinetics. *Comput. Mater. Sci.* **50**, 118–124 (2010).

42. Zhang, S. S. Role of $LiNO_3$ in rechargeable lithium/sulfur battery. *Electrochim. Acta* **70**, 344–348 (2012).

43. Ding, F. *et al.* Dendrite-free lithium deposition via self-healing electrostatic shield mechanism. *J. Am. Chem. Soc.* **135**, 4450–4456 (2013).

44. Yamaki, J. I. *et al.* A consideration of the morphology of electrochemically deposited lithium in an organic electrolyte. *J. Power Sources* **74**, 219–227 (1998).

45. Wang, D. *et al.* Towards High-Safe Lithium Metal Anodes: Suppressing Lithium Dendrites via Tuning Surface Energy. *Adv. Sci.* **4**, (2017).

46. Goodenough, J. B. & Kim, Y. Challenges for rechargeable Li batteries. *Chem. Mater.* **22**, 587–603 (2010).

47. An, S. J. *et al.* The state of understanding of the lithium-ion-battery graphite solid electrolyte interphase (SEI) and its relationship to formation cycling. *Carbon.* **105**, 52–76 (2016).

48. Ko, M., Chae, S. & Cho, J. Challenges in Accommodating Volume Change of Si Anodes for Li-Ion Batteries. *ChemElectroChem* **2**, 1645–1651 (2015).

49. Mukai, K. A series of zero-strain lithium insertion materials that undergo a non-topotactic reaction. *Electrochim. Acta* **263**, 508–514 (2018).

50. Verma, M. K. S. *et al.* A Strain-Diffusion Coupled Electrochemical Model for Lithium-

Ion Battery. *J. Electrochem. Soc.* **164**, A3426–A3439 (2017).

51. Hao, X., Lin, X., Lu, W. & Bartlett, B. M. Oxygen vacancies lead to loss of domain order, particle fracture, and rapid capacity fade in lithium manganospinel ($LiMn_2O_4$) batteries. *ACS Appl. Mater. Interfaces* **6**, 10849–10857 (2014).

52. Jaber-Ansari, L. *et al.* Suppressing Manganese Dissolution from Lithium Manganese Oxide Spinel Cathodes with Single-Layer Graphene. *Adv. Energy Mater.* **5**, 1–10 (2015).

53. Banik, S. J. & Akolkar, R. Suppressing Dendritic Growth during Alkaline Zinc Electrodeposition using Polyethylenimine Additive. *Electrochim. Acta* **179**, 475–481 (2015).

54. Glatz, H., Tervoort, E. & Kundu, D. Unveiling Critical Insight into the Zn Metal Anode Cyclability in Mildly Acidic Aqueous Electrolytes: Implications for Aqueous Zinc Batteries. *ACS Appl. Mater. Interfaces* **12**, 3522–3530 (2020).

55. Shen, C. *et al.* In Situ and Ex Situ TEM Study of Lithiation Behaviours of Porous Silicon Nanostructures. *Sci. Rep.* **6** (2016).

56. Mehdi, B. L. *et al.* Observation and quantification of nanoscale processes in lithium batteries by operando electrochemical (S)TEM. *Nano Lett.* **15**, 2168–2173 (2015).

57. Ma, C. *et al.* Interfacial Stability of Li Metal-Solid Electrolyte Elucidated via in Situ Electron Microscopy. *Nano Lett.* **16**, 7030–7036 (2016).

58. Li, J. & Dahn, J. R. An In Situ X-Ray Diffraction Study of the Reaction of Li with Crystalline Si. *J. Electrochem. Soc.* **154**, A156 (2007).

59. Lin, C. K., Ren, Y., Amine, K., Qin, Y. & Chen, Z. In situ high-energy X-ray diffraction to study overcharge abuse of 18650-size lithium-ion battery. *J. Power Sources* **230**, 32–37 (2013).

60. Courtney, I. A. & Dahn, J. R. Electrochemical and In Situ X-Ray Diffraction Studies of the Reaction of Lithium with Tin Oxide Composites. *J. Electrochem. Soc.* **144**, 2045–2052 (1997).

61. Maraschky, A. & Akolkar, R. Mechanism Explaining the Onset Time of Dendritic Lithium Electrodeposition via Considerations of the Li + Transport within the Solid Electrolyte Interphase. *J. Electrochem. Soc.* **165**, 696–703 (2018).

62. Gao, H. *et al.* Revealing the Rate-Limiting Li-Ion Diffusion Pathway in Ultrathick Electrodes for Li-Ion Batteries. *J. Phys. Chem. Lett.* **9**, 5100-5104 (2018).

63. Yuan, Y. *et al.* Regulating Li deposition by constructing LiF-rich host for dendrite-free lithium metal anode. *Energy Storage Mater.* **16**, 411-418(2019)

64. Nicholson, R. S. & Shain, I. Theory of Stationary Electrode Polarography: Single Scan and Cyclic Methods Applied to Reversible, Irreversible, and Kinetic Systems. *Anal. Chem.* **36**, 706–723 (1964).

65. Cao, X., Chuan, X., Li, S., Huang, D. & Cao, G. Hollow Silica Spheres Embedded in a Porous Carbon Matrix and Its Superior Performance as the Anode for Lithium-Ion Batteries. *Part. Part. Syst. Charact.* **33**, 110–117 (2016).

66. Liu, M. *et al.* Chemically Presodiated Hard Carbon Anodes with Enhanced Initial Coulombic Efficiencies for High-Energy Sodium Ion Batteries. *ACS Appl. Mater. Interfaces* **12**, 17620–17627 (2020).

67. Zhu, Y., Gao, T., Fan, X., Han, F. & Wang, C. Electrochemical Techniques for Intercalation Electrode Materials in Rechargeable Batteries. *Acc. Chem. Res.* **50**, 1022–1031 (2017).

68. Weppner, W. Determination of the Kinetic Parameters of Mixed-Conducting Electrodes and Application to the System Li_3Sb. *J. Electrochem. Soc.* **124**, 1569 (1977).

69. Wen, C. J. & Huggins, R. A. Thermodynamic and mass transport properties of "LiIn". *Mater. Res. Bull.* **15**, 1225–1234 (1980).

70. Li, J., Xiao, X., Yang, F., Verbrugge, M. W. & Cheng, Y. T. Potentiostatic intermittent titration technique for electrodes governed by diffusion and interfacial reaction. *J. Phys. Chem. C* **116**, 1472–1478 (2012).

71. Li, J., Yang, F., Xiao, X., Verbrugge, M. W. & Cheng, Y. T. Potentiostatic intermittent titration technique (PITT) for spherical particles with finite interfacial kinetics. *Electrochim. Acta* **75**, 56–61 (2012).

72. Lv, D. *et al.* Failure mechanism for fast-charged lithium metal batteries with liquid electrolytes. *Adv. Energy Mater.* **5**, (2015).

73. Liu, W., Liu, P. & Mitlin, D. Review of Emerging Concepts in SEI Analysis and Artificial SEI Membranes for Lithium, Sodium, and Potassium Metal Battery Anodes. *Adv. Energy Mater.* **10**, (2020).

74. Lu, Z., Schechter, A., Moshkovich, M. & Aurbach, D. On the electrochemical behavior of magnesium electrodes in polar aprotic electrolyte solutions. *J. Electroanal. Chem.* **466**, 203–217 (1999).

75. Peled, E. & Menkin, S. Review—SEI: Past, Present and Future. *J. Electrochem. Soc.* **164**, A1703–A1719 (2017).

76. Edström, K., Herstedt, M. & Abraham, D. P. A new look at the solid electrolyte interphase on graphite anodes in Li-ion batteries. *J. Power Sources* **153**, 380–384 (2006).

77. Meyerson, M. L. *et al.* The effect of local lithium surface chemistry and topography on solid electrolyte interphase composition and dendrite nucleation. *J. Mater. Chem. A* **7**, 14882–14894 (2019).

78. Liu, M. *et al.* Artificial Solid-Electrolyte Interface Facilitating Dendrite-Free Zinc Metal Anodes via Nanowetting Effect. *ACS Appl. Mater. Interfaces* **11**, 32046–32051 (2019).

79. Wood, K. N. *et al.* Dendrites and pits: Untangling the complex behavior of lithium metal anodes through operando video microscopy. *ACS Cent. Sci.* **2**, 790–801 (2016).

80. Wood, K. N., Noked, M. & Dasgupta, N. P. Lithium metal anodes: Toward an improved understanding of coupled morphological, electrochemical, and mechanical behavior. *ACS Energy Letters* **2**, 664-672 (2017).

81. Chen, K. H. *et al.* Dead lithium: Mass transport effects on voltage, capacity, and failure of

lithium metal anodes. *J. Mater. Chem. A* **5**, 11671–11681 (2017).

82. Boichot, R., Bernis, A. & Gonze, E. Agglomeration of diesel particles by an electrostatic agglomerator under positive DC voltage: Experimental study. *J. Electrostat.* **66**, 235–245 (2008).

83. Sudrajad, A. & Yusof, A. F. Review of electrostatic precipitator device for reduce of diesel engine particulate matter. *Energy Procedia* **68**, 370–380 (2015).

84. Walter, R., Neumann, J. & Hinrichsen, O. Extended Model for Filtration in Gasoline Particulate Filters under Practical Driving Conditions. *Environ. Sci. Technol.* **54**, 9285–9294 (2020).

85. Kim, M. S. *et al.* Ultra-high Li storage capacity achieved by hollow carbon capsules with hierarchical nanoarchitecture. *J. Mater. Chem.* **21**, 19362–19367 (2011).

86. Baek, H. M., Kim, D. Y., Lee, W. J. & Kang, J. Application of soot discharged from the combustion of marine gas oil as an anode material for lithium ion batteries. *RSC Adv.* **10**, 36478–36484 (2020).

87. Frackowiak, E., Gautier, S., Gaucher, H., Bonnamy, S. & Beguin, F. Electrochemical storage of lithium multiwalled carbon nanotubes. *Carbon* **37**, 61–69 (1999).

88. Augustyn, V., Simon, P. & Dunn, B. Pseudocapacitive oxide materials for high-rate electrochemical energy storage. *Energy Environ. Sci.* **7**, 1597–1614 (2014).

89. Thackeray, M. M., Wolverton, C. & Isaacs, E. D. Electrical energy storage for transportation - Approaching the limits of, and going beyond, lithium-ion batteries. *Energy Environ. Sci.* **5**, 7854–7863 (2012).

90. Whittingham, M. S. Ultimate Limits to Intercalation Reactions for Lithium Batteries. *Chem. Rev.* **114**, 11683–11720 (2014).

91. Chazalviel, J. N. Electrochemical aspects of the generation of ramified metallic electrodeposits. *Phys. Rev. A* **42**, 7355–7367 (1990).

92. Aurbach, D., Zinigrad, E., Yaron, C. & Hanan, T. A short review of failure mechanisms of lithium metal and lithiated graphite anodes in liquid electrolyte solutions. *Solid State Ionics* **148**, 405–416 (2002).

93. Cohen, Y. S., Cohen, Y. & Aurbach, D. Micromorphological studies of lithium electrodes in alkyl carbonate solutions using in situ atomic force microscopy. *J. Phys. Chem. B* **104**, 12282–12291 (2000).

94. Steiger, J., Kramer, D. & Mönig, R. Microscopic observations of the formation, growth and shrinkage of lithium moss during electrodeposition and dissolution. *Electrochim. Acta* **136**, 529–536 (2014).

95. Yoshimatsu, I., Hirai, T. & Yamaki, J. Lithium Electrode Morphology during Cycling in Lithium Cells. *J. Electrochem. Soc.* **135**, 2422–2427 (1988).

96. Mandl, M. *et al.* Sodium metal anodes: Deposition and dissolution behaviour and SEI formation. *Electrochim. Acta* **354**, 136698 (2020).

97. Chen, L. *et al.* Novel ALD Chemistry Enabled Low-Temperature Synthesis of Lithium Fluoride Coatings for Durable Lithium Anodes. *ACS Appl. Mater. Interfaces* **10**, 26972–26981 (2018).

98. Li, N. W., Yin, Y. X., Yang, C. P. & Guo, Y. G. An Artificial Solid Electrolyte Interphase Layer for Stable Lithium Metal Anodes. *Adv. Mater.* **28**, 1853–1858 (2016).

99. Zhao, Y. *et al.* In situ formation of highly controllable and stable Na_3PS_4 as a protective layer for Na metal anode. *J. Mater. Chem. A* **7**, 4119–4125 (2019).

100. Zhang, X. Q., Cheng, X. B., Chen, X., Yan, C. & Zhang, Q. Fluoroethylene Carbonate Additives to Render Uniform Li Deposits in Lithium Metal Batteries. *Adv. Funct. Mater.* **27**, 1605989 (2017).

101. Wang, G. *et al.* Suppressing dendrite growth by a functional electrolyte additive for robust Li metal anodes. *Energy Storage Mater.* **23**, 701–706 (2019).

102. Komaba, S. *et al.* Fluorinated ethylene carbonate as electrolyte additive for rechargeable Na batteries. *ACS Appl. Mater. Interfaces* **3**, 4165–4168 (2011).

103. Lee, B., Paek, E., Mitlin, D. & Lee, S. W. Sodium Metal Anodes: Emerging Solutions to Dendrite Growth. *Chem. Rev.* **119**, 5416-5460 (2019)

104. Zhou, W. *et al.* Plating a Dendrite-Free Lithium Anode with a Polymer/Ceramic/Polymer Sandwich Electrolyte. *J. Am. Chem. Soc.* **138**, 9385–9388 (2016).

105. Chen, L. *et al.* PEO/garnet composite electrolytes for solid-state lithium batteries: From "ceramic-in-polymer" to "polymer-in-ceramic". *Nano Energy* **46**, 176–184 (2018).

106. Zhou, W., Li, Y., Xin, S. & Goodenough, J. B. Rechargeable Sodium All-Solid-State Battery. *ACS Cent. Sci.* **3**, 52–57 (2017).

107. Zhao, N. *et al.* Flexible Hydrogel Electrolyte with Superior Mechanical Properties Based on Poly(vinyl alcohol) and Bacterial Cellulose for the Solid-State Zinc-Air Batteries. *ACS Appl. Mater. Interfaces* **11**, 15537–15542 (2019).

108. Zuo, T. T. *et al.* Graphitized Carbon Fibers as Multifunctional 3D Current Collectors for High Areal Capacity Li Anodes. *Adv. Mater.* **29**, 1700389 (2017).

109. Wang, Z. *et al.* Conducting Polymer Paper-Derived Mesoporous 3D N-doped Carbon Current Collectors for Na and Li Metal Anodes: A Combined Experimental and Theoretical Study. *J. Phys. Chem. C* **122**, 23352–23363 (2018).

110. An, Y. *et al.* Heteroatom-doped 3D porous carbon architectures for highly stable aqueous zinc metal batteries and non-aqueous lithium metal batteries. *Chem. Eng. J.* **400**, 125843 (2020).

111. Aleshin, A., Bravo, S., Redquest, K. & Wood, K. N. Rapid oxidation and reduction of lithium for improved cycling performance and increased homogeneity. *ACS Appl. Mater. Interfaces* **13**, 2654–2661 (2021).

112. Sanchez, A. J. *et al.* Plan-View Operando Video Microscopy of Li Metal Anodes: Identifying the Coupled Relationships among Nucleation, Morphology, and Reversibility. *ACS Energy Lett.* **5**, 994-1004 (2020)

113. Özdogru, B., Dykes, H., Padwal, S., Harimkar, S. & Çapraz, Ö. Electrochemical strain evolution in iron phosphate composite cathodes during lithium and sodium ion intercalation. *Electrochim. Acta* **353**, 136594 (2020).

114. Ding, F. *et al.* Effects of Carbonate Solvents and Lithium Salts on Morphology and Coulombic Efficiency of Lithium Electrode. *J. Electrochem. Soc.* **160**, A1894–A1901 (2013).

115. Bieker, G., Winter, M. & Bieker, P. Electrochemical in situ investigations of SEI and dendrite formation on the lithium metal anode. *Phys. Chem. Chem. Phys.* **17**, 8670–8679 (2015).

116. Wood, K. N., Noked, M. & Dasgupta, N. P. Lithium Metal Anodes : Toward an Improved Understanding of Coupled Morphological, Electrochemical, and Mechanical Behavior. **2** 664-672(2017)

117. Fuller, T. & Harb, J. *Electrochemical Engineering*. (John Wiley and Sons Inc., 2018).

118. Iermakova, D. I., Dugas, R., Palacín, M. R. & Ponrouch, A. On the Comparative Stability of Li and Na Metal Anode Interfaces in Conventional Alkyl Carbonate Electrolytes. *J. Electrochem. Soc.* **162**, A7060–A7066 (2015).

119. Fu, J. *et al.* Electrically Rechargeable Zinc–Air Batteries: Progress, Challenges, and Perspectives. *Adv. Mater.* **29**, 1604685 (2017).

120. Enviromental Protection Agency. 2017 National Emissions Inventory Report. (2020).

121. Hammer, M. S. *et al.* Global Estimates and Long-Term Trends of Fine Particulate Matter Concentrations (1998-2018). *Environ. Sci. Technol.* **54**, 7879–7890 (2020).

122. Apte, J. S., Marshall, J. D., Cohen, A. J. & Brauer, M. Addressing Global Mortality from Ambient $PM_{2.5}$. *Environ. Sci. Technol.* **49**, 8057–8066 (2015).

123. Pinguelli-Rosa, L. & Kahn-Ribeiro, S. The present, past, and future contributions to global warming of CO_2 emissions from fuels. *Clim. Change* **48**, 289–308 (2001).

124. Oberschelp, C., Pfister, S. & Hellweg, S. Globally Regionalized Monthly Life Cycle Impact Assessment of Particulate Matter. *Environ. Sci. Technol.* **54**, 16028–16038 (2020).

125. Laine, J. E. *et al.* Prenatal Exposure to Multiple Air Pollutants, Mediating Molecular Mechanisms, and Shifts in Birthweight. *Environ. Sci. Technol.* **54**, 14502–14513 (2020).

126. Shi, W. *et al.* Depression and Anxiety Associated with Exposure to Fine Particulate Matter Constituents: A Cross-Sectional Study in North China. *Environ. Sci. Technol.* **54**, 16006–16016 (2020).

127. Zhang, J. *et al.* Chronic Exposure to $PM_{2.5}$ Nitrate, Sulfate, and Ammonium Causes Respiratory System Impairments in Mice . *Environ. Sci. Technol.* **55**, 3081-3090 (2021)

128. Douglas W. Dockery, et al. An association between air pollution and mortality in 6 U.S. Cities. *The New England Journal of Medicine* vol. 329 1753–1759 (1993).

129. Oberdörster, G., Oberdörster, E. & Oberdörster, J. Nanotoxicology: An emerging discipline evolving from studies of ultrafine particles. *Environ. Health Perspect.* **113**,

823–839 (2005).

130. Pope III, C. A. *et al.* Lung Cancer, Cardiopulmonary Mortality, and Long-term Exposure to Fine Particulate Air Pollution. *J. Am. Med. Assoc.* **287**, 1132–1141 (2002).

131. Lelieveld, J., Evans, J. S., Fnais, M., Giannadaki, D. & Pozzer, A. The contribution of outdoor air pollution sources to premature mortality on a global scale. *Nature* **525**, 367–371 (2015).

132. Tuomisto, J. T., Wilson, A., Evans, J. S. & Tainio, M. Uncertainty in mortality response to airborne fine particulate matter: Combining European air pollution experts. *Reliab. Eng. Syst. Saf.* **93**, 732–744 (2008).

133. Shi, J., Xu, C., Xiang, L., Chen, J. & Cai, Z. Tris(2,4-di- tert-butylphenyl)phosphate: An Unexpected Abundant Toxic Pollutant Found in $PM_{2.5}$. *Environ. Sci. Technol.* **54**, 10570–10576 (2020).

134. Califirnia Air Resources Board. *California's Plan to Reduce Diesel Particulate Matter Emmissions*. (2010).

135. World Health Organization, W. WHO Air quality guidelines for particulate matter, ozone, nitrogen dioxide and sulfur dioxide: Global update 2005. 1–21 (2005)

136. U.S. EPA. Policy Assessment for the Review of the Particulate Matter National Ambient Air Quality Standards. *U.S. Environ. Prot. Agency, Off. Air Qual. Plan. Stand.* (2020).

137. Health Canada, E. C. National Ambient Air Quality Objectives for Particulate Matter: Executive Summary: Part 1: Science Assessment Document. *Air Qual.* (2004).

138. Union, E., Regulation, E. C., Iv, E., Iv, E. & Vi, T. E. Euro IV, Euro V and VI Emissions Regulations for Heavy Duty Vehicle Information Note. **2009**, 1–11 (2016).

139. Peng, W. *et al.* The Critical Role of Policy Enforcement in Achieving Health, Air Quality, and Climate Benefits from India's Clean Electricity Transition. *Environ. Sci. Technol.* **54**, 11720–11731 (2020).

140. Walter, R., Neumann, J. & Hinrichsen, O. Extended Model for Filtration in Gasoline Particulate Filters under Practical Driving Conditions. *Environ. Sci. Technol.* **54**, 9285–9294 (2020).

141. Yang, S. *et al.* Recycling diesel soot nanoparticles for use as activated carbon in Li ion batteries. *Resour. Conserv. Recycl.* **169**, (2021).

142. Elizabeth, I., Singh, B. P., Trikha, S. & Gopukumar, S. Bio-derived hierarchically macro-meso-micro porous carbon anode for lithium/sodium ion batteries. *J. Power Sources* **329**, 412–421 (2016).

143. Li, Y., Li, C., Qi, H., Yu, K. & Liang, C. Mesoporous activated carbon from corn stalk core for lithium ion batteries. *Chem. Phys.* **506**, 10–16 (2018).

144. Yu, K. *et al.* Preparation of porous carbon anode materials for lithium-ion battery from rice husk. *Mater. Lett.* **253**, 405–408 (2019).

145. Selvamani, V., Ravikumar, R., Suryanarayanan, V., Velayutham, D. & Gopukumar, S.

Garlic peel derived high capacity hierarchical N-doped porous carbon anode for sodium/lithium ion cell. *Electrochim. Acta* **190**, 337–345 (2016).

146. Zheng, P. *et al.* Sweet potato-derived carbon nanoparticles as anode for lithium ion battery. *RSC Adv.* **5**, 40737–40741 (2015).

147. Lim, D. G. *et al.* Lithium storage in structurally tunable carbon anode derived from sustainable source. *Carbon N. Y.* **121**, 134–142 (2017).

148. Jones, E. M. C., Çapraz, Ö. Ö., White, S. R. & Sottos, N. R. Reversible and Irreversible Deformation Mechanisms of Composite Graphite Electrodes in Lithium-Ion Batteries. *J. Electrochem. Soc.* **163**, A1965–A1974 (2016).

149. Missyul, A., Bolshakov, I. & Shpanchenko, R. XRD study of phase transformations in lithiated graphite anodes by Rietveld method. *Powder Diffr.* **32**, S56–S62 (2017).

150. Shi, H., Reimers, J. N. & Dahn, J. R. Structure-refinement program for disordered carbons. *J. Appl. Crystallogr.* **26**, 827–836 (1993).

151. Yang, J. *et al.* Enhanced Capacity and Rate Capability of Nitrogen/Oxygen Dual-Doped Hard Carbon in Capacitive Potassium-Ion Storage. *Adv. Mater.* **30**, 1700104 (2018).

152. Liu, L. *et al.* Understanding of the Ultrastable K-Ion Storage of Carbonaceous Anode. *Adv. Funct. Mater.* **28**, 1801989 (2018).

153. Elizabeth, I., Singh, B. P., Trikha, S. & Gopukumar, S. Bio-derived hierarchically macro-meso-micro porous carbon anode for lithium/sodium ion batteries. *J. Power Sources* **329**, 412–421 (2016).

154. Ferrari, A. C. & Basko, D. M. Raman spectroscopy as a versatile tool for studying the properties of graphene. *Nat. Nanotechnol.* **8**, 235–246 (2013).

155. Niu, F. *et al.* $MoSe_2$-Covered N,P-Doped Carbon Nanosheets as a Long-Life and High-Rate Anode Material for Sodium-Ion Batteries. *Adv. Funct. Mater.* **27**, 1700522 (2017).

156. Ma, G. *et al.* Phosphorus and oxygen dual-doped graphene as superior anode material for room-temperature potassium-ion batteries. *J. Mater. Chem. A* **5**, 7854–7861 (2017).

157. Elgrishi, N. *et al.* A Practical Beginner's Guide to Cyclic Voltammetry. *J. Chem. Educ.* **95**, 197–206 (2018).

158. Tabassum, H. *et al.* A Universal Strategy for Hollow Metal Oxide Nanoparticles Encapsulated into B/N Co-Doped Graphitic Nanotubes as High-Performance Lithium-Ion Battery Anodes. *Adv. Mater.* **30**, 1705441 (2018).

159. Penki, T. R., Shanmughasundaram, D., Kishore, B. & Munichandraiah, N. High rate capability of coconut kernel derived carbon as an anode material for lithium-ion batteries. *Adv. Mater. Lett.* **5**, 184–190 (2014).

160. Aurbach, D. *et al.* Common Electroanalytical Behavior of Li Intercalation Processes into Graphite and Transition Metal Oxides. *J. Electrochem. Soc.* **145**, 3024–3034 (1998).

161. Jiang, Y. & Liu, J. Definitions of Pseudocapacitive Materials: A Brief Review. *Energy Environ. Mater.* **2**, 30–37 (2019).

162. Cohn, A. P. *et al.* Durable potassium ion battery electrodes from high-rate cointercalation into graphitic carbons. *J. Mater. Chem. A* **4**, 14954–14959 (2016).

163. Brezesinski, T., Wang, J., Tolbert, S. H. & Dunn, B. Ordered mesoporous α-MoO_3 with iso-oriented nanocrystalline walls for thin-film pseudocapacitors. *Nat. Mater.* **9**, 146–151 (2010).

164. Yang, C. *et al.* Metallic Graphene-Like VSe_2 Ultrathin Nanosheets: Superior Potassium-Ion Storage and Their Working Mechanism. *Adv. Mater.* **30**, 1–8 (2018).

165. Chao, D. *et al.* Pseudocapacitive Na-Ion Storage Boosts High Rate and Areal Capacity of Self-Branched 2D Layered Metal Chalcogenide Nanoarrays. *ACS Nano* **10**, 10211–10219 (2016).

166. Wang, J., Polleux, J., Lim, J. & Dunn, B. Pseudocapacitive contributions to electrochemical energy storage in TiO_2 (anatase) nanoparticles. *J. Phys. Chem. C* **111**, 14925–14931 (2007).

167. Miller, J. R. & Burke, A. F. Electrochemical capacitors: Challenges and opportunities for real-world applications. *Electrochem. Soc. Interface* **17**, 53–57 (2008).

168. Kubota, K., Dahbi, M., Hosaka, T., Kumakura, S. & Komaba, S. Towards K-Ion and Na-Ion Batteries as "Beyond Li-Ion". *Chem. Rec.* **18**, 459–479 (2018).

169. Slater, M. D., Kim, D., Lee, E. & Johnson, C. S. Sodium-ion batteries. *Adv. Funct. Mater.* **23**, 947–958 (2013).

.

APPENDICES

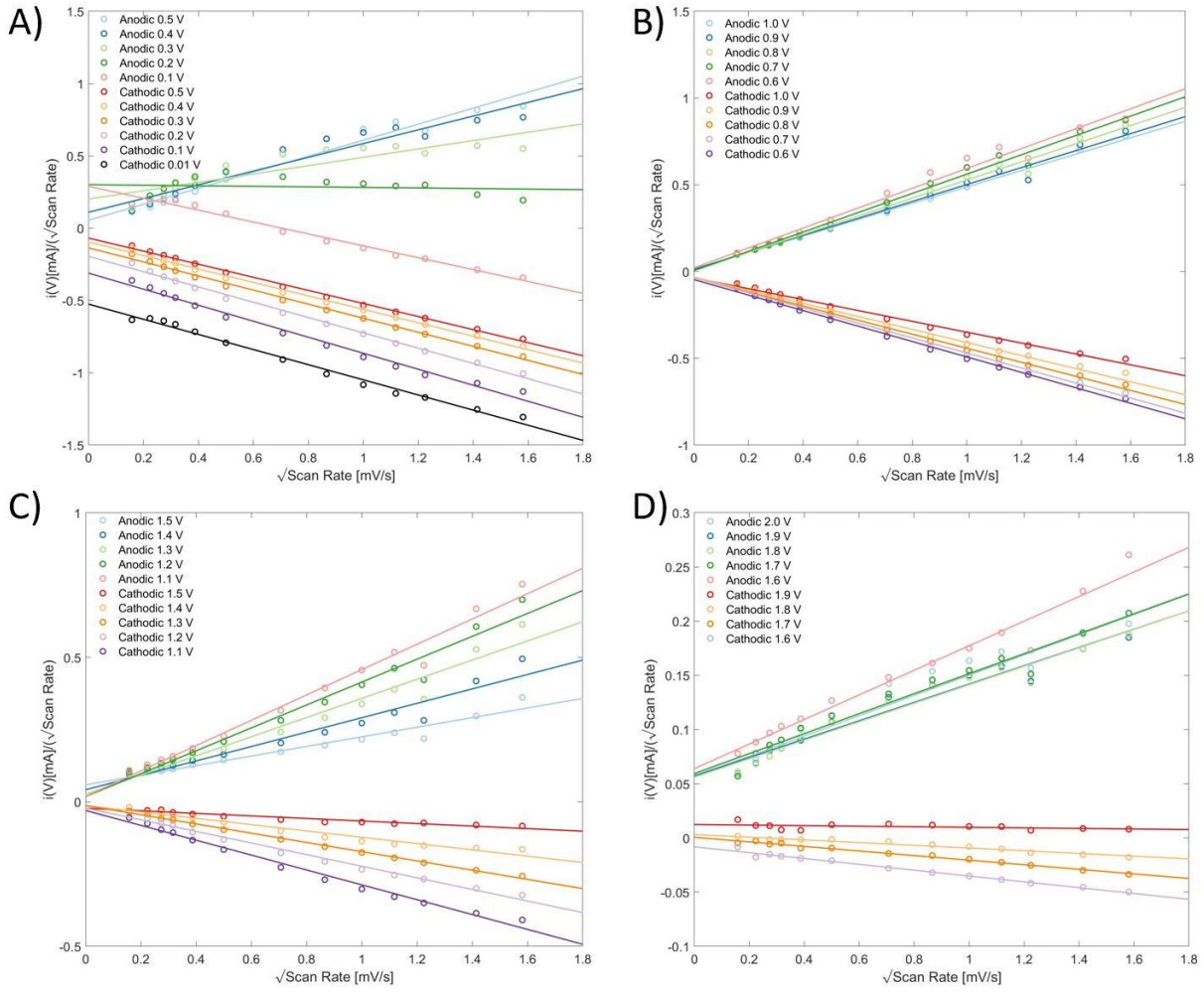

Figure A1: Relationships between $i(V)/v^{0.5}$ vs $v^{0.5}$ for calculating constants k_1 and k_2 at potentials between A) 0.01 – 0.5 V, B) 0.6 – 1.0 V, C)1.1 – 1.5 V, D) 1.6 – 2.0

Table A1: K-Values extracted from Figure A1

K-Values							
Cathodic				Anodic			
Potential [V]	k1	k2	R^2	Potential [V]	k1	k2	R^2
0.01	-0.5239	-0.5254	0.9894	0.01			
0.1	-0.5541	-0.3112	0.9887	0.1	-0.4115	0.2891	0.9835
0.2	-0.5291	-0.1951	0.9949	0.2	-0.019	0.3007	0.019
0.3	-0.4867	-0.1363	0.9957	0.3	0.2893	0.2008	0.7782
0.4	-0.4652	-0.0965	0.9963	0.4	0.4752	0.1097	0.9246
0.5	-0.4524	-0.0687	0.9969	0.5	0.5537	0.0545	0.9592
0.6	-0.4456	-0.0465	0.997	0.6	0.5731	0.0209	0.9807
0.7	-0.4333	-0.0359	0.9973	0.7	0.5568	0.0048	0.9883
0.8	-0.4053	-0.0367	0.9959	0.8	0.5223	0.0055	0.9879
0.9	-0.3767	-0.0322	0.9959	0.9	0.4888	0.0127	0.9867
1	-0.3135	-0.0361	0.9922	1	0.4718	0.016	0.9893
1.1	-0.2572	-0.0299	0.9882	1.1	0.4382	0.0193	0.981
1.2	-0.2007	-0.022	0.9895	1.2	0.3961	0.0182	0.9738
1.3	-0.1598	-0.0126	0.9968	1.3	0.3315	0.0264	0.9588
1.4	-0.1092	-0.0133	0.96	1.4	0.2492	0.0419	0.9469
1.5	-0.044	-0.0223	0.9171	1.5	0.1662	0.0588	0.954
1.6	-0.0269	-0.0082	0.9837	1.6	0.1134	0.0639	0.9646
1.7	-0.0211	0.0006	0.9878	1.7	0.0921	0.0594	0.961
1.8	-0.0125	0.0032	0.9424	1.8	0.0852	0.0561	0.9608
1.9	-0.0026	0.0124	0.1978	1.9	0.0845	0.0574	0.9567
2				2	0.0934	0.0567	0.9473

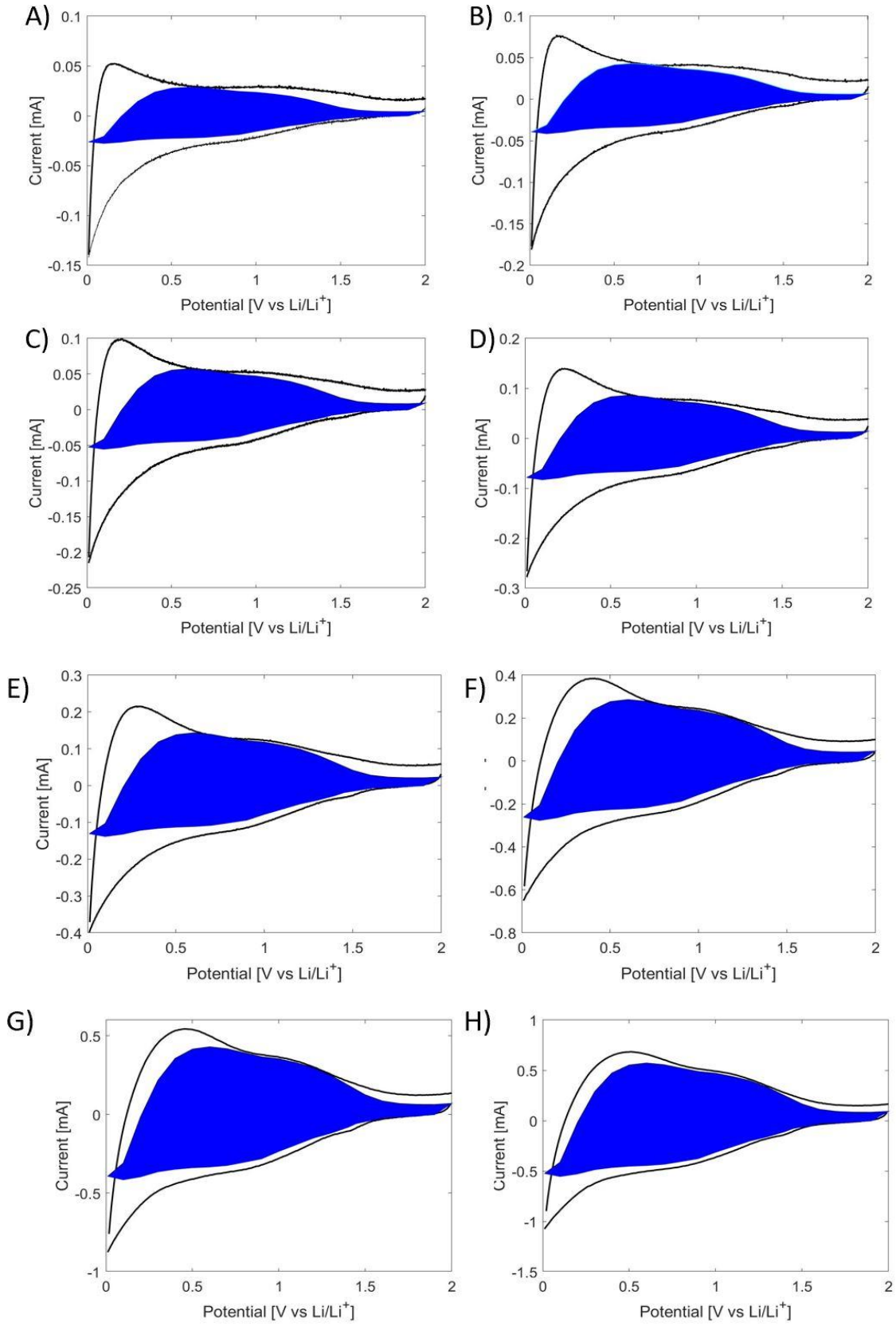
A)
B)
C)
D)
E)
F)
G)
H)
Current [mA]
Potential [V vs Li/Li+]

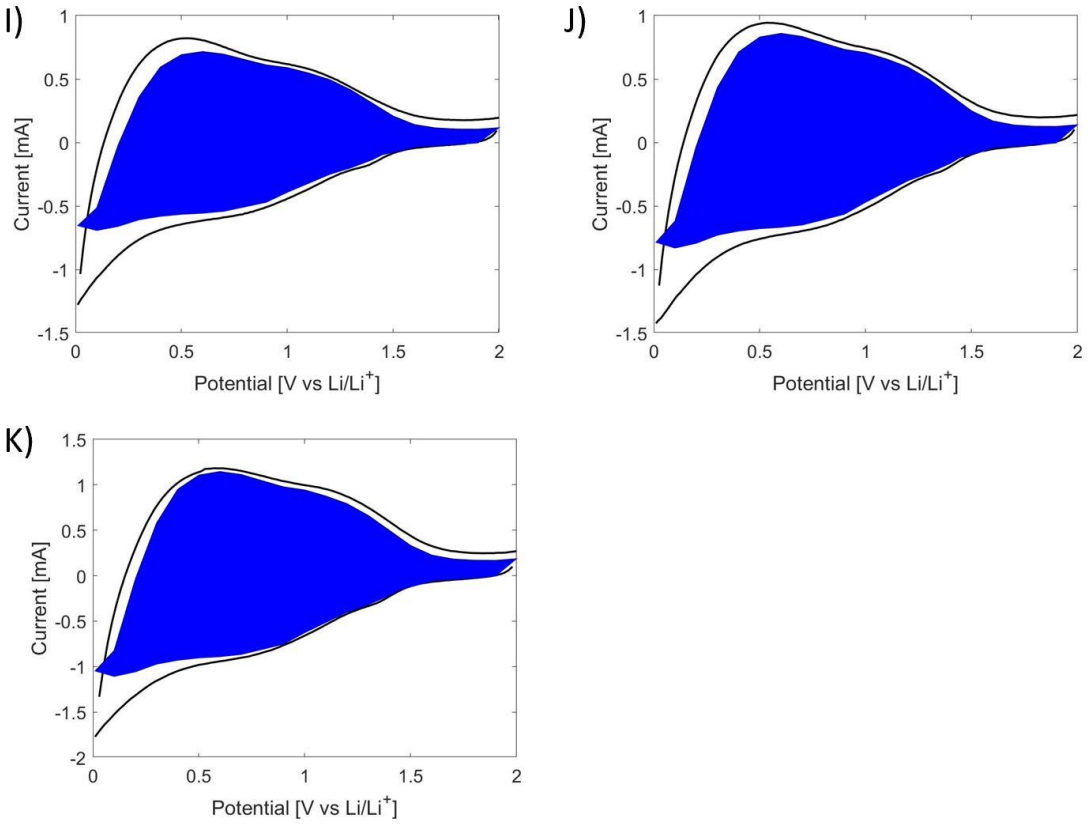

Figure A2: Capacitive charge storage contributions at A) 50, B) 75, C) 100, D) 150, E) 250, F) 500, G) 750, H) 1000, I)1250, J) 1500, K) 2000 $\mu V\ s^{-1}$

VITA

DARRELL REID GREGORY

Candidate for the Degree of

Master of Science

Thesis: ELECTROCHEMICAL BEHAVIOR AND MORPHOLOGICAL EVOLUTION IN CARBONACEOUS AND METAL ANODES FOR Li-ION AND Zn-ION BATTERIES

Major Field: Chemical Engineering

Biographical:

Education:

Completed the requirements for the Master of Science in Chemical Engineering at Oklahoma State University, Stillwater, Oklahoma in May 2021.

Completed the requirements for the Bachelor of Science Chemical Engineering at Oklahoma State University, Stillwater, Oklahoma in 2019.

Experience:

- Graduate Teaching Assistant, Oklahoma State University, United States, 2019-Present.
- Undergraduate Student Lab Mentor, Oklahoma State University, United States, 2019-Present.

Professional Memberships:

- American Institute of Chemical Engineers (AIChE)
- The Electrochemical Society (ECS)